



저작자표시-비영리-변경금지 2.0 대한민국

이용자는 아래의 조건을 따르는 경우에 한하여 자유롭게

- 이 저작물을 복제, 배포, 전송, 전시, 공연 및 방송할 수 있습니다.

다음과 같은 조건을 따라야 합니다:



저작자표시. 귀하는 원저작자를 표시하여야 합니다.



비영리. 귀하는 이 저작물을 영리 목적으로 이용할 수 없습니다.



변경금지. 귀하는 이 저작물을 개작, 변형 또는 가공할 수 없습니다.

- 귀하는, 이 저작물의 재이용이나 배포의 경우, 이 저작물에 적용된 이용허락조건을 명확하게 나타내어야 합니다.
- 저작권자로부터 별도의 허가를 받으면 이러한 조건들은 적용되지 않습니다.

저작권법에 따른 이용자의 권리는 위의 내용에 의하여 영향을 받지 않습니다.

이것은 [이용허락규약\(Legal Code\)](#)을 이해하기 쉽게 요약한 것입니다.

[Disclaimer](#)

공학박사 학위논문

**LOW NOISE GENERATION OF
OPTICAL AND PLASMONIC FIELDS
BASED ON REGULARIZATION OF
RADIATION PATTERNS OF
HUYGENS' SOURCES**

호이겐스 광원의 방사 패턴 정규화에 기반한
광파 및 플라즈몬파 저잡음 형성

2018년 8월

서울대학교 대학원

전기·컴퓨터공학부

박 현 수

LOW NOISE GENERATION OF OPTICAL AND PLASMONIC FIELDS BASED ON REGULARIZATION OF RADIATION PATTERNS OF HUYGENS' SOURCES

지도 교수 이 병 호

이 논문을 공학박사 학위논문으로 제출함
2018년 8월

서울대학교 대학원
전기·컴퓨터공학부
박 현 수

박현수의 공학박사 학위논문을 인준함
2018년 8월

위 원 장 _____ (인)
부위원장 _____ (인)
위 원 _____ (인)
위 원 _____ (인)
위 원 _____ (인)

Abstract

Low noise generation of optical and plasmonic fields based on regularization of radiation patterns of Huygens' sources

Hyeonsoo Park

Department of Electrical Engineering and Computer Science

College of Engineering

Seoul National University

Huygens' principle has been the central part of optical diffraction theory since Huygens wrote on the explanation of refraction and reflection of light in 1690. Especially, the notion of secondary wave is still useful to explain optical diffraction and scattering phenomena. Recently, research on metamaterials have been one of the most active fields in applied physics for the past two decades. Meta-atoms constitute metamaterials in 3D, metasurfaces in 2D, and meta-slits in 1D. Meta-atoms are engineered artificial structures of subwavelength-size, in other words, meta-atoms are Huygens' sources by definition. By engineering shape and arrangement of meta-atoms, researchers have invented various types of metamaterials having exotic optical properties. However, consideration on radiation patterns of meta-atoms has not been seriously addressed by researchers. In this dissertation, I address the importance of engineering radiation patterns of meta-atoms for low noise generation of optical and plasmonic fields by proposing and examining novel types of metasurfaces and meta-slits.

Firstly, I give a brief historical overview of optical diffraction theories based on Huygens' principle, then define what is Huygens' sources and see how meta-atoms can be served as engineered Huygens' sources of designated radiation patterns. I show that meta-atom array of equalized radiation patterns can generate a plane wave without distortion, then give mathematical formulation to illustrate that array of idealized Huygens' sources can serve as the platform of generating arbitrary field with extremely low noise.

Secondly, complex amplitude modulation capability of meta-atoms

compatible with the regularization process is examined. This study is crucial to develop metasurfaces and meta-slits with regularized Huygens' sources because arbitrary optical and plasmonic wavefront is described by complex amplitude distribution.

The subsequent two chapters of this dissertation are devoted to demonstrating generation of optical and plasmonic fields by refining the proposed method in Chapter 2. The proposed metasurfaces and meta-slits are constructed by periodically arranging meta-atoms of regularized radiation patterns, I show that they are capable of generating arbitrary optical and plasmonic fields if complex amplitude and polarization of meta-atoms are realizable.

In Chapter 4, metal-clad waveguide array is proposed as a concrete example of regularized meta-slits. Plasmonic focal spot and plasmonic Airy beam are generated by the proposed structure. Numerical results including full-field simulation are delivered to analyze the generated wavefronts in the sense of signal-to-noise ratio. Experimental suggestion is also made.

In the consequent chapter, for optical field synthesis, generalization of the field synthesis method carried out in Chapters 2 and 4 is proposed. Assuming optical meta-atoms can assign designated complex amplitude electric dipole moment with arbitrary in-plane polarization, then electric dipole metasurfaces equipped with these hypothetical meta-atoms are proposed, and the generalized method of optical field synthesis enables to generate any optical wavefront via the proposed metasurfaces with extremely low noise. I also give a method to realize approximated versions of the proposed metasurfaces by proposing 'quasi-regularization'. Various types of metasurfaces including quasi-regularized metasurfaces are examined by comparative study of generating Airy disk, Bessel-Gauss beam, and hologram in the sense of signal-to-noise ratio. Experimental results on hologram generation of the presented metasurfaces are also provided.

I expect that this dissertation can help to develop advanced meta-devices that account radiation patterns of meta-atoms for achieving full control of generating and manipulating light and surface plasmons. Furthermore, by applying regularization process, wide-angle operation of spatial light modulators with extremely low noise level is viable, and it requires future research on compact active modulation mechanism.

Keywords: Huygens' principle, radiation pattern, complex modulation, optical field, plasmonic field, metasurface, meta-slit

Student Number: 2012-20775

Contents

| | |
|---|------------|
| Abstract | i |
| Contents | iii |
| List of Tables | v |
| List of Figures | vi |
| Chapter 1 Introduction | 1 |
| 1.1 Overview | 1 |
| 1.2 Motivation and organization of this dissertation | 7 |
| Chapter 2 Radiation patterns of Huygens' sources and its regularization process | 12 |
| 2.1 Electromagnetic Huygens' sources | 12 |
| 2.1.1 Key results in Huygens' principle based optical diffraction theories | 12 |
| 2.1.2 Definition and characterization of Huygens' sources | 18 |
| 2.2 Huygens' sources in meta-systems | 20 |
| 2.2.1 Huygens' sources in meta-slits..... | 20 |
| 2.2.2 Huygens' sources in metasurfaces | 23 |
| 2.3 Regularized radiation patterns of Huygens' sources | 25 |
| 2.4 Arbitrary field generation via ideal Huygens' sources | 27 |
| 2.5 Conclusion..... | 30 |
| Chapter 3 Design of regularized Huygens' source | 31 |
| 3.1 Introduction | 31 |
| 3.1.1 Scattering process of parallel metal strips in 2D MIM plasmonic waveguide | 31 |
| 3.1.2 Near-infrared magnetic dipole resonant coherent perfect absorption in 2D MIM plasmonic waveguide..... | 36 |
| 3.1.3 Frequency dependence of magnetic and electric dipole resonance | 43 |
| 3.1.4 Analysis of CPA characteristics in 2D MIM plasmonic waveguide | 47 |
| 3.2 Design of complex amplitude reflection coefficient of light in MIM plasmonic waveguide | 50 |
| 3.2.1 2D waveguide with magnetic dipole resonator and metallic end...50 | |
| 3.2.2 3D waveguide with electric dipole resonator and metallic end.....57 | |
| 3.2.3 3D waveguide with asymmetric slit apertures | 62 |
| 3.3 Design of complex amplitude transmission coefficient of light in 3D metal-clad waveguide..... | 66 |
| 3.4 Conclusion..... | 72 |
| Chapter 4 Low-noise generation of plasmonic field based on regularized Huygens' sources | 74 |
| 4.1 Introduction | 74 |

| | |
|---|------------|
| 4.2 Tilted slit coupled to metal-clad waveguide as regularized Huygens' plasmonic source | 75 |
| 4.3 Rigorous generation of plasmonic field via metal-clad waveguide array . | 81 |
| 4.3.1 Plasmonic focal spot..... | 81 |
| 4.3.2 Plasmonic Airy beam | 83 |
| 4.4 Experimental suggestion and demonstration..... | 86 |
| 4.4.1 Experimental suggestion of fabricating a variant of metal-clad waveguide array | 86 |
| 4.4.2 Comparative study on meta-slits | 88 |
| 4.5 Conclusion..... | 90 |
| Chapter 5 Low-noise generation of optical field based on regularized Huygens' sources..... | 91 |
| 5.1 Introduction | 91 |
| 5.2 Electric dipole metasurfaces as regularized Huygens' optical sources | 92 |
| 5.3 Rigorous generation of optical field via electric dipole metasurface | 94 |
| 5.3.1 Linearly polarized Airy disk | 94 |
| 5.3.2 Bessel-Gauss beam..... | 103 |
| 5.3.3 Hologram..... | 106 |
| 5.4 Analysis of field generation via EDMs | 108 |
| 5.4.1 Signal-to-noise ratio analysis | 108 |
| 5.4.2 Derivation of wave-optical EDMs | 109 |
| 5.5 Realization of electric dipole metasurfaces..... | 112 |
| 5.5.1 Quasi-regularization of radiation patterns for metasurfaces | 112 |
| 5.5.2 Generation of circularly polarized Airy disk..... | 115 |
| 5.5.3 Hologram..... | 117 |
| 5.6 Experimental demonstration..... | 120 |
| 5.6.1 Fabrication and experimental setup..... | 120 |
| 5.6.2 Hologram generation..... | 123 |
| 5.7 Conclusion..... | 126 |
| Chapter 6 Conclusion | 128 |
| Bibliography..... | 132 |
| Appendix | 150 |
| 초 록 | 151 |

List of Tables

| | |
|---|----|
| Table 3.1 Gap between elements make radiation pattern irregular, and plasmonic waveguide regularizes radiation pattern..... | 67 |
|---|----|

List of Figures

| | |
|--|----|
| Figure 1.1 Scope of this dissertation | 9 |
| Figure 2.1 Illustration of the Huygens-Fresnel equation in Eq. 2.1. | 13 |
| Figure 2.2 Parameters in the Kirchhoff-Helmholtz integral theorem (Eq. 1.3) for monochromatic scalar wave are illustrated. | 14 |
| Figure 2.3 Illustration of the Fresnel-Kirchhoff diffraction integral | 15 |
| Figure 2.4 Illustration of surface equivalence principle..... | 17 |
| Figure 2.5 Illustration of simple nano-structures as meta-atoms in meta-slits: (a) bump, (b) dip, and (c) slit. | 21 |
| Figure 2.6 Top view of nano-apertures illuminated by polarized optical wave. (a) shape of nano-aperture affects induced charge distribution and consequently radiation pattern of excited SPPs, (b) polarization of incident light is also a key factor to alter radiation pattern, (c) nano-slit of moderate size radiates SPPs with magnetic dipole-like radiation pattern if it is illuminated by normally incident wave with polarization parallel to the minor axis of the nano-slit..... | 22 |
| Figure 2.7 Examples of Huygens' sources in metasurfaces (a) nano-rod for electric dipole Huygens' sources and nano-slit for magnetic dipole Huygens' sources, (b) more complex nano-structure such as split ring resonator (SRR) has magnetic dipole-like radiation pattern around the resonance frequency. (c) Scattering process of nano-slit. | 24 |
| Figure 2.8 (a) Illustration of sampling process of a target wavefront (green) by | |

| | | |
|------------|--|----|
| | meta-atoms, and (b) Reconstructed field (red) via ideal Huygens' source array is proportional to the target field..... | 27 |
| Figure 3.1 | The proposed CPA embedded in an MIM plasmonic waveguide is depicted. Parallel metal strips absorb light via magnetic dipole resonance. Two metal strips should be close enough to hybridize their plasmonic resonances..... | 33 |
| Figure 3.2 | When the parallel metal strips embedded in the plasmonic waveguide are close enough, two resonant modes are hybridized into electric dipole resonance and magnetic dipole resonance, respectively. The two resonances are separated in the frequency domain (ω -axis). Polarization current (red arrows) and charge distribution (plus, minus sign) are indicated for each case..... | 34 |
| Figure 3.3 | Illustration of the structural parameters and scattering process of the CPA structure illuminated by symmetrically incident mode..... | 39 |
| Figure 3.4 | Absorption ratio of an optimized CPA structure against wavelength with different relative phase Δ . Values of the parameters are $d = 15$ nm, $w = 150$ nm, $g = 16.5$ nm, and $l = 200$ nm..... | 40 |
| Figure 3.5 | Magnetic field distribution of CPA structure for (a) symmetrically incident waves, $\Delta = 0$, and (b) anti-symmetrically incident waves, $\Delta = \pi$. The structural parameters are same as Fig. 3.4..... | 42 |
| Figure 3.6 | Manipulating the values of geometric parameters changes the scattering matrix S and frequency dependence of the complex-valued parameter m . (a) schematic of the trajectory of the parameter m , (b) numerical results derived from five different structures. The other parameters are fixed at $d = 10$ nm, $w = 160$ nm, and $l = 200$ nm..... | 43 |
| Figure 3.7 | Illustration of a single strip embedded in a MIM waveguide with anti-symmetrically incident light..... | 45 |

| | |
|--|----|
| Figure 3.8 Numerical analysis on a single strip embedded in a MIM waveguide with anti-symmetrically incident light as in Fig. 3.7. (a) the absorption spectra of a single strip and (b) the corresponding trajectory of the complex-valued parameter p . The other parameters are fixed at $w = 150$ nm and $l = 200$ nm..... | 46 |
| Figure 3.9 Absorption spectra of symmetrically incident waves in the proposed structure with varying (a) w , (b) d and (c) g . l is fixed at 200 nm. The other parameters are fixed at (a) $d = 10$ nm, $g = 15$ nm, (b) $g = 15$ nm, $w = 160$ nm, and (c) $w = 160$ nm, $d = 10$ nm. (d) Absorption spectra for various CPA structures with operating wavelength between 1 μ m (green line) and 1.6 μ m (black line) | 49 |
| Figure 3.10 Illustration of continuous control of complex amplitude modulation of r by two dimensional parameters p_1 and p_2 | 51 |
| Figure 3.11 Illustration of (a) scattering process and (b) structural parameters of the proposed structure with complex amplitude reflection coefficient. | 52 |
| Figure 3.12 Trajectories of the overall reflection coefficient. If the absorbing structure is critically coupled (red line), full complex modulation (red filled circle) of light is realized. | 53 |
| Figure 3.13 Absorption ratio characteristics of the optimized structure with respect to the parameter, L_2 | 55 |
| Figure 3.14 Trajectories of the overall reflection coefficient along L_2 , with different values of L_1 . The structural parameters are optimized to achieve critically coupled condition: $g = 18$ nm, $w = 152$ nm, $d = 15$ nm, and $l = 200$ nm..... | 56 |
| Figure 3.15 Schematic of the proposed cavity structure composed of nanostrip in a three-dimensional metal-clad plasmonic waveguide..... | 58 |

Figure 3.16 Four modes are the lowest order modes in the square aperture waveguide. (a) and (b) are propagation modes, and the others are evanescent modes.....59

Figure 3.17 (a) Reflection characteristics of the optimized structure with respect to the parameter, L_259

Figure 3.18 Complex modulation map of the reflection coefficient if the optimized nanostrip is inside the square aperture waveguide.60

Figure 3.19 Illustration of reflection and transmission coefficient at the edge of the waveguide (slice view). (a) in-coupling, and (b) out-coupling.61

Figure 3.20 Illustration of cavity formed by square aperture waveguide with two asymmetric slit apertures at its end. Structural parameters are also found. The target wavelength is 532 nm (green).....63

Figure 3.21 Complex amplitude map of reflection coefficient of the cavity with respect to l_1 and l_264

Figure 3.22 Schematics of (a), (c) a supercell metasurface of which unit cell comprised of four H-shaped apertures, and (b), (d) regularized version of the supercell metasurface depicted in (a). Two orthogonal plasmonic modes in a short metal-clad plasmonic waveguide of unit cell have equal coupling efficiency of four apertures.....69

Figure 3.23 Cross-polarization transmission coefficient with respect to various set of rotation angles θ_1 and θ_2 . For convenience, two parameters θ_+ and θ_- are defined as $\theta_+ = \theta_1 + \theta_2$, $\theta_- = \theta_1 - \theta_2$. Periodic condition is used with normal incidence of circular polarized light.70

Figure 4.1 (a) and (c): Schematics of a conventional double-lined slit array (b) and (d): Schematics of the proposed structure, regularizing each unit cell of the shifted slit array. Both cases assume the incident light left-circularly polarized plane wave along +z-axis. Dimensions of the

metal-clad waveguide is given as $c_x = 100 \text{ nm}$, $c_z = 390 \text{ nm}$, $w = 100 \text{ nm}$, $L_{\text{prop}} = 2 \text{ }\mu\text{m}$, and $t_{\text{top}} = t_{\text{bottom}} = 80 \text{ nm}$. Size of slits are $s_x = 300 \text{ nm}$ and $s_y = 80 \text{ nm}$ 75

Figure 4.2 (a) and (c): Radiation field distributions of a unit cell of double-lined slit array for $\theta_1 = -30^\circ$, $\theta_2 = 60^\circ$. (b) and (d): Radiation field distributions in the proposed structure for $\theta = 0^\circ$, $d = 0 \text{ nm}$. The purple dashed lines indicate $y = 0 \text{ }\mu\text{m}$. (e) The waveguide mode efficiently produces a plasmonic field.....79

Figure 4.3 Numerical results of SPP focusing at $y = 7 \text{ }\mu\text{m}$ with (a) the proposed structure, and (b) the double-lined slit array. (c) Analytical dipole modelling produces a plasmonic field with sinc function profile. (d) The amplitudes of the simulated fields at the focal line are compared. Each blue dashed line on (a), (b) and (c) depicts the corresponding focal line.....82

Figure 4.4 Plasmonic Airy beams constructed by (a) the proposed structure and (b) the double-lined slit array. (c) Analytical dipole modelling produces a plasmonic Airy beam. (d) The amplitudes of the simulated fields at $y = 7 \text{ }\mu\text{m}$ are compared. Each blue dashed line on (a), (b) and (c) depicts $y = 7 \text{ }\mu\text{m}$ line.84

Figure 4.5 Illustration of the proposed fabrication process for a variant of the metal-clad waveguide array introduced in Sec. 4.2.....87

Figure 4.6 Demonstration of the performance of the two meta-slits: single-lined slit arrays and double-lined slit arrays. FIB images (first row), AFM images (second row), and NSOM images (third row) are provided. Single-lined slit arrays for generating plasmonic focal spot of $z_0 = 5 \text{ }\mu\text{m}$ (first column) and plasmonic Airy beam (second column).

| | |
|---|-----|
| Double-lined slit arrays for generating plasmonic focal spot of $z_0 = 5 \text{ um}$ (third column) and plasmonic Airy beam (fourth column). | 88 |
| Figure 5.1 A schematic of an electric dipole metasurface (EDM) with subwavelength-sized dielectric rods on a flat substrate. | 92 |
| Figure 5.2 Illustration of the derivation of the electric dipole moment density of the EDM generating an x -polarized Airy disk pattern. The dipole moment densities, p_ρ and p_ϕ , in the infinitesimal area dS_r , correspond to the angular spectral components of the x -polarized Airy disk \mathcal{E}_ρ and \mathcal{E}_ϕ on the output plane, respectively. | 95 |
| Figure 5.3 Comparison between EDM distributions generating the amplitude of normalized Airy disk with $\text{NA} = \sin(75^\circ) = 0.966$, $z_0 = 5 \text{ um}$, $k_0 = 2\pi / (1 \text{ um})$, and the reconstructed field distributions of an EDM for an x -polarized Airy disk (left column) and an EDM with a nullified p_y (right column)..... | 100 |
| Figure 5.4 Schematics for the (a) sampling and (b) reconstruction scheme for a Bessel-Gauss beam with topological charge $m = 2$ | 103 |
| Figure 5.5 Generation of the Bessel-Gauss beam of the topological charge 2 via the EDM by sampling the transverse electric field on the focal plane $z = z_0 = 20 \text{ um}$. The amplitude distributions of p_{RCP} and p_{LCP} of the corresponding EDM (upper row) that generate the Bessel-Gauss beam. Plots of the amplitude distributions of E_{RCP} , E_{LCP} , E_z , and \vec{E} of the generated wavefront and the distribution of the polarization of the transverse electric field on the focal plane, and amplitude distributions of the transverse electric field at $z = 5, 10, 15, 20, 25, 30$ | |

| | | |
|-------------|--|-----|
| | and 35 μm (lower row)..... | 105 |
| Figure 5.6 | (a) Schematic for hologram generation. EDM on the plane $z=0$ illuminated by normally incident LCP plane wave along the $+z$ -axis is derived by the superposition of sampled Airy disk units on the image plane $z=z_0=5 \mu\text{m}$. (b) Plots of the target image, the electric dipole distribution of the EDM, and the corresponding field distributions on the image plane. The wavelength $\lambda=1 \mu\text{m}$. The PSNR is 76.81. ... | 107 |
| Figure 5.7 | z_0 –SNR semi-log plot (center) for various NAs and focal lengths for EDMs. Four intensity profiles (the four corners of the figure) of the residual fields, which represent the difference between E_x generated by the EDM and the Airy disk on the focal plane. | 109 |
| Figure 5.8 | Comparison between WOEDM and ROEDM generating x -polarized Airy disks with $\text{NA} = \sin(45^\circ)=0.707$, $z_0=5 \mu\text{m}$, and $k_0 = 2\pi / (1 \mu\text{m})$. In-plane electric dipole distribution (upper row) and the generated field at the focal plane (lower row)..... | 111 |
| Figure 5.9 | Schematics of (a) unit cell of GPM, (b) unit cell (supercell) of DGPM, (c) unit cell (supercell) of QGPM (d) unit cell of XAM, respectively. | 113 |
| Figure 5.10 | Amplitude distribution of the E_{RCP} for the unit RCP Airy disks via the DGPM, QGPM, and XAM on the focal plane $z=z_0=5 \mu\text{m}$ and on the $y=0 \mu\text{m}$ plane (left panel). The three metasurfaces have the $\text{NA} = \sin 75^\circ=0.966$ and the wavelength $\lambda=1 \mu\text{m}$ | 116 |
| Figure 5.11 | The holograms of the same target image in Fig. 5.6(b) are generated via the conventional metasurfaces DGPM, QGPM and XAM, respectively, at the focal plane $z_0=5 \mu\text{m}$. The corresponding structural parameters | |

| | |
|---|-----|
| θ , θ_1 , and θ_2 are also presented (upper row)..... | 118 |
| Figure 5.12 (a) Schematic of fabrication process of forming nano-antennas on a quartz plate. (b) SEM images for fabricated samples of GPM, DGPM, QGPM, and XAM, respectively. | 121 |
| Figure 5.13 Schematic of experimental setup for measurement of hologram of geometric phase based metasurfaces..... | 122 |
| Figure 5.14 (a) Target image of the holograms, (b) optical microscope image of a patterned area of a QGPM sample. | 124 |
| Figure 5.15 Schematic of unit cell of GPM, DGPM, QGPM, and XAM, respectively (top panel). The corresponding CCD images of hologram (middle panel), and the numerically derived results of the same target image in Fig. 5.14(a) (bottom panel)..... | 124 |

Chapter 1 Introduction

1.1 Overview

Optical science through wave theoretic viewpoint started from *Traité de la Lumière* written by Christian Huygens in 1690 [1]. He introduced the concept of secondary waves to explain reflection and refraction phenomena of light at interfaces of different media. What is called Huygens' principle assumes that wavefront at any instant is regarded as the source of secondary waves and the envelop of the secondary waves forms the wavefront at a later instant. In the beginning of 18th century, Young and Fresnel introduced interference principle and the first diffraction theory of light respectively, and their works gave an account of distributions of light diffracted by opaque screens [2-10]. Fresnel's diffraction theory of light was so successful that most advocators of the corpuscular theory of light became wave theorists after the Fresnel's demonstration. It should be mentioned that Fresnel synthesized Young's interference principle and Huygens' principle into the Huygens-Fresnel diffraction theory. Secondary waves that are unblocked by an opaque screen interfere with each other and collectively construct diffracted waves.

Even in quantum electrodynamics, Huygens' principle is extensively used in

the formulation of propagator and path integral [11]. Propagator of the photon's wavefunction is described by the Green's function of Maxwell's equations, and the propagator explains the infinitesimal radiation process of the secondary wave from each point along the path of interest. Path integral deals with all possible paths that can be taken by a photon, and this calculation describes how secondary waves along different paths interfere with each other. The path integral gets the same envelop as the case of Huygens' original work if wavelength is small enough.

There have been continuous debates on how to extract secondary waves from incident wavefront toward diffracting objects and what are the radiation patterns of secondary waves [12-17]. Kirchhoff (1883) and Sommerfeld (1896) are early contributors for developing rigorous diffraction integrals of diffracted fields based on scalar wave theory [15-17].

To be consistent with Maxwell's equations, vector versions of optical diffraction theory have been proposed and investigated [10, 18-37]. With the help of surface equivalence principle [30-37], the source of the secondary waves is expressed in the form of surface current density or equivalently surface dipole densities. Continuous distribution of electric and magnetic dipole density is the natural choice of radiating source. Consequently, radiation patterns of infinitesimal secondary waves follow those of electric dipoles and magnetic dipoles.

As introduced above, Huygens' principle is adopted as the central part of their theory in Fresnel's diffraction theory and its successors. The concept of secondary waves introduced by Huygens' principle makes the calculation of diffraction field a

two-step process in many practical cases: Incident wavefront unblocked by diffracting object is the source of secondary waves. Integration of the radiated secondary waves gives the diffracted field. The abovementioned diffraction theories based on Huygens' principle are still relevant in analyzing and engineering diffractive optical systems [38-44].

Meanwhile, research on metamaterials is one of the most active fields in both optical science and engineering in the past two decades [45-52, 54-69]. The term 'metamaterial' is coined by Smith and his collaborators in 2000 [53]. The prefix 'meta' is used to mean 'beyond', and 'metamaterials' intend to represent systems that attain material properties beyond those of conventional materials by embracing artificially engineered inclusions, called meta-atoms.

If size of meta-atoms is much smaller than wavelength, then effective medium theory is feasible. That is, optical response of individual inclusions is homogenized, and collective response of inclusions is described by effective material properties: electric permittivity and magnetic permeability. For example, meta-atoms such as split-ring resonators (SRRs) have magnetic dipole resonance, metamaterials comprised of SRRs have non-trivial effective magnetic permeability around the resonance frequency of the SRRs [54, 55]. By engineering meta-atoms, any distribution of effective material parameters of metamaterials can be designed in principle. Effective material properties of metamaterials critically depend on shape and arrangement of meta-atoms as well as the properties of constituent materials.

Researches on metamaterials revealed lots of exotic physics and applications

that are unattainable by conventional optical systems: Doubly negative metamaterials enable negative refraction of light [53-56]. A slab of negative unity refractive index exhibits the super-lens property [57-59]. Transformation optics gives a systematic design of electromagnetic cloaking via metamaterial [60-65]. Epsilon-near-zero and mu-near-zero metamaterials allow super-coupling in waveguides, highly directive emission, and enhanced nonlinearity [66-69]. These are just a few examples of fascinating aspects of metamaterials.

However, there is so far no nanofabrication technique of three-dimensional assembly of optical meta-atoms for mass production. Instead, state-of-the-art semiconductor fabrication techniques are served as the platform of making two-dimensional optical metamaterials. The two-dimensional metamaterials are called metasurfaces, and this subfield has been extensively studied in the last decade [70-99]. Metasurfaces are composed of single-layer or few-layer stacks of planar arrangements of optical meta-atoms with sub-wavelength thickness. Incident light on metasurfaces undergo little propagation phase because of optically negligible thicknesses, and strong light-matter interaction caused by resonant meta-atoms gives abrupt response on the incident wave. In turn, optical response of metasurfaces are described in the form of surface properties.

Researchers have been investigated to show that metasurfaces have potential to shape reflected and/or refracted wavefronts with arbitrary phase, amplitude, and polarization distributions. Especially, many reports are published on metasurface-based hologram generation in recent years [79-83]. It is expected that the meta-

holograms have extremely wide-angle property because of the subwavelength distance between meta-atoms. More importantly, complex modulation of light enables dual-image-free, speckle-free, and extremely low-noise generation of computer generating hologram (CGH) without any time-consuming iterative algorithms. I have to mention that research on metasurfaces covers much broader area of interest. Frequency selectivity, polarization conversion, and huge nonlinearity on metasurfaces have been also investigated in depth [84-92].

Finally, there has been similar approach on the one-dimensional metamaterials: meta-slits. In analogy with metasurfaces, meta-slits are originally proposed to generate various plasmonic field distributions. A flat interface of dielectric and metal supports surface plasmon polaritons (SPPs), which refer to single transverse-magnetic (TM) mode of light propagating along the surface of metal media [29, 93-97]. In other words, the term ‘plasmonic field’ refers to the distribution of electromagnetic waves excited nearby the surface of metal. The coherent plasmonic field of frequency f on an infinite metallic plane is described by scalar wave equation. This implies that SPPs have wave phenomena similar to three-dimensional optical phenomena. Generation, propagation, and modulation of SPPs are the key issues in the applications of integrated nano-photonics circuits, due to the extremely small mode area property and high data transmission rate of SPP-based devices [98-111]. Other applications of SPPs including plasmonic sensors [112], plasmonic focusing based nanolithography [113], plasmonic optical tweezers [114], plasmonic beam shaping [113, 115] also highly demand the modulation

capability of SPPs. Correspondingly, researchers have been extensively investigating on the fundamental properties and applications of meta-slits [116-123]. Unlike previous studies using conventional plasmonics, the meta-slits do not need much space of bulky optical parts to control incident wavefront, and they have full capability of complex amplitude modulation by meta-atoms with simple design.

1.2 Motivation and organization of this dissertation

In the previous section, I introduced the brief historical review of Huygens' principle and its implication to the optical diffraction theories. In modern optics, optical diffraction theories consistent with the Maxwell's equations still embrace the concept of secondary waves in Huygens' principle. Secondary waves are assumed to have amplitudes, radiation patterns, and possibly polarizations. As introduced in the later part of the previous section, metasurfaces and meta-slits have wavefront manipulation capability. Meta-atoms can be regarded as the sources of secondary waves.

Regarding the characterization of metasurfaces in the sense of wavefront manipulation, researchers found that 2-by-2 surface polarizability is sufficient to model local scattering process on the metasurfaces in their studies [124-130]. Relying on the equivalence theorem [30-37], with a given incident wavefront, the required induced surface currents on the metasurface are constructed by engineering meta-atoms to give the desired surface polarizability. I note that there is an implicit assumption on the surface polarizability modeling of metasurfaces: incident and reflected/refracted wavefronts have small spatial bandwidth. It is because most researchers are interested only with the scattering problems considering small portion of radiation pattern of meta-atoms. Then, radiation pattern of each meta-atom is equivalently presented by two complex amplitudes corresponding with two orthogonal polarizations. Under this assumption, polarization-dependent 2-by-2 scattering process is sufficient to model the optical

response of metasurfaces with the given direction of incident, reflected and refracted wavefront even though meta-atoms radiation patterns are different from each other.

Regarding supercell metasurfaces, each supercell is composed of a few meta-atoms to implement complex amplitude modulation of light in practical applications [131-133]. Each supercell has complex radiation pattern even if the incident wave has slowly varying wavefront on the metasurface. Scattering process of meta-atoms having complex structure is characterized by multipole components [134-138]. In these cases, justification of the ignorance of radiation patterns are not enough to generate optical and plasmonic wavefronts with broadband spatial bandwidth via metasurfaces and meta-slits. Most previous studies on effect of the radiation pattern of meta-atoms have focused on efficiency [137], directive emission [132], and diffusive emission [133], not distortion and noise. Moreover, potential applications including meta-holograms raise demands on the capability of generating spatially broadband wavefronts.

Therefore, the motivation of this dissertation is to investigate the advantages of taking account of radiation patterns of meta-atoms in metasurfaces and meta-slits. It is supposed that irregularity of radiation patterns of meta-atoms causes distortion of generated wavefronts, regularization of meta-atoms would be the essential part to realize generation of arbitrary optical and plasmonic wavefront with extremely low noise. The objective of this dissertation is to propose novel methods of rigorous generation of optical and plasmonic field based on regularized

radiation patterns of meta-atoms in metasurfaces and meta-slits, respectively. The corresponding structures for realizing the proposed methods are suggested and examined by various ways: analytical modeling, full-field simulation, and experiments. Complex modulation mechanisms of meta-atoms compatible with the proposed methods are also discussed in depth. The scope of this dissertation is illustrated in Fig. 1.1.

| | Chapter 4 | Chapter 5 |
|---|----------------------------------|-----------------------------------|
| Subject | Plasmonic field synthesis | Optical field synthesis |
| Proposed structure | Metal-clad waveguide array | Nano antenna array |
| Type of metamaterials | Meta-slit (1D metamaterial) | Metasurface (2D metamaterial) |
| Meta-atoms | Edge of metal-clad waveguide | Nano-antennas |
| Chapter 2 Radiation patterns | Magnetic dipole-like | Electric dipole-like |
| Chapter 3 Modulation capability | Complex modulation | Complex modulation + polarization |
| Generated output | Arbitrary plasmonic field | Arbitrary optical field |

Figure 1.1 Scope of this dissertation

This dissertation is organized as follows: In Section 2.1, Huygens’ sources found in optical diffraction theories are discussed. The next section covers basic types of Huygens’ sources in metasurfaces and meta-slits. In Section 2.3, the term ‘regularization’ repeatedly used in this dissertation is defined. By assuming idealized Huygens’ sources, I propose a novel method to generate arbitrary optical and plasmonic wavefronts in Section 2.4.

The next chapter discusses how to give complex amplitude modulation to

meta-atoms with regularized radiation pattern. Starting from coherent perfect absorption (CPA) condition in plasmonic waveguide, a novel method to achieve complex amplitude reflection coefficient in two-dimensional and three-dimensional metal-clad waveguide is derived in Sec. 3.2. In these cases, the proposed waveguides have magnetic dipole-like radiation patterns at the open ends of the waveguides. This observation directly leads to the design of complex amplitude transmission coefficient in Section 3.3.

In Chapter 4, I propose a metal-clad waveguide array for realizing the method of generating arbitrary plasmonic field as discussed in Section 2.4. Complex amplitude modulation capability is implemented by a tilted input slit and circularly-polarized normally incident plane wave; radiation patterns are regularized by the open ends of metal-clad waveguides. In Section 4.3, the performance of the proposed structure is examined by noise analysis on the two cases: plasmonic focusing and truncated plasmonic Airy beam. Experimental suggestion is addressed in Section 4.4.

Synthesis of arbitrary optical field is more complex than that of arbitrary plasmonic field, due to additional degree of freedom: polarization. Complex amplitude modulation with arbitrary polarization is not currently available for optically thin metasurfaces. In Chapter 5, electric dipole metasurface is proposed to illustrate how to generate arbitrary optical wavefront with regularized meta-atoms. By using the proposed metasurfaces, optical focusing with high-NA, generation of Bessel-Gauss beam, and holograms are analyzed by noise analysis in Section 5.3.

More accurate form of electric dipole metasurfaces is derived in Sec. 5.4.2. In Section 5.5, nano-antenna arrays are examined as the realization of electric dipole metasurfaces. Experimental demonstration of the nano-antenna arrays introduced in Sec. 5.5. is delivered in Section 5.6.

In Chapter 6, I make summary and concluding remarks on this dissertation.

Chapter 2 Radiation patterns of Huygens' sources and its regularization process

2.1 Electromagnetic Huygens' sources

In this chapter, electromagnetic Huygens' sources are defined and characterized. By specifying radiation patterns of Huygens' sources, the ideal radiation pattern of Huygens' sources for noiseless generation of any electromagnetic fields are derived. Then, I will show that irregular radiation patterns of Huygens' sources are the cause of noise from conventional sampling-recovery process of electromagnetic field via metasurfaces and meta-slits. It is shown that regularized Huygens' sources, which have identical radiation patterns, can generate plane waves without noise. Realization of regularized Huygens' sources will be discussed in the following chapter. It is helpful to start with summarizing the key results in the diffraction theories which were briefly introduced in Sec. 1.1.

2.1.1 Key results in Huygens' principle based optical diffraction theories

The Huygens-Fresnel equation on the optical diffracted field constructed by superposing secondary waves is as follows:

$$U(P) = \frac{i}{\lambda} U(r_0) \int_S \frac{e^{-ik_0 s}}{s} K(\chi) dS, \quad (2.1)$$

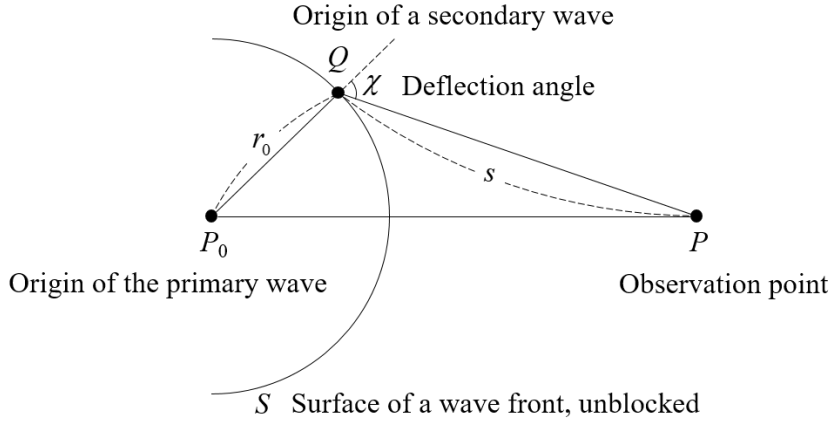


Figure 2.1 Illustration of the Huygens-Fresnel equation in Eq. 2.1.

where parameters are illustrated in Fig. 2.1. Considering the case that a spherical primary wave with wavelength λ is generated by a point source at a point P_0 , the complex amplitude of the primary wave at a distance r_0 from P_0 is assumed to be $U(r_0) = U_0 r_0^{-1} e^{-ik_0 r_0}$. Equation 2.1 means that the complex amplitude of the diffracted wave at a distant point P can be obtained by the superposition of the unblocked secondary waves from the surface of the sphere S centered at P_0 with the radius r_0 . Each secondary wave radiates light wave with a multiplication factor $K(\chi)$ which is called the inclination factor. χ denotes the deflection angle between the propagating direction of the primary wave and the propagating

direction of the secondary wave at a point Q on the surface S as depicted in Fig. 2.1.

Stokes pointed out that the inclination factor of optical ether is given by [11]:

$$K(\chi) = \frac{1}{2}(1 + \cos \chi), \quad (2.2)$$

whereas the Fresnel's original statement assumes the inclination factor satisfies $K(\chi = \pi/2) = 0$. Helmholtz exploits Green's second identity to get integral theorem of monochromatic waves as follows [13]:

$$U(P) = -\frac{1}{4\pi} \iint_S \left[U \frac{\partial}{\partial n} \left(\frac{e^{-iks}}{s} \right) - \frac{e^{-iks}}{s} \frac{\partial U}{\partial n} \right] dS, \quad (2.3)$$

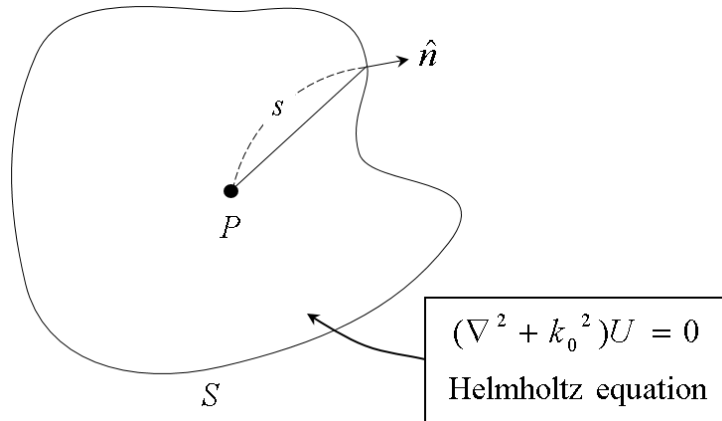


Figure 2.2 Parameters in the Kirchhoff-Helmholtz integral theorem (Eq. 1.3) for monochromatic scalar wave are illustrated.

where parameters are depicted in Fig. 2.2. Since the general formulation for the case of non-monochromatic wave is derived by Kirchhoff [14], Eq. 2.3 is called the Kirchhoff-Helmholtz integral theorem. Starting from Eq. 2.3, the Fresnel-Kirchhoff diffraction integral is obtained from Eq. 2.3 by adopting Sommerfeld radiation condition and Kirchhoff's boundary conditions on perfectly absorbing screen [9, 10, 14]. Suppose a monochromatic point source $U = Ar^{-1}e^{-ikr}$ with center P_0 is diffracted by an opaque screen with the opening \mathcal{A} , the diffracted field is calculated according to the Fresnel-Kirchhoff diffraction integral as follows:

$$U(P) = -\frac{iA}{2\lambda} \iint_{\mathcal{A}} \frac{e^{-ik(r+s)}}{rs} [\hat{n} \cdot \hat{r} - \hat{n} \cdot \hat{s}] dS, \quad (2.4)$$

where geometrical parameters are illustrated in Fig. 2.3.

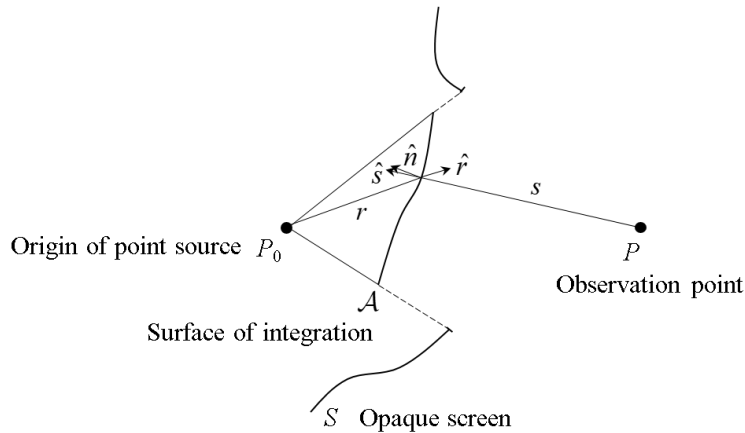


Figure 2.3 Illustration of the Fresnel-Kirchhoff diffraction integral

The importance of the Fresnel-Kirchhoff diffraction integral is that inclination factor for diffracted field is explicitly derived in accordance with Stokes' one in Eq. 2.2 if the surface of integration \mathcal{A} is an equidistant surface with center P_0 .

Various types of corrections have been made to improve the Kirchhoff's diffraction theory of light. Rayleigh (1896) and Sommerfeld (1954) made integral formulas which are called the Rayleigh-Sommerfeld diffraction integrals [15-17].

Since light as the form of electromagnetic wave follows vector wave equation in free space, vector optical diffraction theories have been proposed by many researchers [10, 18-37]. Surface equivalence principle gives the correct secondary sources with physical radiation patterns consistent with the Maxwell's equations [30-37]. Suppose that there are two connected region I and II separated by a boundary as illustrated in Fig. 2.4. The two regions have source-free electromagnetic field solutions (\vec{E}_1, \vec{H}_1) and (\vec{E}_2, \vec{H}_2) . Then, on the boundary, surface current density \vec{J}_s and surface magnetic current density \vec{M}_s connect two independent solutions consistent with the Maxwell's equations as

$$\begin{cases} \vec{J}_s = \hat{n} \times (\vec{H}_2 - \vec{H}_1) \\ \vec{M}_s = (\vec{E}_2 - \vec{E}_1) \times \hat{n}. \end{cases} \quad (2.5)$$

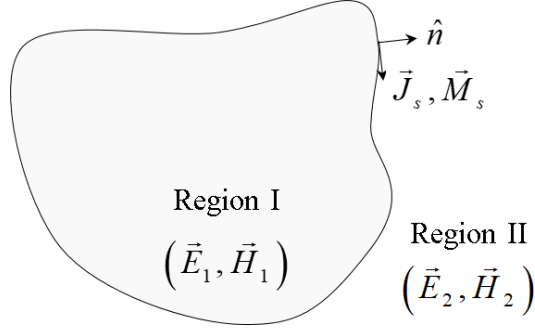


Figure 2.4 Illustration of surface equivalence principle

This boundary source can be used to formulate vector diffraction theory of light. For example, if a screen is either perfect electric conductor (PEC) or perfect magnetic conductor (PMC), the surface of the opening only contributes to the diffracted field in the sense of Huygens' principle. According to the Franz formula [19, 37], the diffracted field is given as follows:

$$\begin{cases} \vec{E}(\vec{r}) = \vec{\nabla} \times \iint_{\mathcal{A}} (\hat{n} \times \vec{E}_{\text{inc}}) g dS' + \frac{-i}{\omega \epsilon} \vec{\nabla} \times \vec{\nabla} \times \iint_{\mathcal{A}} (\hat{n} \times \vec{H}_{\text{inc}}) g dS' \\ \vec{H}(\vec{r}) = \vec{\nabla} \times \iint_{\mathcal{A}} (\hat{n} \times \vec{H}_{\text{inc}}) g dS' + \frac{-i}{\omega \mu} \vec{\nabla} \times \vec{\nabla} \times \iint_{\mathcal{A}} (\hat{n} \times \vec{E}_{\text{inc}}) g dS', \end{cases} \quad (2.6)$$

where $g = \exp(-ik|\vec{r} - \vec{r}'|) / 4\pi|\vec{r} - \vec{r}'|$, and incident field $(\vec{E}_{\text{inc}}, \vec{H}_{\text{inc}})$ is blocked by an opaque screen S and thus passes through the opening \mathcal{A} . $\vec{J}_s = \hat{n} \times \vec{H}_{\text{inc}}$ and $\vec{M}_s = \vec{E}_{\text{inc}} \times \hat{n}$ are considered as the sources of diffracted field.

In conclusion, surface current (magnetic current) density is equivalently surface density of electric (magnetic) dipoles, tangential electric and magnetic

dipole sheet on any surface can generate field which is same as the corresponding diffraction problem.

2.1.2 Definition and characterization of Huygens' sources

As discussed in the previous subsection, the original statement of secondary waves in the Huygens' work did not specify the waveform of the secondary waves. Thus, the definition of Huygens' sources in electromagnetic waves should be given as any electromagnetic point sources consistent with Maxwell's equations. Any hypothetical point sources are considered as the source of secondary waves.

One of the most convenient way to characterize Huygens' sources is exploiting multipole expansion method [28]. In general, all the amplitudes of multipoles are needed to fully characterize a Huygens' source. The most fundamental and natural choice of Huygens' sources would be magnetic and electric dipole sources. Electric dipole moment \vec{p} and magnetic dipole moment \vec{m} with their own radiation patterns fully characterize optical response of these simple types of Huygens' sources. For example, electric dipole Huygens' sources have electric dipole moment \vec{p} with radiation pattern given by Greens' dyadic [29]:

$$\vec{E} = \int \vec{G}(\vec{r}, \vec{r}') \cdot \vec{p} \delta^{(3)}(\vec{r} - \vec{r}') dV' = \left\{ \left[\vec{I} + \frac{1}{k^2} \vec{\nabla} \vec{\nabla} \right] \frac{e^{-ik|\vec{r}-\vec{r}'|}}{|\vec{r}-\vec{r}'|} \right\} \cdot \vec{p}. \quad (2.7)$$

Similarly, magnetic dipole Huygens' sources have magnetic dipole moment

\vec{m} with radiation pattern as follows:

$$\vec{H} = \int \vec{G}(\vec{r}, \vec{r}') \cdot \vec{m} \delta^{(3)}(\vec{r} - \vec{r}') dV' = \left\{ \left[\vec{I} + \frac{1}{k^2} \vec{\nabla} \vec{\nabla} \right] \frac{e^{-ik|\vec{r}-\vec{r}'|}}{|\vec{r}-\vec{r}'|} \right\} \cdot \vec{m}. \quad (2.8)$$

These two types are realized by the concept of meta-atoms in metamaterials. According to the results of optical diffraction theories in the previous subsection, a periodic arrangement of meta-atoms corresponding to the surface dipole density can construct any electromagnetic field. In the next section, I would like to characterize examples of optical meta-atoms in terms of Huygens' sources.

2.2 Huygens' sources in meta-systems

As discussed in the previous section, Huygens' sources are defined by any local electromagnetic sources with multipole radiation components. The notion of meta-atoms perfectly fits into Huygens' sources. Sizes of meta-atoms are mostly fall into deep subwavelength regime. According to the Mie scattering theory [29], scattering by any object is decomposed into an infinite series of multipole radiation terms.

It should be noted that radiation pattern of Huygens' sources with multiple non-zero multipole terms is not preferred: it is because there is a possibility of existence of non-radiating direction of radiation. In turn, realizations of electric dipole only Huygens' sources and magnetic dipole only Huygens' sources by meta-atoms are needed. As pointed out in the previous section, the most fundamental and natural choice of Huygens' sources would be magnetic and electric dipole sources.

In the following, various types of meta-atoms as Huygens' sources are considered in both meta-slits and metasurfaces. It should be noted that optical properties of bulk metamaterials can be somewhat different from individual meta-atoms because mutual interaction between nearby meta-atoms can overwhelm their individual optical response.

2.2.1 Huygens' sources in meta-slits

On metallic plane, nanostructures such as bumps, dips, or apertures can transform incident wave into SPPs as in Fig. 2.5. Since SPPs are localized on metallic surface with TM polarization, consideration on shape of nanostructures and field

distribution of incident light is crucial to excite SPPs efficiently.

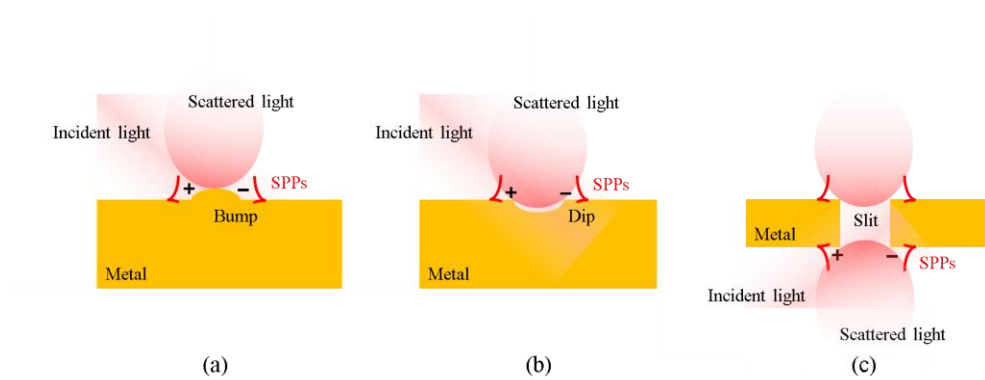


Figure 2.5 Illustration of simple nano-structures as meta-atoms in meta-slits: (a) bump, (b) dip, and (c) slit.

It is instructive to describe the case of excitation of SPPs by nano-apertures in more detail. Induced charge distribution determines radiation pattern of plasmonic field. As in the case of optical scattering decomposition by multipole expansion method, radiation pattern of plasmonic scattering can be decomposed by two-dimensional expansion method. Figure 2.6 depicts the cases for excitation of plasmonic field by illuminating polarized optical wave on various nano-apertures. As shown in Fig. 2.6(a), an arbitrarily shaped nano-aperture has complex induced charge distribution along the perimeter of it, in turn, radiation pattern of generated plasmonic field of the nano-apertures is determined by the induced charge distribution. Polarization and local field distribution of incident light can alter the induced charge distribution.

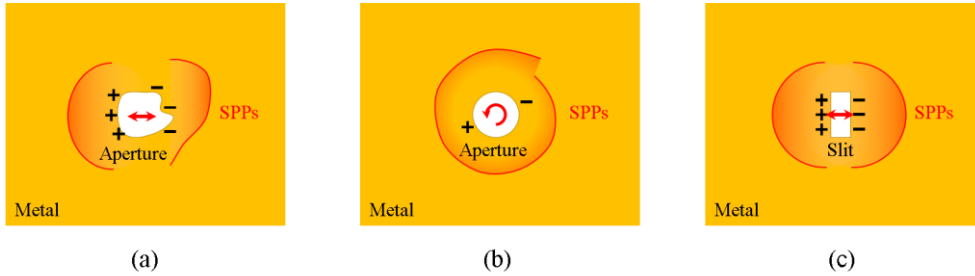


Figure 2.6 Top view of nano-apertures illuminated by polarized optical wave. (a) shape of nano-aperture affects induced charge distribution and consequently radiation pattern of excited SPPs, (b) polarization of incident light is also a key factor to alter radiation pattern, (c) nano-slit of moderate size radiates SPPs with magnetic dipole-like radiation pattern if it is illuminated by normally incident wave with polarization parallel to the minor axis of the nano-slit.

The most important case is shown in Fig. 2.6(c), where nano-slit of moderate size radiates SPPs with magnetic dipole-like radiation pattern, as inferred from Babinet's principle [28]. That is, small metallic or dielectric nano-rods of which sizes are smaller than half wavelength act as electric dipole Huygens' sources parallel to the major axis of the nano-rods; nano-slits as complementary structures for nano-rods act as magnetic dipole Huygens' sources parallel to the major axis of the nano-slits. In general, any edge of rectangular waveguide supporting only plasmonic TM modes has magnetic dipole-like radiation pattern if the size of

waveguide is not greater than a wavelength. In Chapter 4, this argument is formulated with two-dimensional dyadic of magnetic dipole Huygens' sources.

There have been numerous approaches to realize meta-atoms having complex amplitude modulation capability for plasmonic field synthesis. Notable example is the double-lined slit array that was suggested by Lee et al. [119]. Unit cell (meta-molecule) of the double-lined slit array in this case consists of two slits separated by a half wavelength. The author and co-workers argued that the proposed meta-slit generates any plasmonic wavefront with its complex amplitude modulation capability. However, such supercell structures have complicated radiation patterns, in turn, might generate intense background noise if supercell-based meta-slits are used for generating arbitrary wavefronts. I will examine this argument in depth in Chapter 4. To realize versatile meta-atoms, there have been numerous attempts that are not introduced in this subsection [116-123]. However, consideration on radiation patterns of meta-atoms has not been seriously addressed by researchers.

2.2.2 Huygens' sources in metasurfaces

As discussed in the previous section, electric dipole and magnetic dipole Huygens' sources can be realized by nano-rods or nano-slits, respectively. Figure 2.5(a) shows that nano-rods (nano-slits) have electric (magnetic) dipole moment along the major axis of the nano-rods (nano-slits).

According to Mie scattering theory, high index nano-rods can have multipole resonances even if their size is smaller than half wavelength. In addition,

complicated shape of a nanostructure affects its radiation pattern, so that high order multipole scattering components arise. A meta-molecule, defined by a group of meta-atoms, has non-trivial radiation pattern: interference of scattering patterns of meta-atoms, occlusion, and mutual interaction between meta-atoms affect radiation pattern of meta-molecules.

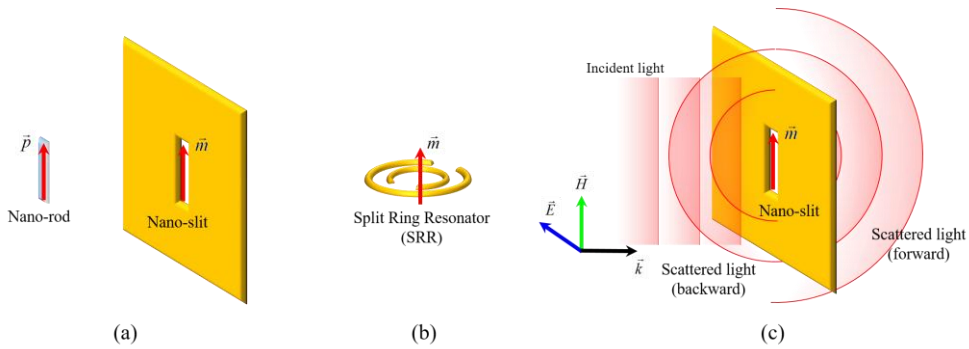


Figure 2.7 Examples of Huygens' sources in metasurfaces (a) nano-rod for electric dipole Huygens' sources and nano-slit for magnetic dipole Huygens' sources, (b) more complex nano-structure such as split ring resonator (SRR) has magnetic dipole-like radiation pattern around the resonance frequency. (c) Scattering process of nano-slit.

Figure 2.7(b) shows a classic example of resonant meta-atoms for achieving artificial magnetism around the resonance frequency. In Fig. 2.7(c), scattering process of nano-slit is illustrated.

In Chapter 5, nano-rods are used to implement in-plane electric dipole

metasurfaces. It should be noted that a similar approach can be made with in-plane magnetic dipole metasurfaces realized by nano-slit arrays.

2.3 Regularized radiation patterns of Huygens' sources

In this section, I define the term ‘regularization’ and discuss about how to utilize regularized radiation patterns of Huygens' sources placed in a periodic array for low-noise generation of optical fields. For fixed frequency f , the optical wave field generated from an array of Huygens' sources with complex amplitudes is represented as

$$\vec{\psi}_{\text{synt}}(\vec{r}, \omega) = \sum_{p,q} \vec{G}_{p,q}(\vec{r}, \vec{r}_{p,q}) \cdot \vec{a}_{p,q}, \quad (2.9)$$

where Huygens' sources are placed at periodic grid points $(x, y) = (p\Lambda, q\Lambda)$ on the plane $z=0$, and the corresponding complex amplitudes with polarization are represented as $\vec{a}_{p,q}$. Radiation pattern of each Huygens' source is $\vec{G}_{p,q}$.

If each radiating profile can be set to a mathematically equal Huygens' source function $\vec{G}_{p,q} = \vec{G}_{\text{reg}}$, then the generated field $\vec{\psi}_{\text{synt}}$ can be represented by the two-dimensional convolution of the sampled pulse train of the original field and the unit dipole field, given as

$$\vec{\psi}_{\text{synt}} = \vec{G}_{\text{reg}}(\vec{r}, 0) *_{x,y} \left[\sum_{p,q} \vec{a}_{p,q} \delta(\vec{r} - \vec{r}_{p,q}) \right], \quad (2.10)$$

where the asterisk signifies two-dimensional convolution. Here, any process that

makes all radiation patterns of Huygens' sources same with each other is referred to as *regularization* of Huygens' source array. In this section, it is assumed that regularized Huygens' source array is available. In Fourier domain, Eq. 2.10 is equivalently

$$\mathcal{F}_{x,y}\{\tilde{\psi}_{\text{synt}}\} = \mathcal{F}_{x,y}\{\tilde{\mathbf{G}}_{\text{reg}}\} \cdot \mathcal{F}_{x,y}\left\{\sum_{p,q} \vec{a}_{p,q} \delta(\vec{r} - \vec{r}_{p,q})\right\}. \quad (2.11)$$

The complex amplitudes may be regarded as periodically sampled amplitudes of a wavefront. In this section, I deal with the case that complex amplitudes are slowly varying. If a plane wave with transverse electric (TE) polarization is considered as the sampled wavefront, $\vec{a}_{p,q} = (k_x \hat{x} + k_y \hat{y}) e^{-i(k_x p \Lambda + k_y q \Lambda)}$.

Relying on the Nyquist sampling theory, the sampling period Λ should be less than a half wavelength $\lambda/2$. Then, Fourier component of the resultant wavefront is given as

$$\tilde{\tilde{\psi}}_{\text{synt}} = \left[\tilde{\tilde{\mathbf{G}}}_{\text{reg}}(k_x \hat{x} + k_y \hat{y}) \right] \cdot (k_x \hat{x} + k_y \hat{y}), \quad (2.12)$$

where tilde refers to two-dimensional Fourier transform. That is, the resultant wavefront is also plane wave with the same wavevector and polarization as the sampled wavefront without noise. It should be noted that the regularized radiation pattern determines efficiency with respect to the wavevector and polarization of the sampled plane wave.

Since any optical wavefront can be represented by superposition of plane

waves of all spatial frequency and regularized Huygens' sources can be straightforwardly superposed, the regularization process opens up the possibility of perfect synthesis of any wavefront.

Finally, I remark that generation of arbitrary plasmonic field can be treated in the same fashion except the polarization, since dynamics of plasmonic field on a flat metallic plane can be described by scalar wave equation.

2.4 Arbitrary field generation via ideal Huygens' sources

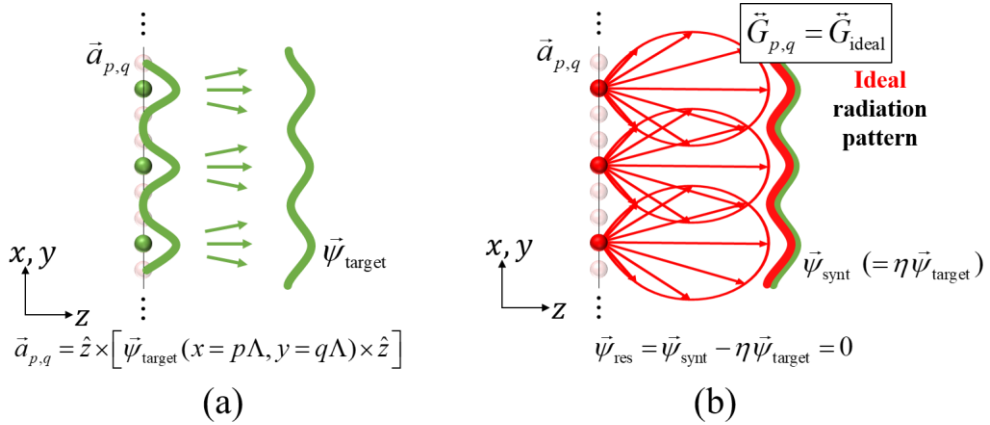


Figure 2.8 (a) Illustration of sampling process of a target wavefront (green) by meta-atoms, and (b) Reconstructed field (red) via ideal Huygens' source array is proportional to the target field.

In this section, I propose a novel method for noiseless generation of arbitrary optical and plasmonic field by defining ideal Huygens' source array that is

regularized and has the unique radiation pattern. As discussed in the previous section, regularized Huygens' sources can be exploited to generation of plane wave without distortion. Since superposition of regularized Huygens' sources is straightforward, arbitrary field generation with extremely low loss is achievable by applying regularized Huygens' sources.

As in the sampling process, complex amplitude with polarization of each Huygens' source $\vec{a}_{p,q}$ picks a local field profile at the position as $\vec{a}_{p,q} = \vec{\psi}_{\text{target}}(x = p\Lambda, y = q\Lambda)$, and the target field $\vec{\psi}_{\text{target}}(x, y)$ is supposed to be bandlimited. Then, the synthesized field is presented as:

$$\vec{\psi}_{\text{synt}} = \vec{G}_{\text{reg}}(\vec{r}, 0) *_{x,y} \left[\sum_{p,q} \vec{\psi}_{\text{target}}(\vec{r}) \delta(\vec{r} - \vec{r}_{p,q}) \right]. \quad (2.13)$$

To reconstruct the perfect target field such that $\vec{\psi}_{\text{synt}} = \eta \vec{\psi}_{\text{target}}$, it is needed to state the mathematical condition of the unit Huygens' source for perfect reconstruction in Fourier domain. As seen in Fig. 2.8, the angular spectrum of the radiation pattern of ideal Huygens' source \vec{G}_{ideal} with polarization α , is explicitly given as $\vec{G}_{\text{ideal},\alpha} \Big|_{z=0} := \mathcal{F}_{x,y} \left\{ \vec{G}_{\text{ideal}} \cdot \hat{\alpha} \right\} \Big|_{z=0} = \eta U_{k_0}(\vec{k}_{\perp}) \hat{\alpha}$, or equivalently,

$$\mathcal{F}_{x,y} \left\{ \vec{G}_{\text{ideal}} \right\} = \eta U_{k_0}(\vec{k}_{\perp}) \vec{I}, \quad (2.14)$$

where \otimes symbol is used for the tensor product. $U_{k_0}(\vec{k}_{\perp})$ is an indicator function of transverse wavevector having the value 1 for $|\vec{k}_{\perp}| \leq k_0$ and the value 0 for

otherwise. Any Huygens' sources having the radiation pattern as in Eq. 2.14 are called ideal Huygens' sources.

In the analysis, it is assumed that the sampling of complex amplitude is perfect, thus the noise field is induced only by the non-ideal radiation patterns of Huygens' sources. The focus of the analysis is the effect of the non-ideal Huygens' source in the field synthesis. The noise field is then defined as the residual field over the original target field given by

$$\vec{\psi}_{\text{res}} = \vec{\psi}_{\text{synt}} - \eta \vec{\psi}_{\text{target}} = \sum_{p,q} [\vec{G}_{p,q} - \vec{G}_{\text{ideal}}](\vec{r}, \vec{r}_{p,q}) \cdot \vec{a}_{p,q}. \quad (2.15)$$

However, it is worth to note that the gratings that form a periodic array of non-ideal but identical Huygens' sources can generate nearly collimated and noise-reduced wave field even though their single radiation unit generates non-ideal Huygens' sources.

If ideal Huygens' sources are unavailable, regularized radiation patterns of Huygens' sources take place. In this case, the ratio between $\vec{G}_{\text{reg}}(\vec{k}_{\perp})$ and $\vec{G}_{\text{ideal}}(\vec{k}_{\perp})$ should be systematically compensated in the sampling process. In this subsection, I do not specify the regularized radiation pattern of Huygens' sources. The detailed compensation process is explained in Chapter 5.

2.5 Conclusion

In this chapter, the term ‘Huygens’ source’, that is used throughout this dissertation, is defined as an electromagnetic point source consistent with the Maxwell’s equations. According to the historical overview in Sec. 2.1.1, secondary sources in various optical diffraction theories are hypothetical point sources to decompose local contribution from a specified diffraction surface to the diffracted field. Amplitude and radiation pattern of secondary sources is chosen quite arbitrarily. However, electric dipole and magnetic dipole are the natural choice of Huygens’ sources, according to the vector optical diffraction theory and surface equivalence principle. In metasurfaces and meta-slits, meta-atoms can be served as Huygens’ sources by definition. Then, I define the term ‘regularization’ by homogenizing process of radiation patterns of meta-atoms. Arbitrary field generation by ideal Huygens’ sources is proposed in Sec. 2.4. Regularized Huygens’ sources can be applied, however, how to construct Huygens’ sources to generate arbitrary plasmonic and optical field with extremely low ratio will be addressed in Chapter 4 and 5, respectively.

Chapter 3 Design of regularized Huygens' source

3.1 Introduction

In the previous chapter, I discussed Huygens' sources in metasurfaces and metaslits, and the regularization process of radiation patterns of meta-atoms is defined. Then I proposed a method of the generation of arbitrary optical and plasmonic field using regularized meta-atoms. In this chapter, I firstly explore implementation of complex amplitude reflection/transmission coefficient of metallic waveguide by exploiting coherent perfect absorption (CPA) condition in plasmonic waveguides. In the next section, I will propose the method to realize complex amplitude modulation via CPA.

3.1.1 Scattering process of parallel metal strips in 2D MIM plasmonic waveguide

In this subsection, parallel metal strips are considered as a candidate of coherent perfect absorber in 2D MIM waveguide. Firstly, I describe the scattering process of the proposed CPA structure in 2D MIM plasmonic waveguide. Figure 3.1 shows the parallel embedded metal strips in a two-dimensional MIM plasmonic waveguide. The MIM plasmonic waveguide has a subwavelength-thick dielectric

core, sandwiched by metal claddings, which is designed to forbid the propagation of the photonic modes. The MIM waveguide sustains two plasmonic modes, of which field distribution is evanescent both in metal and dielectric region. One of them is the magnetic field symmetric (fundamental) MIM mode, and the other is the anti-symmetric mode. Subwavelength thickness of the core is needed to obtain extreme confinement and it ensures that the anti-symmetric mode is cut-off or decayed much faster than symmetric one [139, 140]. Since dimension of the proposed structure is chosen as not greater than 250 nm, concerned mode is always magnetic field symmetric in this study. It is noteworthy that the symmetric MIM mode undergoes weak loss with propagation length more than 40 μm in the considered near-IR region (1 μm –1.6 μm).

The CPA part consists of two parallel thin metal strips. Since there exists only one fundamental MIM mode, this configuration can be effectively supposed to be a two-port system, where the input and output modes are the fundamental modes propagating towards and against the CPA, respectively. Moreover, by the mirror symmetry of the CPA structure with respect to the x -axis, the scattering matrix of the system can be explicitly written as:

$$S = \begin{pmatrix} t & r \\ r & t \end{pmatrix}, \quad (3.1)$$

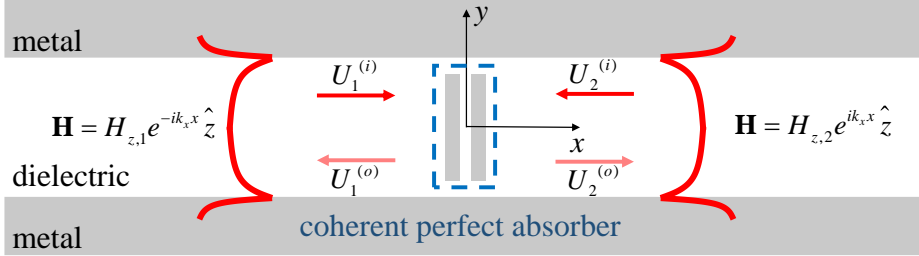


Figure 3.1 The proposed CPA embedded in an MIM plasmonic waveguide is depicted. Parallel metal strips absorb light via magnetic dipole resonance. Two metal strips should be close enough to hybridize their plasmonic resonances.

where r , t are complex reflection and transmission coefficients at the $x=0$ surface. The scattering process is expressed as:

$$U^{(o)} = \begin{bmatrix} U_1^{(o)} \\ U_2^{(o)} \end{bmatrix} = \begin{bmatrix} r & t \\ t & r \end{bmatrix} \begin{bmatrix} U_1^{(i)} \\ U_2^{(i)} \end{bmatrix}. \quad (3.2)$$

The eigenvectors of the scattering matrix represent symmetrically incident MIM mode, $U^{(i)} = (U_1^{(i)} \ U_2^{(i)})^T = (1 \ 1)^T$ and the anti-symmetrically incident MIM mode, $U^{(i)} = (1 \ -1)^T$, respectively. In the analysis, the scattering process occurs at the center position $x=0$. In practice, in order to obtain the effective scattering coefficients at $x=0$, the scattering amplitudes are calculated at $x=\pm 1 \text{ um}$, the positions distant from the center of the plasmonic absorbing structure, and convert them to the scattering coefficients, r and t , at $x=0$ with

the compensation of propagating loss and phase retardation. This assumption does not harm the simulation results if the plasmonic absorbing structure is thin enough.

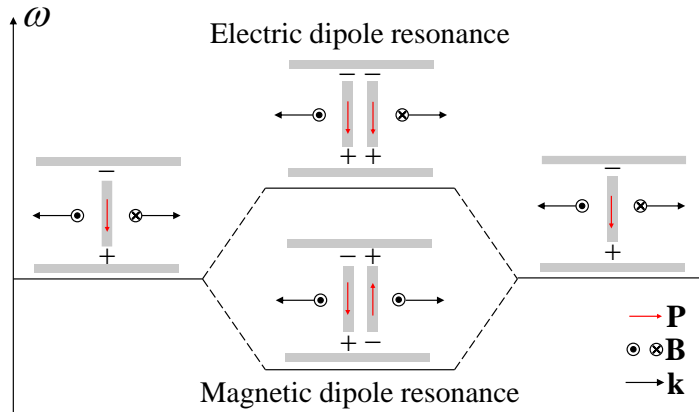


Figure 3.2 When the parallel metal strips embedded in the plasmonic waveguide are close enough, two resonant modes are hybridized into electric dipole resonance and magnetic dipole resonance, respectively. The two resonances are separated in the frequency domain (ω -axis). Polarization current (red arrows) and charge distribution (plus, minus sign) are indicated for each case.

Meanwhile, plasmonic resonances of two parallel metal strips are hybridized by interacting identical resonant structure pair, as depicted in Fig. 3.2 [140]. When the distance between the metal strips is far enough, the resonant modes of two strips are degenerate in the resonance frequency ω , and the electric dipoles are induced in each metal strip. If the strips are close enough to be optically coupled,

the coupled resonant modes are well-separated in ω -domain – one is the electric-dipole resonance at higher frequency and the other is the magnetic-dipole resonance at lower frequency. Field radiations from those induced dipole moments are obviously different. For the case of magnetic dipole resonance, the current loop formed by oppositely flowing current induces magnetic field through the parallel metal strips structure, so that it scatters waves such that $U_1^{(o)} = U_2^{(o)}$, which means that bidirectional waves propagating against the structure are in-phase with respect to the magnetic field, but out-of-phase with respect to the electric field at the same distance from the structure. On the other hand, for the case of electric dipole resonance, the electric field is in-phase and the magnetic field is out-of-phase at the same distance from the structure. In this case, induced currents on metal strips are in the same directions and do not form any current loop component.

According to the simple rule in the antenna theory that a good emitter is also a good receiver, it is expected that the proposed structure acts as a good absorber of symmetrically incident MIM modes ($U_1^{(i)} = U_2^{(i)}$) at the resonance frequency of magnetic dipole resonance. The amplitude of the induced magnetic dipole is proportional to the z -component of the magnetic field, penetrating through the current loop. On the other hand, since the electric-dipole resonant mode is well-separated in the frequency domain, the CPA absorbs little amount of energy of anti-symmetrically incident mode ($U_1^{(i)} = -U_2^{(i)}$) at the same frequency. The optimized structure shows perfect absorption for symmetric incidence and almost perfect transmission for anti-symmetric incidence. Such a high extinction property is

desirable for the design of amplitude switching devices.

3.1.2 Near-infrared magnetic dipole resonant coherent perfect absorption in 2D MIM plasmonic waveguide

As shown in the previous subsection, the scattering process of the proposed CPA structure in 2D MIM plasmonic waveguide is characterized by the symmetric 2-by-2 matrix S . This subsection deals with the CPA condition of the proposed structure and derivation of the corresponding structural parameters for given frequency.

Mathematically, the perfect absorption condition corresponds to the condition that one of the eigenvalues of scattering matrix S is zero. According to Eq. 3.1, one of the perfect absorption conditions is $r = t$, and the other is $r = -t$. The first case needs to have electric dipole resonance, and the second case corresponds to the magnetic dipole resonance when thin dipole sheet is concerned as in Fig. 3.2.

Defining a parameter $m = (r + t - 1) / 2$ for finding the magnetic resonant CPA condition. It represents the relative amount of symmetrically scattered light. If the CPA condition meets with $r = -t$, m is equal to $-1/2$. This condition is equivalent to the critical coupling condition [141] where loss rate and coupling rate should be equal to absorb incident power perfectly. There are three key observations to understand this parameter: (i) m is proportional to the strength of induced magnetic dipole on the structure, (ii) the structure behaves as a simple harmonic oscillator, and (iii) the structure is passive. From (i) and (ii), the frequency dependence of m can be modeled as $m = m_0 / (1 + i(\omega - \omega_0) / \gamma)$,

where m_0 is the relative amplitude of the symmetrically scattered light on resonance, γ is bandwidth or loss rate, and ω_0 is the resonance frequency. m_0 should be between -1 and 0 to satisfy (iii). For appropriate scattering amplitude, m_0 is equal to $-1/2$. Similarly, in the case of electric resonant CPA, the counterpart parameter of m , p is defined by $p = (-r + t - 1)/2$. The coherent perfect absorption condition for the electric resonant CPA is obtained at $p = -1/2$.

The introduction of the parameters p , m and the relationship between r , t , p , and m can be justified as follows. The total wave is assumed to be the superposition of incident wave and scattered wave. In the case of one-sided illumination, reflection coefficient r is equal to the relative amplitude of the scattered wave only and transmission coefficient t is sum of one and the relative amplitude of the scattered wave. Then there are two types of scattering process: electric dipole and magnetic dipole, the amplitudes of which are represented as p and m , respectively. Setting the relative amplitude of the scattered wave propagating toward the same direction with the incident wave has plus sign, the transmission and reflection coefficient in the magnetic field distribution are given by $t = 1 + p + m$, and $r = -p + m$, respectively. A simple algebra results in the representation of $m = (r + t - 1)/2$, and $p = (-r + t - 1)/2$.

As indicated in Fig. 3.2, the plasmonic hybridization puts the magnetic resonance energy to a lower energy level. Moreover, comparing the designs of electric dipole and magnetic dipole resonators working for a specific design

wavelength, it is inferred that the electric dipole resonance occurs with relatively long strip but the magnetic dipole resonance does with relatively short strip for the same resonance frequency, which relies on the fact that plasmonic resonance frequency of the structure is strongly dependent on the length of the strip. Thus, the use of magnetic dipole resonance is essential for the realization of CPA in the near-IR region within smaller footprint. It is noted that the high-order modes of metal strips are originated from the hybridization of high-order modes of the single metal strip, which tend to live in high frequency region. Also, the coupling from the incident mode to high-order modes are effectively inhibited by transverse wavevector mismatch between the incident field and the resonant field [141]. These unwanted higher-order effects are suppressed by choosing the length of the metal strips as small as possible, so that only electric and magnetic dipole resonances exist in the operating frequency region.

Figure 3.3 indicates the structural parameters that are tuned for optimizing the structure. Gold is chosen for the metal medium of both the waveguide and the CPA structure and its complex permittivity profile is obtained from the experimental data [142].

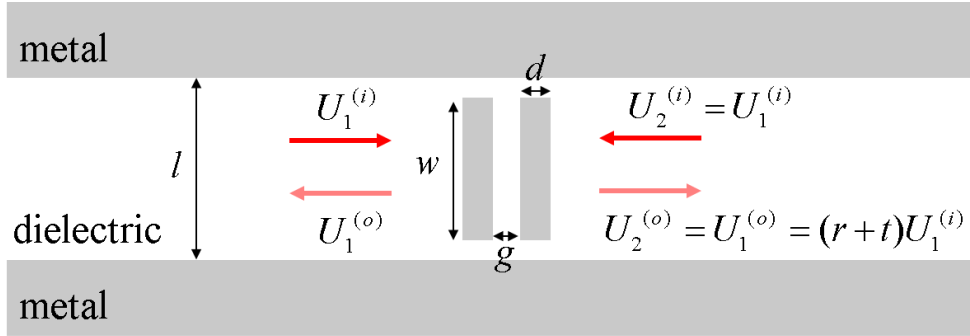


Figure 3.3 Illustration of the structural parameters and scattering process of the CPA structure illuminated by symmetrically incident mode.

As depicted in Fig. 3.3, there are four parameters to be varied: the dielectric core thickness l , the length of the strips w , the thickness of each strip d and the gap size g . To reduce the complexity of the parameter space, l is not used as an optimization target, but considered as a pre-determined value. l should be smaller than the operating wavelength to ensure the cut-off of the photonic modes. Moreover, l has to be barely longer than w to enhance coupling ratio. The parameters, w , d and g are related to the on-resonance frequency of the magnetic dipole ω_m . Hence, setting the three parameters to appropriate values can optimize the characteristics of the magnetic dipole resonance. w is almost solely dependent on the plasmon resonance of each metal strip. When gold is chosen for the metal media, it should be around 100 nm in order to make the resonances at the near-IR region. g determines the frequency separation between electric and magnetic

dipole resonance by plasmonic hybridization. Since the separation should be large to retain high extinction ratio, it is preferred for g to be sufficiently small. Typical value of g is below 30 nm long for plasmonic hybridization. Lastly, d is tuned for coherent perfect absorption condition. As d increases, the structure scatters light more in a proportional way. However, it does not indicate that the absorption ratio is also proportional to d .

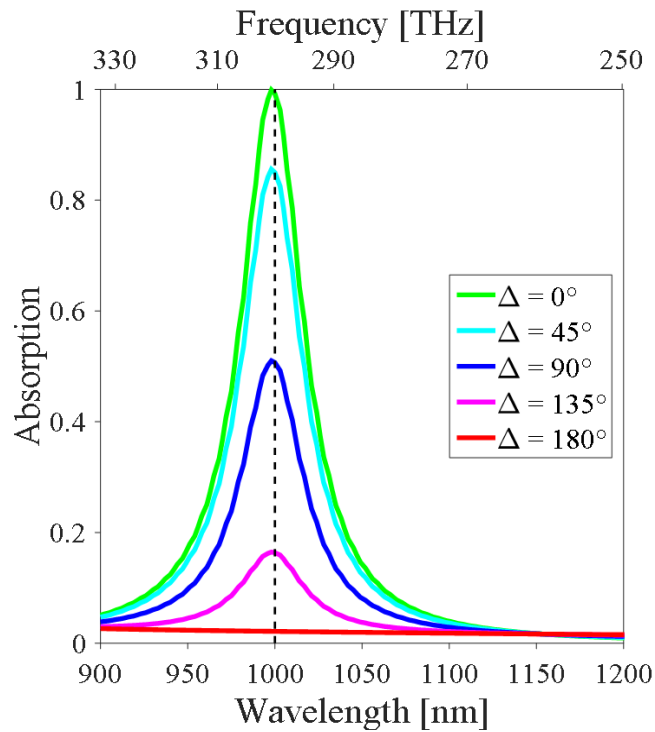


Figure 3.4 Absorption ratio of an optimized CPA structure against wavelength with different relative phase Δ . Values of the parameters are $d = 15$ nm, $w = 150$ nm, $g = 16.5$ nm, and $l = 200$ nm.

The CPA structure is derived with the Nelder-Mead method [143]. At target frequency ω_r , objective function is chosen as

$$f(l, w, g, d) = |m(\omega_r) + 1/2|^2. \quad (3.3)$$

If CPA condition lies on the parameter space, then its optimal value approaches to zero. As a result, the optimal structural parameters are derived as $w = 150$ nm, $d = 15$ nm, and $g = 16.5$ nm; and the corresponding absorption ratio is above 0.999 at wavelength 1 μ m. The commercial software COMSOL Multiphysics is employed for the optimization and analysis.

As shown in Fig. 3.4, when the phase difference of incident counter-propagating waves, Δ , is changed from 0 to π , then absorption ratio of CPA at the on-resonance frequency is modulated from the maximum value 1 to the minimum value near 0. The transmitted modes are represented by

$$U_{1(2)}^{(o)} = (r + te^{\pm i\Delta})U_{1(2)}^{(i)}. \quad (3.4)$$

Then, the absorption ratio can be simply formulated:

$$A = \cos^2 \frac{\Delta}{2} + A_0 \sin^2 \frac{\Delta}{2} \approx \cos^2 \frac{\Delta}{2}, \quad (3.5)$$

where A_0 is the absorption ratio when plasmonic waves are incident anti-symmetrically. This value can be ignored if g is small enough.

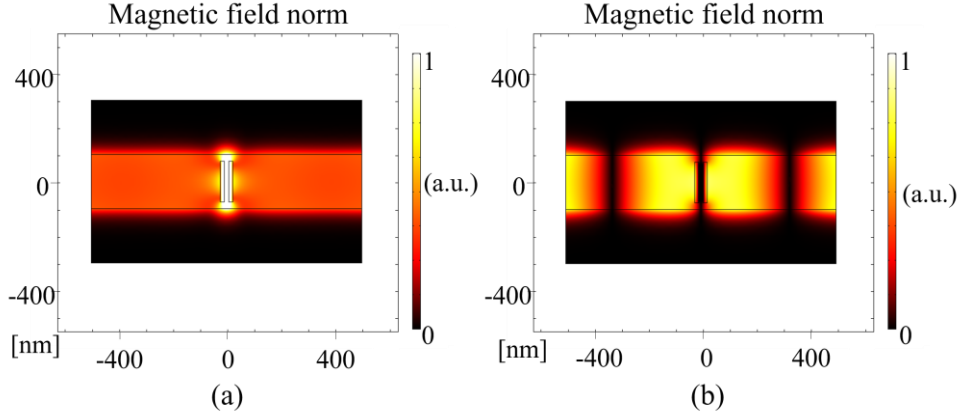


Figure 3.5 Magnetic field distribution of CPA structure for (a) symmetrically incident waves, $\Delta = 0$, and (b) anti-symmetrically incident waves, $\Delta = \pi$. The structural parameters are same as Fig. 3.4.

Not surprisingly, Fig. 3.4 depicts the dependence of the absorption ratio on the phase difference in accordance to Eq. 3.4. The magnetic field distributions in the CPA structure at $\Delta = 0$ and at $\Delta = \pi$ are shown in Figs. 3.5(a) and (b), respectively. The symmetrically incident MIM modes ($\Delta = 0$) produces the magnetic field distribution interfering constructively at the CPA structure ($x = 0$), while the anti-symmetrical incidence ($\Delta = \pi$) induces destructive interference and allows visible standing wave pattern formation in MIM waveguide. This simulation result is consistent with the qualitative analysis.

3.1.3 Frequency dependence of magnetic and electric dipole resonance

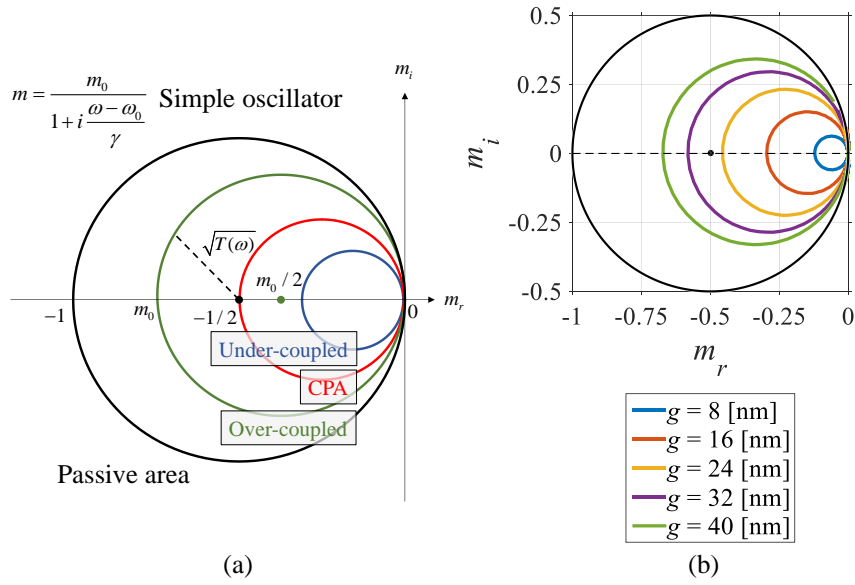


Figure 3.6 Manipulating the values of geometric parameters changes the scattering matrix S and frequency dependence of the complex-valued parameter m . (a) schematic of the trajectory of the parameter m , (b) numerical results derived from five different structures. The other parameters are fixed at $d = 10$ nm, $w = 160$ nm, and $l = 200$ nm.

As assumed in the previous subsection, the magnetic resonant dipole m is modeled as a simple harmonic oscillator. Then, the value of m can have a typical trajectory

of circle as graphically shown in Fig. 3.6(a), having the radius of $m_0/2$ and centered at $(-m_0/2, 0)$. When the symmetrical MIM mode input is applied, the amplitudes of out-coupled light from the CPA are given by $U_1^{(o)} = U_2^{(o)} = (r+t)U_1^{(i)}$, or $U_1^{(o)} = U_2^{(o)} = (m(\omega) - (-1/2))U_1^{(i)}$. In Fig. 3.6(a), the ratio of transmitted power over the total power is interpreted as the square of the distance between $(-1/2, 0)$ and $m(\omega)$. The CPA condition is achieved if the distance becomes zero, which can only be satisfied when the trajectory of $m(\omega)$ meets the point $(-1/2, 0)$, i.e. $m_0 = 1/2$ (red line in Fig. 3.6(a)). Also, there are blue line and green line that indicate under-coupled case and over-coupled case, respectively.

As an example of tuning m_0 , Fig. 3.6(b) shows the extracted complex values of m from the full-field simulation results for various gap size of the CPA. The circular loops of the calculated m indicate that the proposed CPA is well matched to the simple harmonic oscillator model, and they also show that the value of m_0 can be tuned by changing the structural parameters properly. According to the numerical results, it is found that the amount of the resonant hybridization can be arbitrarily tuned by changing the gap between the metallic strips, g .

For comparison, the same analysis on the parameter p is carried out. p stands for the complex amplitude of the anti-symmetrically scattered light in the electric resonant CPA. Figure 3.8(a) shows a single strip embedded in the same plasmonic MIM waveguide.

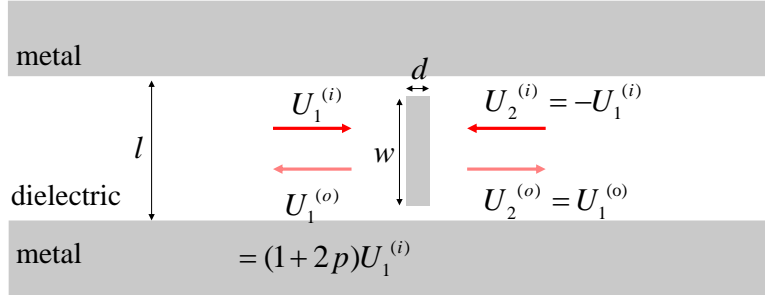


Figure 3.7 Illustration of a single strip embedded in a MIM waveguide with anti-symmetrically incident light.

In Fig. 3.8(a), the absorption efficiency for various d is plotted as a function of wavelength, which depicts that the single strip cannot absorb light effectively irrespective to the thickness, d . As seen in Fig. 3.8(b), the single-strip structure, i.e. electric resonant structure, is highly over-coupled. To achieve perfect absorption by electric dipole resonance at any cost, 1 nm order thick metal strip is needed as inferred from Fig. 3.8(b). This case is very unrealistic in various ways, size-dependent plasmonic loss, quantum effect, etc.

Similar analysis can be done for the electric dipole resonance of two metal strips. However, it is blue-shifted for reducing the distance d , so that it is not appropriate for near-IR operation with constraint of compactness. Moreover, electric dipole resonance is still in over-coupling regime no matter when the plasmonic structure is hybridizing two coupled metallic strips. Thus, electric dipole resonance is not considered as the plasmonic absorbing structure for low-loss waveguiding in near-IR region and for the use of critical coupling scheme.

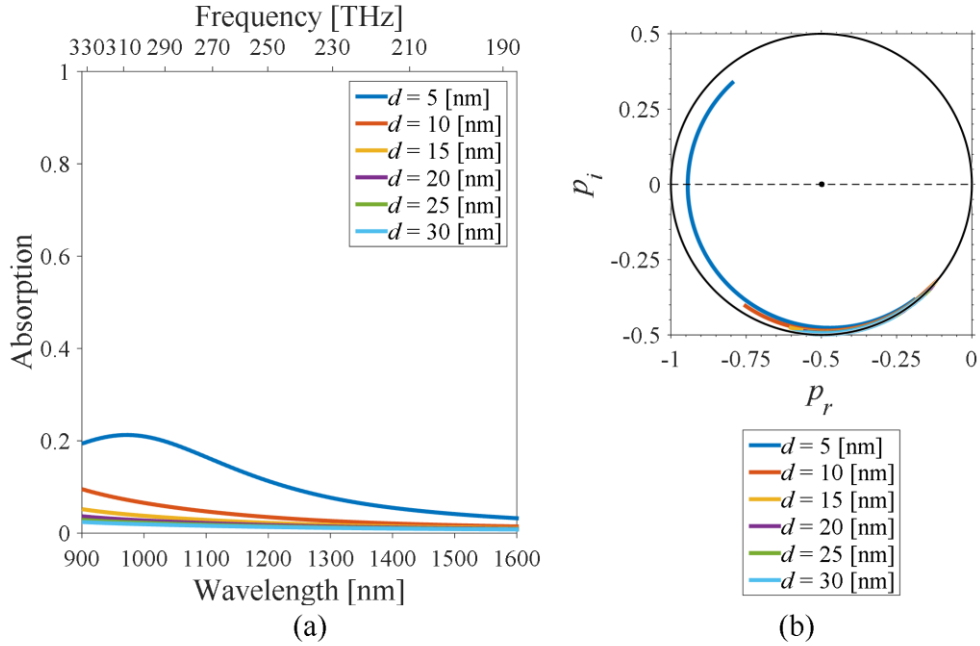


Figure 3.8 Numerical analysis on a single strip embedded in a MIM waveguide with anti-symmetrically incident light as in Fig. 3.7. (a) the absorption spectra of a single strip and (b) the corresponding trajectory of the complex-valued parameter p . The other parameters are fixed at $w = 150$ nm and $l = 200$ nm.

The observation from the comparison of magnetic and electric dipole resonances tells that the use of magnetic dipole resonance for CPA is superior to electric dipole resonance for two reasons. Firstly, the magnetic resonance structure can be gently tuned with the amount of plasmonic hybridization so that appropriate scattering amplitude for achieving CPA condition is achieved. Secondly, the

resonance peak of the magnetic dipole resonance can be flexibly adjusted from the resonance of single plasmonic structure at the near-IR region, so that the resonance is easily located at any wavelength of near-IR region in ultra-compact MIM waveguide structure.

3.1.4 Analysis of CPA characteristics in 2D MIM plasmonic waveguide

In this subsection, the dependence of the CPA spectra on the structural parameters are numerically analyzed. In this calculation, the absorption ratio is compensated to be not overestimated by the waveguide propagation loss. In Fig. 3.9(a), it is seen that the absorption spectrum is red-shifted as the length of strips grows and the peak value at on-resonance frequency is almost independent of w . The spectrum shifting seems to be ascribed to the Fabry-Pérot resonance. However, Fig. 3.9(b) presents that the thickness of metal strips, d , can change both the resonance frequency and the peak value at on-resonance. The aspect ratio of plasmonic structure affects depolarization factor, so on-resonance frequency is blue-shifted by growing d . Also, increasing d causes the enhancement of induced current on the metal strips, so that m_0 grows proportional to d . Absorption ratio is then quadratic with d . The peak value is maximum at the certain structural parameter, which satisfies the condition, $m_0 = -1/2$. As shown in Fig. 3.9(c), the resonance frequency is blue-shifted with g . Simultaneously, the scattering amplitude, m , increases with g because the magnetic dipole moment is proportional to the area of

circular current loop. Finally, Fig. 3.9(d) shows the absorption spectra of various CPA structures which are optimized for different on-resonance frequencies, from 1 μm to 1.6 μm . The design results show that the CPA condition in the proposed structure can be fit for broad range in near-IR band.

In this section, ultra-compact near-IR CPA based on plasmonic MIM waveguide is proposed with its design and analysis. The proposed CPA consists of parallel metal strips, which give a magnetic dipole resonance. It absorbs counter-propagating fundamental MIM plasmonic modes efficiently when magnetic field interferes constructively, which leads to produce ultra-compact near-IR CPA with excellent extinction ratio.

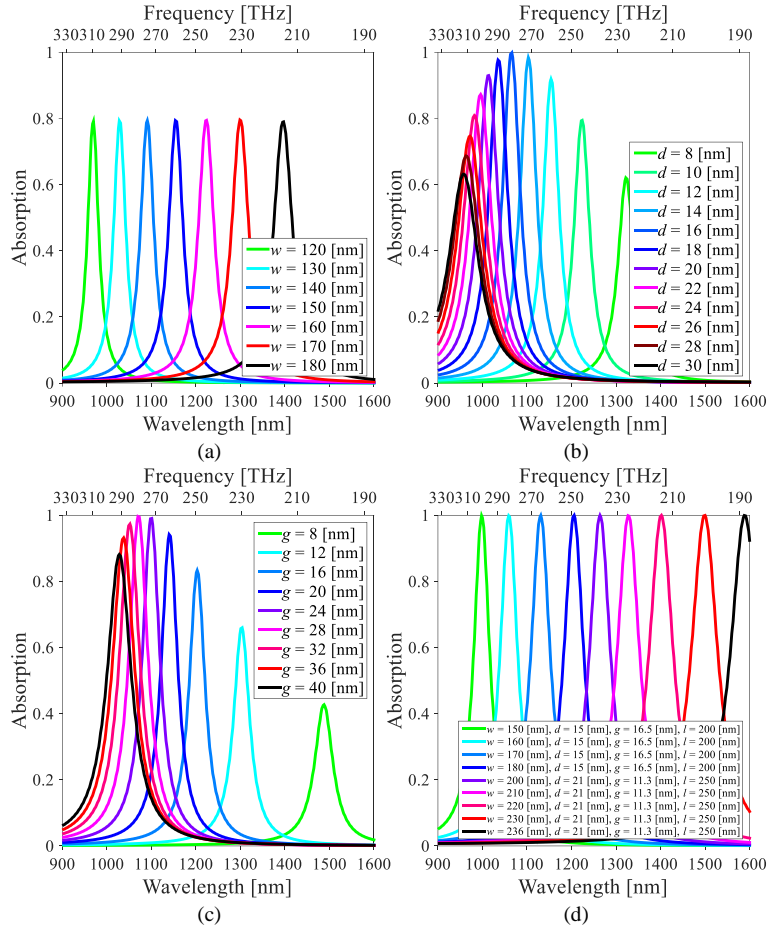


Figure 3.9 Absorption spectra of symmetrically incident waves in the proposed structure with varying (a) w , (b) d and (c) g . l is fixed at 200 nm. The other parameters are fixed at (a) $d = 10$ nm, $g = 15$ nm, (b) $g = 15$ nm, $w = 160$ nm, and (c) $w = 160$ nm, $d = 10$ nm. (d) Absorption spectra for various CPA structures with operating wavelength between 1 μm (green line) and 1.6 μm (black line)

3.2 Design of complex amplitude reflection coefficient of light in MIM plasmonic waveguide

In the previous section, magnetic dipole resonance of parallel metal strips was exploited to realize CPA condition in 2D MIM plasmonic waveguide. By engineering the structural parameters, resonance frequency and the peak amplitude of the magnetic dipole resonance m_0 are tuned in near-IR region. In the following subsection, the parallel metal strips can be exploited to design complex amplitude reflection coefficient of light in 2D MIM waveguide by introducing a metallic end. The other subsection is devoted to the 3D case: single metal antenna inside metal-clad waveguide as three-dimensional coherent perfect absorber.

3.2.1 2D waveguide with magnetic dipole resonator and metallic end

Consider a complex amplitude of a coefficient r that has full complex amplitude modulation capability. In other words, there exist at least two independent parameters $(p_i) \in P$ in the reachable parameter space P such that the corresponding coefficient $r(p_i)$ covers zero in the complex plane, and r_0 is defined as the largest complex number such that $B_{r_0}(0) \subset r(P)$ where $B_{r_0}(0)$ refers to a closed ball with radius r_0 center at 0 in the complex plane. For practical applications, continuous control is desirable. Thus, continuous control of

complex amplitude coefficient r with full complex modulation capability is realized by finding a subset of continuous parameter set P^* such that P^* is homeomorphic with $B_{r_0}(0)$ in the complex plane, where $r_0 \in \mathbb{R}$ is chosen as the largest one. Then, maximum amplitude modulation with full phase is r_0 by definition. Fig. 3.10 illustrates a case in which complex amplitude coefficient r is continuously modulated by two independent parameters p_1 and p_2 . It should be noted that efficient complex modulation needs high r_0 , and more isotropic P^* .

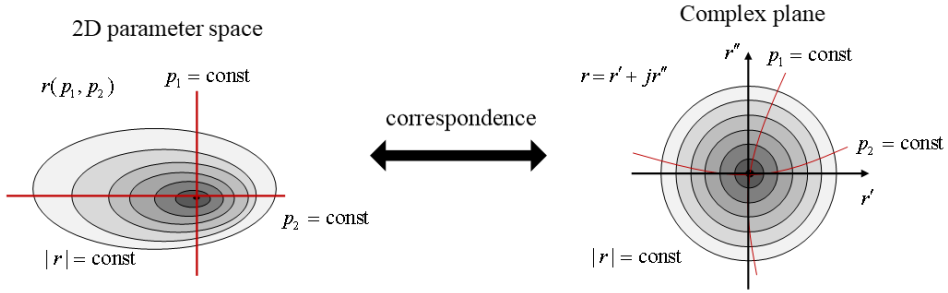


Figure 3.10 Illustration of continuous control of complex amplitude modulation of r by two dimensional parameters p_1 and p_2 .

Bearing above discussion in mind, I would like to realize complex modulation of light by exploiting CPA condition of the parallel metal strips in MIM 2D plasmonic waveguide. As discussed in the previous section, the parallel metal strips have many structural parameters to tune the scattering process. Moreover, the phase difference between two incident modes controls absorption in an extreme

way as presented in Eq. 3.5. I introduce a metallic end to the waveguide so that multiple scattering arises as in Fig. 3.11.

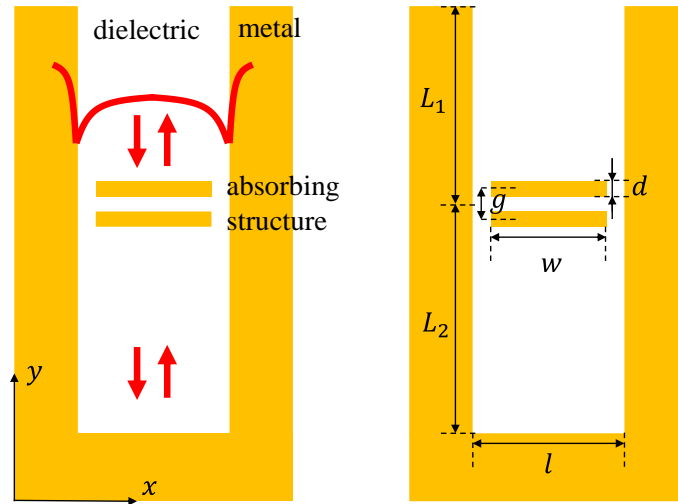


Figure 3.11 Illustration of (a) scattering process and (b) structural parameters of the proposed structure with complex amplitude reflection coefficient.

Then, a partial Fabry-Pérot (FP) cavity is formed. Trapped light inside the cavity is multiply reflected by the absorbing structure. The amplitude modulation can be obtained by tuning the length of the FP cavity (L_2). Then, the phase modulation is achieved by tuning the length between the absorbing structure and observing point (L_1).

Because the absorbing structure is same as the previous section, the scattering matrix of the absorbing structure is same as Eq. 3.1. With some calculation, the

overall reflection coefficient is given by

$$r_{\text{tot}} = r + \frac{t^2 e^{i(2k_{\text{MIM}}L_2 + \phi)}}{1 - r e^{i(2k_{\text{MIM}}L_2 + \phi)}} = r + \frac{t^2 r^*}{1 - |r|^2} + \frac{t^2 e^{i(2k_{\text{MIM}}L_2 + \phi)}}{1 - |r|^2}, \quad (3.6)$$

where k_{MIM} is the wavenumber of the MIM waveguide mode and ϕ is phase delay during the reflection. When the magnetic field at the absorbing structure is enhanced, the induced magnetic dipole moment is increased, and absorption can be enhanced for a certain level. Its trajectory along changing L_2 in complex plane draws a circle as depicted in Fig. 3.12.

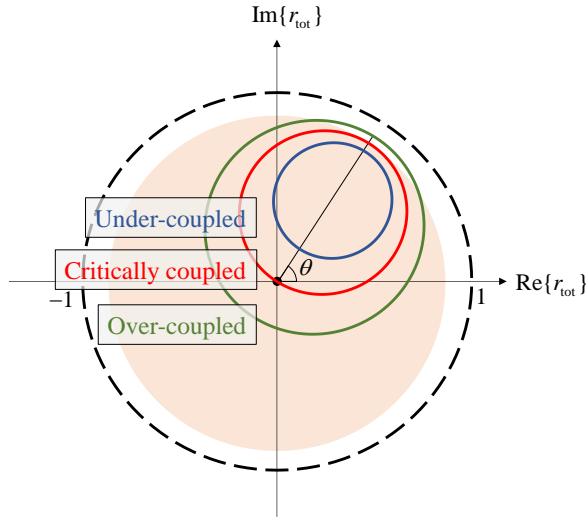


Figure 3.12 Trajectories of the overall reflection coefficient. If the absorbing structure is critically coupled (red line), full complex modulation (red filled circle) of light is realized.

When the geometrical parameters are optimized in order to make the trajectory pass through the origin, complete absorption of light is possible: the critically coupled condition. This condition is also found in the previous section as in Fig. 3.6. Only this condition makes full modulation of amplitude from zero to maximum. Moreover, the arbitrary value of phase (θ) is easily achieved if propagation length, L_1 , is introduced. Thus, full complex modulation is achieved by simply continuously changing only two structural parameters L_1 and L_2 . Numerical analysis confirms that the proposed structure properly works as intended. In this subsection, commercial finite element method (FEM) simulation tool (COMSOL Multiphysics 5.0) is used for calculating full-field simulation of the structure.

The operating wavelength is chosen as 1 μm , and other structural parameters are numerically optimized. The material used in metal cladding and the absorbing structure are assumed to be gold, of which the value is extracted from the experimental data [142].

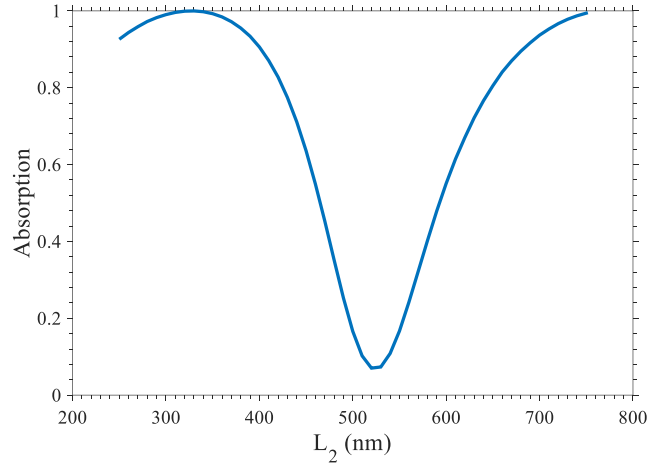


Figure 3.13 Absorption ratio characteristics of the optimized structure with respect to the parameter, L_2 .

The structural parameters of the optimized structure are $g = 18$ nm, $w = 152$ nm, $d = 15$ nm, and $l = 200$ nm. Figure 3.13 shows that the absorption modulation is accomplished by changing the structural parameter L_2 . The optimized structure accomplishes complete absorption of light so that the full amplitude modulation is possible.

Figure 3.14 depicts the region of the complex modulation by changing structural parameters L_1 and L_2 . L_1 is the key parameter for modulating the phase of the reflected wave. The red filled circle depicts the region of the complex modulation. The proposed structure achieves the full amplitude modulation from zero to 93 % of the input power, with arbitrary phase conditions. Finally, it is

noteworthy that the footprint of the structure is below $1 \mu\text{m}^2$ and the ultra-compactness of the structure is due to the strong plasmonic resonance in the absorbing structure.

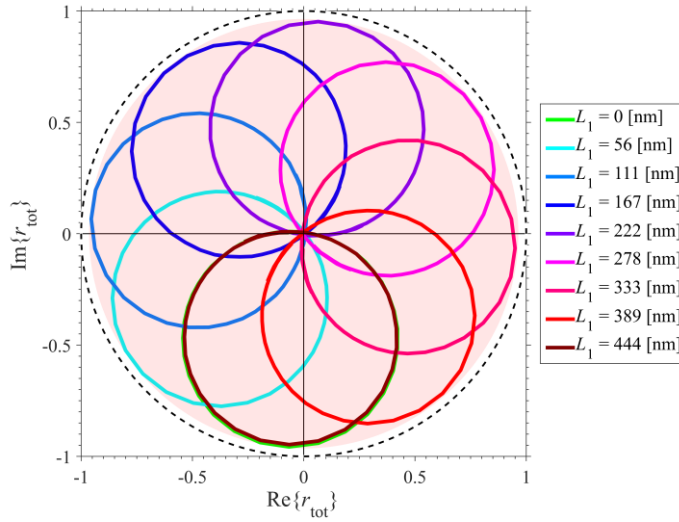


Figure 3.14 Trajectories of the overall reflection coefficient along L_2 , with different values of L_1 . The structural parameters are optimized to achieve critically coupled condition: $g = 18 \text{ nm}$, $w = 152 \text{ nm}$, $d = 15 \text{ nm}$, and $l = 200 \text{ nm}$.

I would like to conclude this subsection with some remarks. At first, I proposed a one-port structure for achieving full-range complex amplitude reflection coefficient, which can achieve the complete absorption of incident light. Numerical simulations show that translation of the absorbing structure modulates

the amplitude of the reflected wave, and addition of propagation length gives full-range of phase modulation. This study might be used to develop complex modulator with sub-micro sized pixels. It should be mentioned that radiation pattern at the open end of the waveguide is magnetic-dipole like. Moreover, overall reflection coefficient does not alter the form of radiation pattern. It means that this sub-micron sized structure can be regarded as a realization of regularized meta-atom with complex amplitude modulation capability. Second, it can be inferred that structures with negligible thickness are hard to achieve complex modulation capability. In the proposed structure, full phase modulation is possible by introducing additional propagation length L_1 .

3.2.2 3D waveguide with electric dipole resonator and metallic end

The proposed structure introduced in the previous subsection is generalized to the three-dimensional case. 3D plasmonic metallic antenna in three-dimensional metal-clad waveguide with a metallic end is a candidate for achieving complex amplitude reflection coefficient. It is because nano-antenna of moderate size offers under-coupled condition unlike 2D case as seen in subsection 3.1.3. In this subsection, it is assumed that metal media is made of gold.

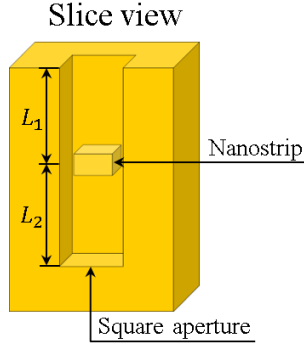


Figure 3.15 Schematic of the proposed cavity structure composed of nanostrip in a three-dimensional metal-clad plasmonic waveguide.

Firstly, size of the plasmonic waveguide is fixed as $500 \text{ nm} \times 500 \text{ nm}$ to guarantee that there are only two fundamental plasmonic modes at wavelength $\lambda = 1 \text{ }\mu\text{m}$, which are shown in Fig. 3.16. The square aperture waveguide supports M1 and M2 modes, and other higher order modes are evanescent. If x -polarized incident wave is considered, then M1 is of only interest. By symmetry, other modes cannot be excited during scattering process inside the cavity.

The optimization process of the proposed structure is same as the 2D case in Sec. 3.2.1. The optimized size of the nanostrip is $259 \text{ nm} \times 141 \text{ nm} \times 50 \text{ nm}$. With the optimized structure, the reflectance with respect to L_2 is shown in Fig. 3.17. For $L_2 = 632 \text{ nm}$, the reflectance is 0.78, and for $L_2 = 1012 \text{ nm}$, the reflectance is 0. In turn, full modulation depth is 78% while achieving CPA condition.

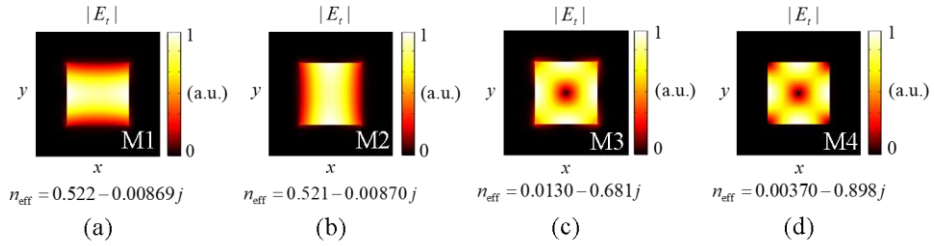


Figure 3.16 Four modes are the lowest order modes in the square aperture waveguide. (a) and (b) are propagation modes, and the others are evanescent modes.

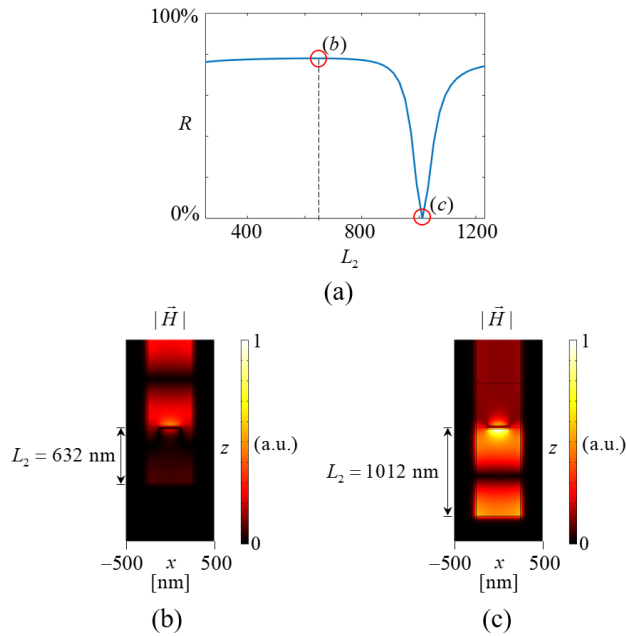


Figure 3.17 (a) Reflection characteristics of the optimized structure with respect to the parameter, L_2 .

Complex amplitude reflection coefficient is obtained by gradually changing L_1 and L_2 as shown in Fig. 3.18.

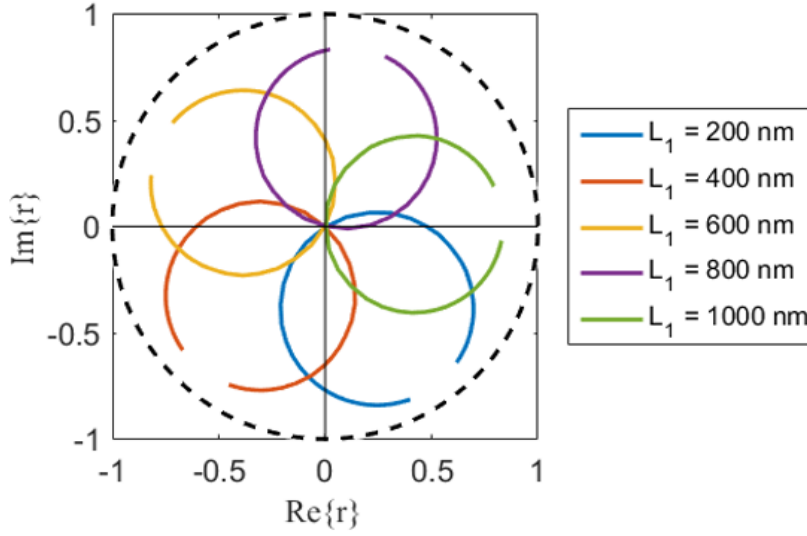


Figure 3.18 Complex modulation map of the reflection coefficient if the optimized nanostrip is inside the square aperture waveguide.

For practical applications, it is needed to account multiple scattering at the edge of waveguide. Reflection and transmission coefficients at the edge are illustrated in Fig. 3.19, then overall reflection ratio is formulated as

$$r_{\text{tot}} = r_s + \frac{t_s t_{\text{sp}} r \exp(-i2kL_1)}{1 - r_{\text{sp}} r_s \exp(-i2kL_1)}. \quad (3.7)$$

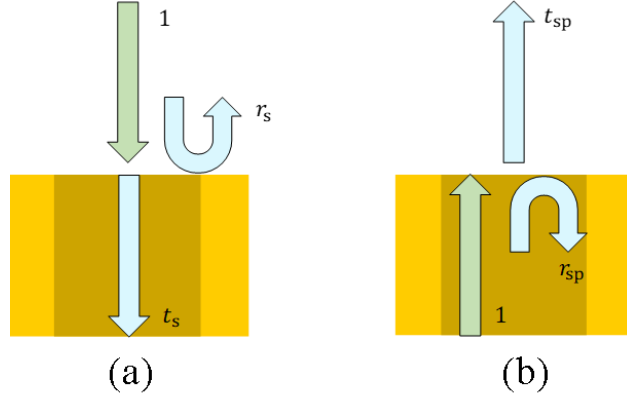


Figure 3.19 Illustration of reflection and transmission coefficient at the edge of the waveguide (slice view). (a) in-coupling, and (b) out-coupling.

Numerically extracted t_s , t_{sp} , r_s , and r_{sp} with periodic boundary condition can be exploited to calculate overall reflection coefficient of the cavity structure array without full-field calculation if unit cell size is selected to prohibit surface propagating modes at the interface. In practice, amplitude of r_s and r_{sp} is much less than 1 and r is small nearby the CPA condition, the overall reflection coefficient can be approximated by

$$r_{\text{tot}} \approx t_s t_{sp} r p^2 \propto r, \quad (3.8)$$

where p indicates propagating phase delay from the interface to the reference position where r is extracted. Then, the two-dimensionally arranged cavities with

all different reflection coefficients can be served as an metasurface with complex amplitude modulation capability for a fixed polarization. The design of individual reflection coefficient of cavities to generate optical wavefront is not given here, but it can be consulted in Chapter 5.

3.2.3 3D waveguide with asymmetric slit apertures

In the previous subsection, a floating nanostrip is served as an effective absorber, but fabrication of this configuration is not preferable. In this subsection, I would like to give an alternative structure for achieving CPA condition. Figure 3.20 shows the alternative structure that is composed of square aperture waveguide with asymmetric slit apertures at the end of the square aperture. The proposed structure is designed for visible region of light to achieve arbitrary complex-valued reflectance. The cavity is comprised of two parallel slit apertures with different depths, and it is attached to the end of the plasmonic square aperture.

The cavity utilizes interference effect between two slit modes, so that difference of the phase delay between two slit modes modulates coupling coefficient at the junction. It eventually changes both the phase and amplitude of the reflectance at the junction. If incident light is totally absorbed by multiple reflections, the depths of the slit apertures can be tuned nearby this perfect absorbing condition for an arbitrary complex-valued reflectance with full-range of both phase and amplitude. The structural parameters are given as $\Lambda = 450 \text{ nm}$, $a_x = a_y = 220 \text{ nm}$, and $b_x = 90 \text{ nm}$.

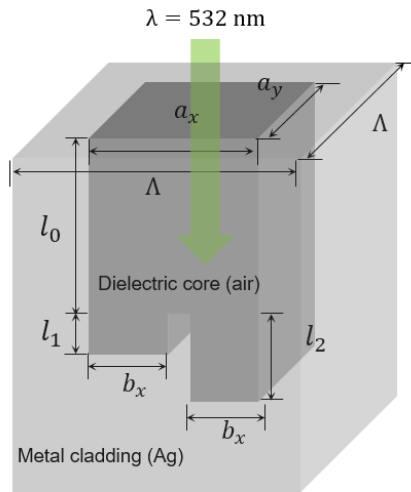


Figure 3.20 Illustration of cavity formed by square aperture waveguide with two asymmetric slit apertures at its end. Structural parameters are also found. The target wavelength is 532 nm (green).

Figure 3.21 shows the numerical result of reflectance r against continuous structural parameters l_1 and l_2 at $\lambda = 532$ nm. Nearby the perfect absorbing condition at $l_1 = 330$ nm and $l_2 = 742$ nm, arbitrary complex valued reflectance can be obtained by changing the structural parameters gradually. Full modulation width of CPA-based cavity is defined as the maximum reflectance such that its contour can wind the CPA condition. This definition gives r_0 that is introduced at the beginning of Sec. 3.2.1. For the structure at the CPA condition $(l_1, l_2) = (330$ nm, 742 nm), the full modulation width is calculated as 10%.

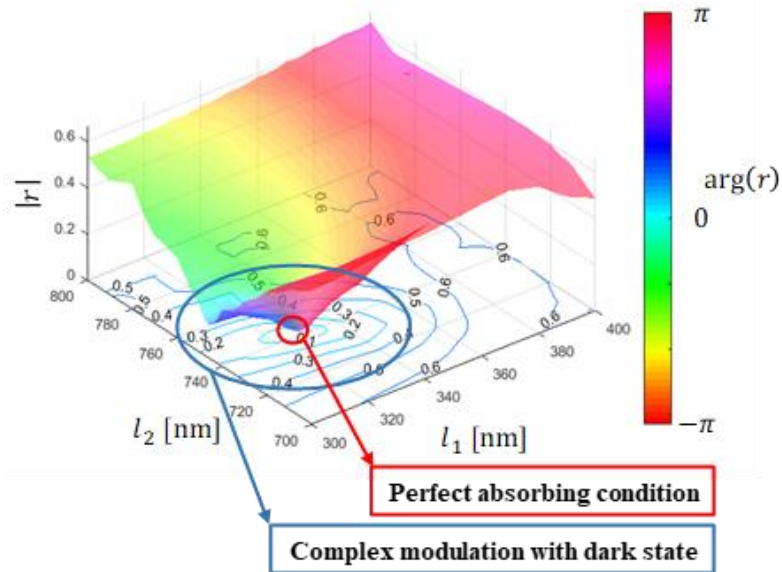


Figure 3.21 Complex amplitude map of reflection coefficient of the cavity with respect to l_1 and l_2 .

Other sets of l_1 and l_2 give CPA condition because the length of slit apertures gives phase delay without much decay. The CPA condition with the smallest slit apertures is found at $(l_1, l_2) = (38 \text{ nm}, 78 \text{ nm})$. The full modulation width is calculated as 20%, which is higher than the previous case. It is because loss in slit apertures is lowered, and consequently sharper resonance occurs nearby the CPA condition.

By proposing alternative design of complex amplitude reflection coefficient, the structure is more fabricable than the structure in Sec. 3.2.2.

Finally, it should be noted that two independent parameters give the desired

simultaneous control of phase and amplitude at will nearby CPA condition. That is, a complex coefficient r nearby the $r(p=p_0)=0$ for p is a complex number to represent two-dimensional continuous real-valued parameters p_1 and p_2 . In other words, $p = p_1 + jp_2$. Taylor series of the complex coefficient r nearby p is given as

$$r(p) = r(p_0) + a_{1,1}(p - p_0) + a_{1,2}\overline{(p - p_0)} + O((p - p_0)^2). \quad (3.9)$$

Then, except the case that CPA condition $r=0$ does not break along a trajectory passing through p_0 , the winding of the CPA condition gives full phase modulation,

$$\lim_{s \rightarrow 0} \oint_{p=p_0+s \exp(i\theta)} \frac{1}{i} \frac{d}{dp} \left(\ln \left[\frac{r(p)}{|r(p)|} \right] \right) dp = \pm 2\pi. \quad (3.10)$$

The exceptional case is equivalently stated that there is a line of CPA condition of the considered two-dimensional parameter space. That is, there is a change that cannot influence the complex valued coefficient, which means the parameter space is ill-defined.

3.3 Design of complex amplitude transmission coefficient of light in 3D metal-clad waveguide

In the previous section, a plasmonic metal-clad waveguide acts as a filter to prevent transmission of higher order waveguide modes. Moreover, the edge of the waveguide radiates light into free space with magnetic dipole-like radiation pattern. CPA condition is used to accomplish complex amplitude modulation with completely dark state, and complex amplitude modulation naturally occurs nearby the CPA condition in two-dimensional parametric space.

The design of complex amplitude transmission coefficient of light is briefly discussed in this section. Although CPA based cavities have no other scattering channels, transmission-type structure does not require perfect absorbing condition to nullify the transmission coefficient. Bearing this observation in mind, a transmission type structure with regularized radiation pattern is proposed in the following.

Table 3.1 illustrates that gap between dipoles gives irregular radiation pattern because multipole component is dependent on distance between elements. Regularization occurs for the case of dipoles with no gap as found in the second column. The physical realization of magnetic dipoles is given by the nano-slits on a metal surface as seen in the lower row of Table 3.1. Distance between nano-slits gives irregular radiation pattern, and not surprisingly, introducing a short three-dimensional metal-clad waveguide so that scattering field is directly coupled to the

plasmonic waveguide modes. The edge of the waveguide radiates light with magnetic dipole-like radiation pattern. It is noted that length of the waveguide is a quarter of the wavelength $t_w = \lambda / 4 = 250 \text{ nm}$, and it is sufficient to regularize the overall radiation pattern of each unit cell.

Table 3.1 Gap between elements makes radiation pattern irregular, and plasmonic waveguide regularizes radiation pattern.

| | Not regularized: gap between elements | Regularized: no gap between elements |
|------------------|---------------------------------------|--------------------------------------|
| Electric dipoles | | |
| Nano-slits | | |

It is well known that rotation of nano-slit gives geometric phase that is two times of the rotation angle if the structure is illuminated by circularly polarized plane wave [81]. As illustrated in the lower row of Table 3.1, if two nano-slits are rotated by θ_1 and θ_2 , the cross-polarization transmission coefficients of the individual slits are given as $a \exp(-j2\theta_1)$ and $b \exp(-j2\theta_2)$, respectively. If the

shapes of the two nano-slits are identical, location of nano-slits is symmetric in the waveguide, and mutual interaction is negligible, overall cross-polarization transmission coefficient is given as

$$t_{\text{cross}} = a \exp(-j2\theta_1) + a \exp(-j2\theta_2) = 2a \cos(\theta_1 - \theta_2) \exp(-j(\theta_1 + \theta_2)), \quad (3.11)$$

where the polarization basis is the set of two circular polarizations $\{+\sigma, -\sigma\}$.

Tuning the difference of the rotation angles gives amplitude modulation, and changing the average of the rotation angles gives phase modulation. Thus, this configuration will have complex amplitude cross-polarization transmission coefficient with intuitive modulation scheme. Moreover, radiation patterns of the proposed structure array are fully regularized so that they have magnetic dipole-like radiation patterns.

To prove complex modulation capability of the cross-polarization transmission coefficient with regularized radiation patterns of the proposed design, I investigate a metasurface of which unit cell consists of four H-shaped nano-apertures as shown in Fig. 3.22(a). The metasurface can be regularized by introducing metal-clad short waveguides onto unit cells, its regularized version is illustrated in Fig. 3.22(b). Structural parameters of the proposed structures are illustrated in Figs. 3.22(c) and (d). The parameters $h=150$ nm, $g_x=70$ nm and $g_y=40$ nm are optimized to achieve high coupling efficiency. The others are $t_s=50$ nm, $t_w=250$ nm, $\Lambda=640$ nm, $\Lambda_{\text{sub}}=270$ nm, and $w_x=w_y=100$ nm. The wavelength is $\lambda=980$ nm. The metallic substrate is assumed to be made of

gold.

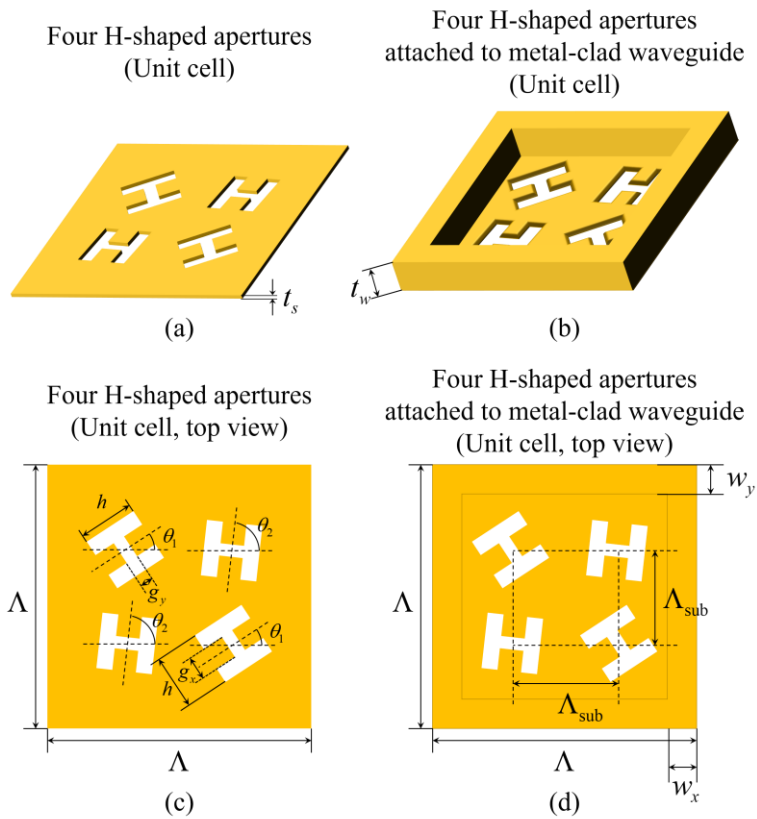


Figure 3.22 Schematics of (a), (c) a supercell metasurface of which unit cell comprised of four H-shaped apertures, and (b), (d) regularized version of the supercell metasurface depicted in (a). Two orthogonal plasmonic modes in a short metal-clad plasmonic waveguide of unit cell have equal coupling efficiency of four apertures.

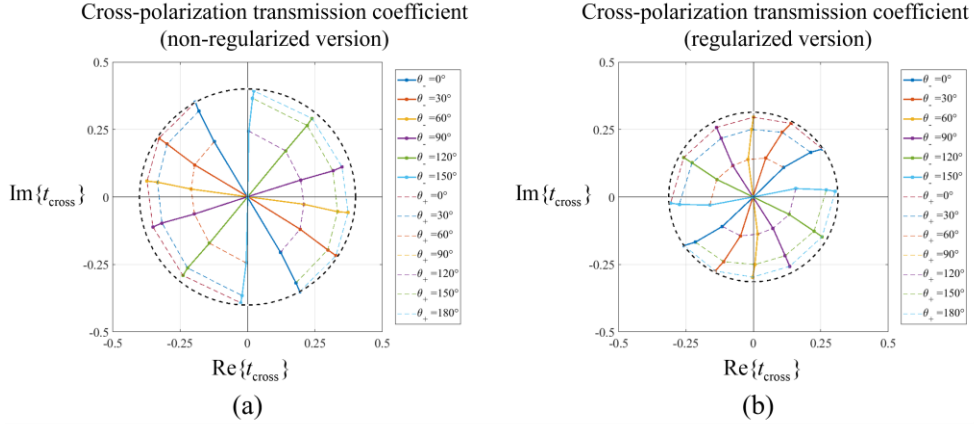


Figure 3.23 Cross-polarization transmission coefficient with respect to various set of rotation angles θ_1 and θ_2 . For convenience, two parameters θ_+ and θ_- are defined as $\theta_+ = \theta_1 + \theta_2$, $\theta_- = \theta_1 - \theta_2$. Periodic condition is used with normal incidence of circular polarized light.

Figure 3.23 shows that complex modulation is accomplished by changing θ_1 and θ_2 for both cases. This numerical results are calculated under assumption of periodic boundary condition and normal incidence of circular polarized plane wave. It means that introducing the metal-clad waveguide to regularize radiation patterns of unit cells does not harm the original complex modulation capability of cross-polarization transmission coefficient. Note that modulation efficiency of the regularized metasurface is lower than that of the non-regularized metasurface.

The proposed structure is fabricable if multi-level lithography and conformal

metal-deposition, and introducing substrate might enhance the overall efficiency by suppressing backscattering after optimization. It is expected that this type of metasurfaces can be used to develop supercell-based metasurfaces with regularized radiation patterns of unit cells.

3.4 Conclusion

In this chapter, various structures of complex amplitude reflection and transmission coefficient are provided. I firstly gave an introductory section to describe how to achieve CPA condition and how to engineer it. Inspired by the engineering capability of magnetic dipole of the parallel metal strips in 2D MIM plasmonic waveguide, reflective cavity structure composed of nanostructures embedded in plasmonic waveguides with a metallic end can be served as achieving complex amplitude reflection coefficient. Moreover, alternative design is proposed: asymmetric slit apertures attached at the end of the 3D metal-clad plasmonic waveguide gives interferometric complex amplitude modulation of light. Mathematical formulation on the parametric change of reflection coefficient infers that complex amplitude with full phase modulation capability and completely dark state naturally occurs. The last section is devoted to design cross-polarized transmission coefficient by placing multiple scatterers onto the entrance of a plasmonic waveguide structure. All the proposed structures have magnetic dipole-like radiation patterns due to the edge of the waveguide. Therefore, the proposed structures are compatible with regularization process, and consequently, can be exploited to realize regularized meta-atoms equipped with complex amplitude modulation and polarization at will. Finally, it is remarked that the size of the reflection-type complex modulator proposed in Sec. 3.2.3 is comparable to the cubic of wavelength (λ^3). Future research on compact active mechanisms is highly demanded to develop compact spatial light modulator with wide angle operation.

Finally, Section 3.3 investigate a design of non-CPA based complex modulating meta-atoms with regularized radiation patterns. By introducing a short waveguide attached to each unit cell, complex amplitude modulation capability is not broken and the overall radiation pattern of each unit cell is successfully regularized. Four H-shaped apertures are aggregated to form a unit cell as an example of supercell metasurfaces, and its regularized version is made by introducing a short metal-clad waveguide onto the four nano-apertures to regularize overall radiation pattern. The Numerical results show that the complex amplitude modulation capability is maintained after regularization.

Chapter 4 Low noise generation of plasmonic field based on regularized Huygens' sources

4.1 Introduction

In this chapter, I propose a metal-clad plasmonic waveguide array as a platform of regularized Huygens' plasmonic wave field synthesis. By adopting regularized Huygens' sources, rigorous generation of plasmonic field is possible as discussed in chapter 2. The ultimate goal of generating arbitrary plasmonic field is the design of meta-slit with full modulation capability of both amplitude and phase in an intuitive manner. Section 4.2 explains how to apply complex amplitude to the Huygens' sources by using tilted input slit of each waveguide. Using metal-clad waveguide array, a diffraction-limited spot with minimal sidelobes is generated. The perfect synthesis of arbitrary plasmonic field is then derived by superposing the sets of Huygens' sources, and each set corresponds to the Huygens' sources that generates diffraction-limited spot of the sampled complex amplitude at each sampling position. As a proof-of-concept, two cases are presented: a plasmonic focal spot with given numerical aperture (NA) and a truncated plasmonic Airy beam are numerically analyzed. In the last section, experimental suggestion is addressed.

4.2 Tilted slit coupled to metal-clad waveguide as regularized Huygens' plasmonic source

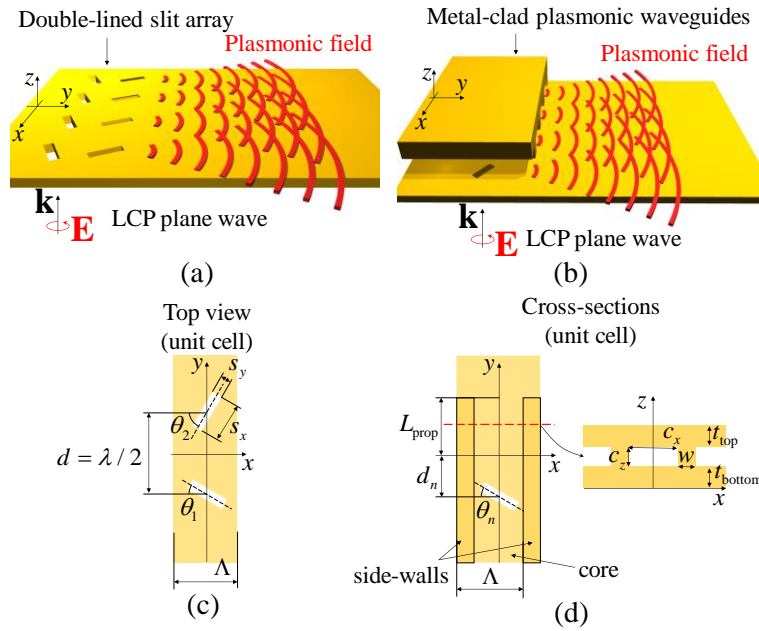


Figure 4.1 (a) and (c): Schematics of a conventional double-lined slit array (b) and (d): Schematics of the proposed structure, regularizing each unit cell of the shifted slit array. Both cases assume the incident light left-circularly polarized plane wave along $+z$ -axis. Dimensions of the metal-clad waveguide are given as $c_x = 100$ nm, $c_z = 390$ nm, $w = 100$ nm, $L_{\text{prop}} = 2$ μm , and $t_{\text{top}} = t_{\text{bottom}} = 80$ nm. Size of slits are $s_x = 300$ nm and $s_y = 80$ nm.

Two-dimensional (2D) plasmonic field synthesis is much simpler than 3D cases because only the TM polarization 2D scalar field describes all the information of plasmonic field distribution. Moreover, as in Sec. 2.2.1, plasmonic radiation field from the unit magnetic dipole moment $\vec{m}_{\theta_0} = \delta(\vec{\rho}) \cdot (\cos \theta_0 \hat{x} + \sin \theta_0 \hat{y})$ is given as

$$G_{\vec{m}_{\theta_0}} = (k_0 / 4i) H_0^{(2)}(k_0 \rho) \cos(\theta - \theta_0), \quad (4.1)$$

where $H_0^{(2)}(x)$ is a Hankel function of the second kind. The Fourier transform of the radiation profile is given as

$$\mathcal{F}_x \{ G_{\vec{m}_{\theta_0}} \} \Big|_{y=0} = \tilde{G}_{\vec{m}_{\theta_0}} = \eta U_{k_0}(k_x), \quad (4.2)$$

where $U_{k_0}(k_x)$ is an indicator function of transverse wavenumber having the value 1 for $|k_x| \leq k_0$ and the value 0 for otherwise. In this case, sampling the target field using the x -polarized magnetic dipoles can perfectly generate any plasmonic field as discussed in Sec. 2.4. For example, a slit parallel to x -axis can serve as the magnetic dipole source of plasmonic field, that is, $G_{\text{ideal,2D}} = G_{\vec{m}_{\theta_0}}$.

Researchers have suggested many methods for plasmonic field synthesis to date [116-120, 123], and I select the double-lined slit array as the representative method [118-120] and illustrate its structure in Figs. 4.1(a) and (c). Its mechanism relies mainly on Huygens' principle through equidistant sampling of the target field. This type of structure can generate an arbitrary plasmonic wavefront because the geometric phase induced by the rotation angles of slits (θ_1, θ_2) together with the

superposition of scatterers provides complex amplitude modulation.

However, as discussed in Sec. 2.4, noise is non-negligible, because the two slits in each unit cell are distant from each other, as seen in Fig. 4.1(c). Slits generate plasmonic field independently because each slit is distant from neighbor slit and the scattering is not strong enough to produce high-order scattering terms. For the perfect synthesis of a plasmonic field, the regularization of the single slit, of which rotation angle is θ_n , in each cell is done by introducing a metal-clad plasmonic waveguide, as depicted in Figs. 4.1(b) and (d). The essential element in the fabrication is the side-walls and supporting upper metal plate. Since the core of the waveguide can be replaced into dielectric medium, a metal deposition after milling of dielectric film on lower metal film can form sidewalls and upper-metal film, simultaneously.

The working principle of the proposed structure can be explained as follows. The metal cladding isolates each unit cell from its neighbors. Its size is small and anisotropic enough so that only one fundamental mode can propagate through the waveguide. The electric field of the propagating mode is mainly z -polarized, and the magnetic field is mainly x -polarized. Therefore, for incidence of left-circular polarized light as in Fig. 4.1(b), the relative coupling coefficient is represented by $c_n = \cos\theta_n \exp(-i\theta_n)$. Note that the circular polarization of the incident wave additionally induces geometric phase. The position of each slit is y -shifted as much as d_n , then additional phase $\exp(-i2\pi d_n / \lambda_{\text{eff}})$ is introduced, where λ_{eff} is effective wavelength of the fundamental mode of the metal-clad waveguide. In the

final stage, the radiation from the waveguide to the half-infinite metal plane is also approximated using the magnetic dipole radiation $G_{\text{reg}} \approx G_{\bar{m}_0}$, the waveguide supports the only propagating mode with localized and mainly x -polarized magnetic field.

Verification of this is presented in Figs. 4.2(b) and (d). The complex amplitude of the radiation for a unit cell is $a_n = \xi c_n = \xi \exp(-i\theta_n - i2\pi d_n / \lambda_{\text{eff}}) \cdot \cos\theta_n$, where ξ is a proportional constant. The overall radiation pattern for a unit cell of the proposed structure follows $a_n G_{\text{reg}} \approx a_n G_{\bar{m}_0} \approx \xi c_n G_{\text{ideal,2D}}$, thus complex modulation and regularization are simultaneously accomplished by the proposed structure.

To the contrary, in Figs. 4.2(a) and (c), the radiation pattern of a unit cell of the conventional double-lined slit array is $E_{z,\text{dls}} \approx [G_{\bar{m}_{\theta_1}} \exp(-i\theta_1) + G_{\bar{m}_{\theta_2}} \cdot \exp(-i\pi \cos\theta - i\theta_2)]$. The double-lined slit array works as desired under paraxial launching, but the radiation profile of a unit cell is irregular and varies in parameter space (θ_1, θ_2) .

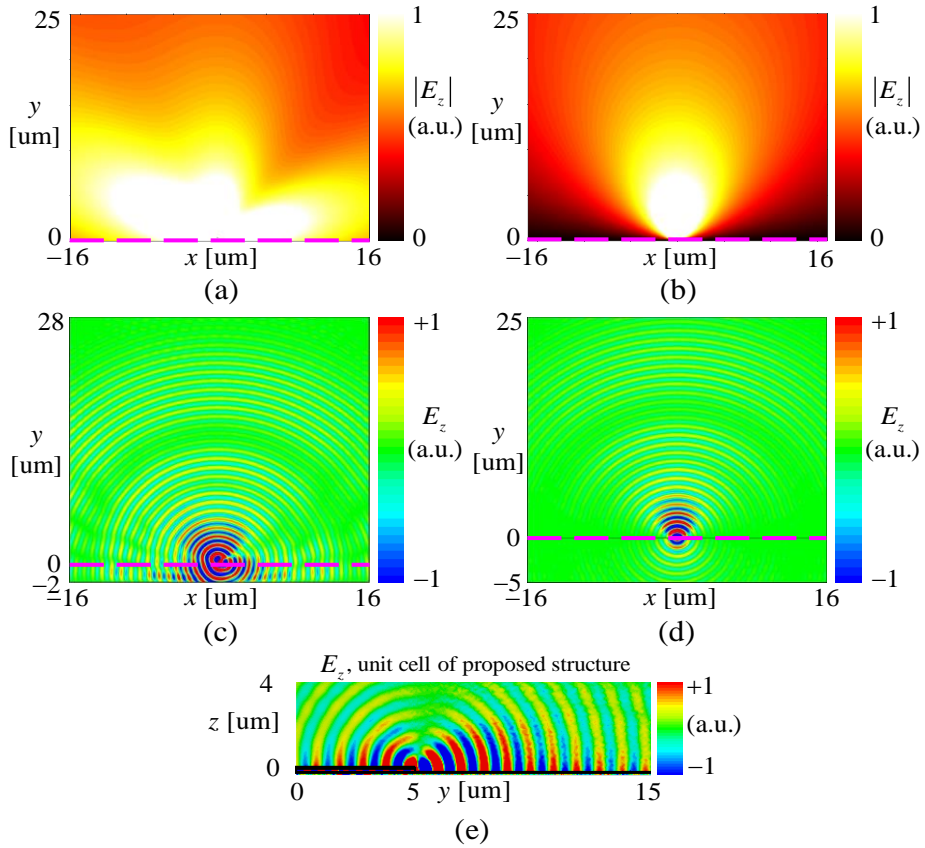


Figure 4.2 (a) and (c): Radiation field distributions of a unit cell of double-lined slit array for $\theta_1 = -30^\circ$, $\theta_2 = 60^\circ$. (b) and (d): Radiation field distributions in the proposed structure for $\theta = 0^\circ$, $d = 0$ nm. The purple dashed lines indicate $y = 0$ μm . (e) The waveguide mode efficiently produces a plasmonic field.

3D full-field simulations were carried out using CST studio SUITE. Analytical modeling of plasmonic field generated by double-lined slit arrays and ideal point source arrays was performed using MATLAB [118-120]. The wavelengths were fixed at 980 nm and the metal was assumed to be gold. All dimensions are illustrated in Figs. 4.1(c) and (d). Sampling period satisfies the Nyquist sampling rate, $\Lambda \leq \lambda / 2$. The structural parameters are chosen for obtaining cell isolation and single propagation mode ($c_x < L / 2$, $c_y \ll \lambda$). Note that if multimode excitation were involved, the modulation could not be expressed in any simple form. In Fig. 4.2, the effect of the regularization process is analyzed. For the case of the double slits parameterized by $(\theta_1, \theta_2) = (-30^\circ, 60^\circ)$, the analytical radiation pattern of the two slits is presented in Fig. 4.2(a). In Fig. 4.2(c), 3D full-field simulation result confirms the analytical model. On the other hand, the proposed structure successfully regularizes the radiation field distribution as shown in Figs. 4.2(b) and (d). Figure 4.2(e) shows that the metal-clad waveguide launches plasmonic field to the half-infinite metal plane.

4.3 Rigorous generation of plasmonic field via metal-clad waveguide array

As shown in the previous section, unit-cell or meta-atom of the metal-clad waveguide array is capable of complex modulation and regularization of radiation pattern. In this section, I utilize the proposed metal-clad waveguide array as the platform of generating arbitrary plasmonic field. The performance of the proposed structure is presented by comparing that of double-lined slit array. It is noted that the sampling rate is fixed at the inverse of half of the wavelength, and the number of sample points is 61 in this section.

4.3.1 Plasmonic focal spot

In this subsection, diffraction-limited plasmonic focusing is presented via the proposed metal-clad waveguide array and the double-lined slit array. Figure 4.3 depicts a focused plasmonic field to demonstrate the effect of regularization on the generation of a plasmonic field. Maximal intensity at the focal point can be generated by backpropagation:

$$a_n = \overline{G_{\tilde{m}_0}}(\theta) = \overline{H_0^{(2)}(k_{\text{SPP}}\sqrt{f^2 + x^2})} \cdot (f / \sqrt{f^2 + x^2}), \quad (4.3)$$

where f is the distance between the reconstruction line and the focal line, and k_{SPP} refers to the complex wavenumber of SPPs. The overbar notation indicates complex conjugate operation. On the other hand, the sampling profile also implies

that the generated field should be $\text{sinc}(NA \cdot k_0 y / \pi)$, which is, as expected, the Fourier transform of the rectangular function. Analytical dipole modelling perfectly illustrates this situation in Fig. 4.3(c).

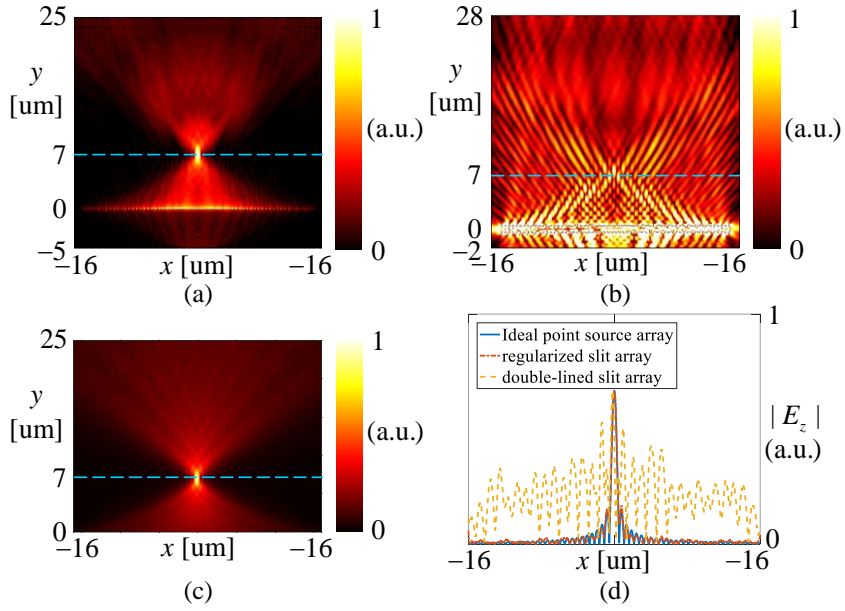


Figure 4.3 Numerical results of SPP focusing at $y = 7 \text{ um}$ with (a) the proposed structure, and (b) the double-lined slit array. (c) Analytical dipole modelling produces a plasmonic field with sinc function profile. (d) The amplitudes of the simulated fields at the focal line are compared. Each blue dashed line on (a), (b) and (c) depicts the corresponding focal line.

The profile expressed in Eq. 4.3 is used to achieve diffraction-limited focusing with minimal noise as in Fig. 4.3(a). The estimated signal-to-noise ratio (SNR) is about 54. The conventional double-lined slit array focuses near the desired position, but it is slightly shifted and background noise also appears with a low SNR of approximately 0.14 as in Fig. 4.3(b). Regularized dipole radiation is realized by the proposed structure, and 3D full-field simulation confirms that tight and bell-shaped focusing is produced via the regularization process as seen in Fig. 4.3(d). It is shown that very accurate plasmonic field distribution is achieved in this case.

4.3.2 Plasmonic Airy beam

In this subsection, generation of truncated plasmonic Airy beam is presented for proving the capability of arbitrary plasmonic wavefront of the proposed metal-clad waveguide array. Airy beam has non-diffracting property, which has attracted much attention [144]. Plasmonic Airy beam is one-dimensional non-diffracting plasmonic wavefront, and many researchers have investigated on the generation of plasmonic Airy beam [145]. Here, truncated version of plasmonic Airy beam is generated via the proposed structure as well as the conventional double-lined slit array.

Figure 4.4 displays another example of Airy plasmonic field generation via meta-slit and its regularized version:

$$a_n = \text{Airy}((x - x_0) / a), \quad (4.4)$$

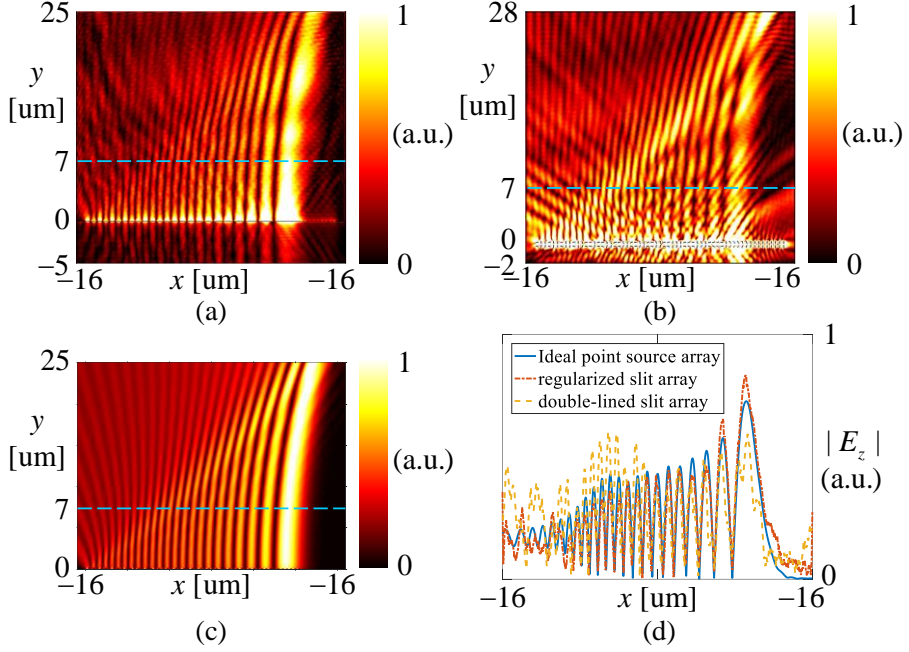


Figure 4.4 Plasmonic Airy beams constructed by (a) the proposed structure and (b) the double-lined slit array. (c) Analytical dipole modelling produces a plasmonic Airy beam. (d) The amplitudes of the simulated fields at $y = 7 \mu\text{m}$ are compared. Each blue dashed line on (a), (b) and (c) depicts $y = 7 \mu\text{m}$ line.

where the parameters are fixed at $x_0 = 10 \mu\text{m}$, $a = 1.1\lambda$. This distribution of dipole amplitude should generate non-diffracting plasmonic Airy beam as in Fig. 4.4(c). As seen in Fig. 4.4(b), the conventional method distorts the main lobe of the synthesized field distribution severely by background noise. In contrast, the

proposed structure generates a noise-reduced non-diffracting profile for the Airy plasmonic beam as in Fig. 4.4(a). The finite length of the double-lined slit array blurs outer side-lobes. The amplitudes of the simulated fields at the same reconstruction plane $y = 7 \text{ um}$ are compared in Fig. 4.4(d). It is shown that the distortion near the main lobe is greatly reduced by the regularization process.

4.4 Experimental suggestion and demonstration

4.4.1 Experimental suggestion of fabricating a variant of metal-clad waveguide array

The proposed metal-clad waveguide array is proved to be a platform of complex amplitude modulated Huygens' sources with near-ideal radiation patterns in the previous sections, however, fabrication of it and its variants generally requires a series of lithography and deposition on a selective area. For example, one of feasible fabrication techniques would be photolithography to form low refractive index polymer cores of waveguides and e-beam evaporating deposition of metal on a selective area to make walls and ceiling of waveguides. Input slits can be formed by focused ion beam (FIB) milling process. High refractive index for core material of waveguides is not preferred because width of waveguides is so narrow that size of input slits is not sufficient to guarantee coupling efficiency for near-field detection by near-field scanning optical microscope (NSOM).

Several modifications on design of regularized meta-slits can be made to reduce the number of fabrication techniques. In this section, I suggest a feasible fabrication process as depicted in Fig. 4.5. It utilizes FIB milling and metal deposition to accomplish all the features: complex amplitude modulation is acquired by changing width and shift of each input slit, and regularization is realized by milling identical output slit. In practice, however, inefficient coupling efficiency due to short length of slits and waveguiding loss severely degrades the

performance of the proposed structure. In addition, Si_3N_4 dielectric film has high refractive index $n_{\text{Si}_3\text{N}_4} = 2.0146$ at wavelength 980 nm, so that single propagating mode operation is not guaranteed, only numerical simulation confirms the reliability of complex amplitude modulation. It was failed to demonstrate generation of plasmonic wavefront with low noise via the proposed structures, because the overall efficiency of the proposed structure is too low to detect plasmonic field by NSOM.

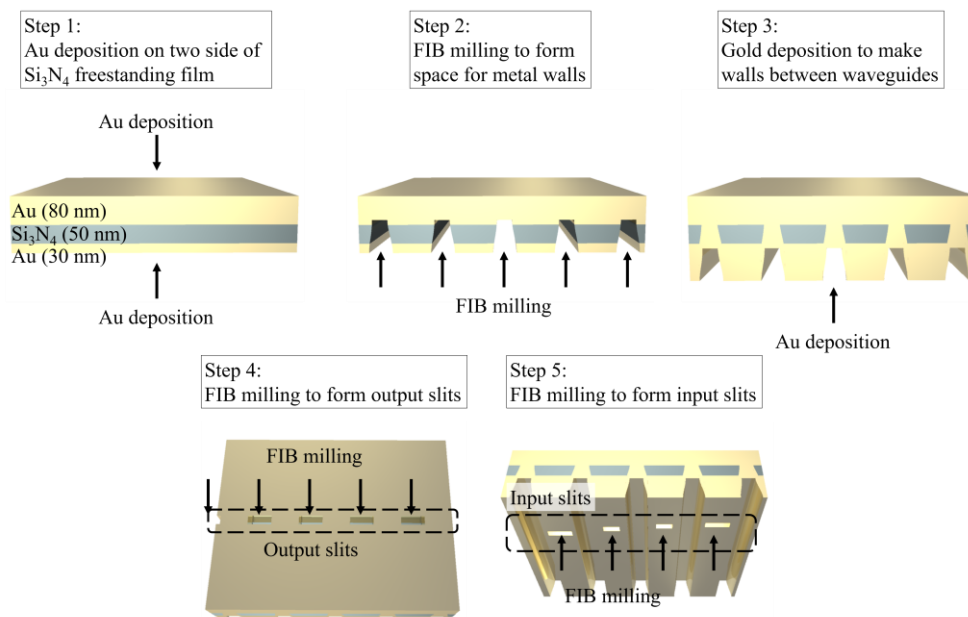


Figure 4.5 Illustration of the proposed fabrication process for a variant of the metal-clad waveguide array introduced in Sec. 4.2.

4.4.2 Comparative study on meta-slits

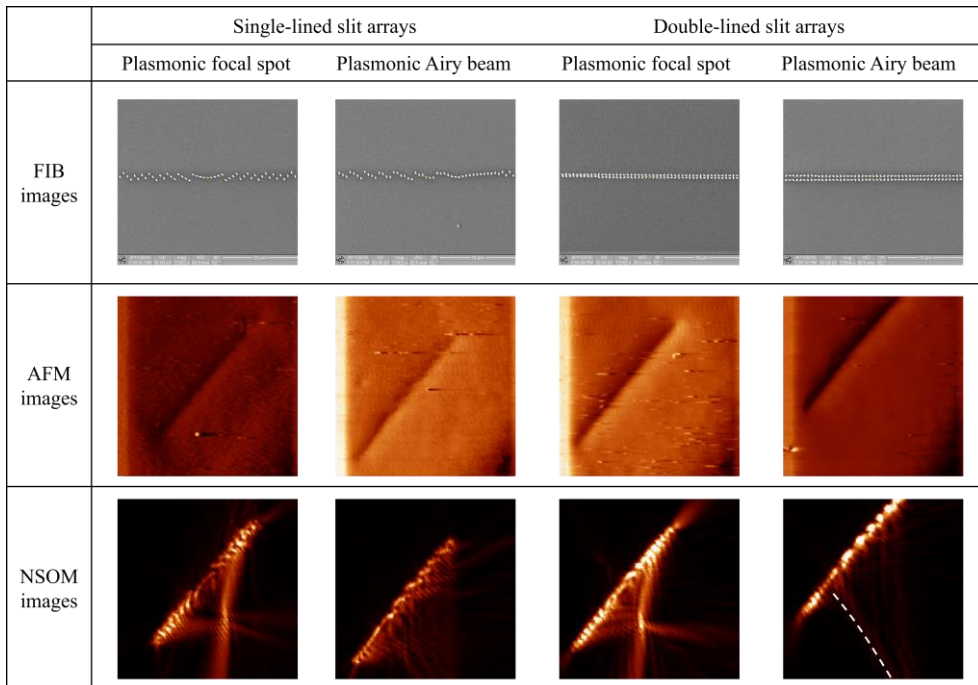


Figure 4.6 Demonstration of the performance of the two meta-slits: single-lined slit arrays and double-lined slit arrays. FIB images (first row), AFM images (second row), and NSOM images (third row) are provided. Single-lined slit arrays for generating plasmonic focal spot of $z_0 = 5 \text{ um}$ (first column) and plasmonic Airy beam (second column). Double-lined slit arrays for generating plasmonic focal spot of $z_0 = 5 \text{ um}$ (third column) and plasmonic Airy beam (fourth column).

The double-lined slit arrays are one of the most efficient and low-noise platforms of generating plasmonic wavefronts. Spatially broadband signals generated by the double-lined slit arrays suffer from interference of inherent caustic rays for $NA > 0.5$, however, performance of other meta-slits is worse than that of double-lined slit arrays.

Figure 4.6 shows comparative study on the performance of the two meta-slits: single-lined slit arrays and double-lined slit arrays. A single-lined slit array is comprised of slit arrays along a curve; Rotation angle of slit gives geometric phase when circularly polarized plane wave is incident on the meta-slit. Longitudinal shift of slit induces phase delay. Thus, complex amplitude modulation is accomplished by these two independent parameters. However, it can be proved that the single-lined slit arrays have more irregular radiation patterns than the double-lined slit arrays. The plasmonic focal spot and plasmonic Airy beam used in Fig. 4.6 have the same parameters as found in Figs. 4.3 and 4.4. The experimental results confirm that the double-lined slit arrays formed a clear focal spot with a considerable amount of sidelobes for the case of plasmonic focal spot, whereas the single-lined slit array was failed to make not a focal spot but interference pattern for the same case. In addition, the plasmonic Airy beam generated by the double-lined slit array barely shows a main lobe accompanied by the characteristic bending (depicted by a white dotted line). Caustic rays interfering with the reconstructed plasmonic Airy beam are also observed. It is noted that the generated wavefront of the single-lined slit array was failed to show the non-diffracting feature.

4.5 Conclusion

In this chapter, a scheme for generating arbitrary plasmonic field is proposed. The regularization of meta-atoms is realized by adopting metal-clad waveguide on each cell consisting of tilted slit. The proposed structure has complex amplitude modulation capability with regularized near-ideal profile of radiation patterns, direct sampling of plasmonic wavefront just gives the correct wavefront generated by normal incidence of circularly polarized plane wave on the metal-clad waveguide array. Backpropagation method enables to construct diffraction-limited plasmonic focusing with extremely compressed sidelobes. It is shown that the conventional double-lined slit array as a representative of meta-slits cannot generate the target wavefront with low-noise if considered wavefront has spatially broad bandwidth. Experimental suggestion is made, but overall efficiency should be improved to detect waveform with sufficient accuracy. I expect that this study has paved the way to develop active meta-slits for accurate generation of arbitrary plasmonic wavefront. In addition, it is inferred that the regularization of optical Huygens' sources might also improve the performance of generating arbitrary optical field via meta-surface. In the next chapter, this argument is examined by proposing a novel type of metasurfaces.

Chapter 5 Low noise generation of optical field based on regularized Huygens' sources

5.1 Introduction

In the previous chapter, low noise generation of plasmonic field by regularized Huygens' sources is presented, and its realization is proposed: the metal-clad waveguide array. Generation of optical field is harder than that of plasmonic field because the vector nature of optical waves. Moreover, regarding optically thin passive metasurfaces, they cannot give advancing phase with respect to the incident wave. In other words, regularized meta-atoms with complex amplitude and arbitrary polarization cannot be realized unless active materials are available.

Meanwhile, in Chapter 2, meta-atoms with high-order multipoles are difficult to control scattering amplitudes at will. Natural choices of regularized meta-atoms are only two types: electric dipole antennas or magnetic dipole apertures. I select electric dipole nano-antennas as the regularized meta-atoms without any loss of generality. I note that the similar approach is possible with magnetic dipole nano-apertures.

In this chapter, I firstly assume that meta-atoms having complex amplitude modulated electric dipole with arbitrary in-plane polarization are available. By

using the hypothetical meta-atoms, I derive a novel scheme to generate arbitrary optical wavefront by periodically arranging meta-atoms.

5.2 Electric dipole metasurfaces as regularized Huygens' optical sources

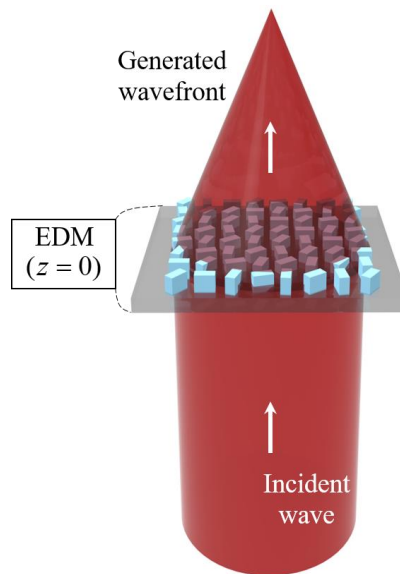


Figure 5.1 A schematic of an electric dipole metasurface (EDM) with subwavelength-sized dielectric rods on a flat substrate.

In this section, an electric dipole metasurface (EDM) is defined as depicted in Fig. 5.1. It can be formed from the arrangement of subwavelength-size dielectric or metallic rods on a flat substrate. Assuming that the dielectric meta-atoms are not so close to each other that their mutual interaction is negligible [70, 79-83], the total

scattering field for an EDM is considered to be the linear superposition of the scattering fields of the individual meta-atoms in free space. As I mentioned in the previous section, it is assumed that an EDM that has meta-atoms with arbitrary in-plane electric dipole moments can generate an arbitrary vector field at a specified output plane.

5.3 Rigorous generation of optical field via electric dipole metasurface

In the previous section, it is argued that EDM can generate arbitrary optical wavefront. In this section, I will show this by deriving in-plane dipole moment density of EDM corresponding to various optical waves. Plasmonic field synthesis is a lot easier than optical field synthesis because ideal Huygens' sources are available as presented in Chapter 4. Thus, in subsection 5.3.1, I show that a linearly polarized Airy disk is constructed as a virtual Huygens' source. Arbitrary optical wavefront is constructed by superposing EDMs corresponding to the periodically arranged virtual Huygens' sources to sample electric field of the target wavefront.

5.3.1 Linearly polarized Airy disk

In this subsection, in-plane dipole moment density of the proposed EDMs corresponding to linearly polarized Airy disks is derived. Schematically illustrated in Fig. 5.2, it is crucial to derive the in-plane vector field distribution on the metasurface plane to generate a precise linear-polarized Airy disk pattern on the specific output plane, $z = z_0$. An x -polarized Airy disk is defined as the in-plane electric field distribution in which the angular spectrum, $\vec{\mathcal{E}}_{\text{tan}}$, is designed by

$$\vec{\mathcal{E}}_{\text{tan}}(k_x, k_y) = \mathcal{F}_{xy} \{ \hat{z} \times (\vec{E}(\rho, \theta, z_0) \times \hat{z}) \} = \mathbf{1}_{k_\rho \leq \text{NA} \cdot k_0} \hat{x}, \quad (5.1)$$

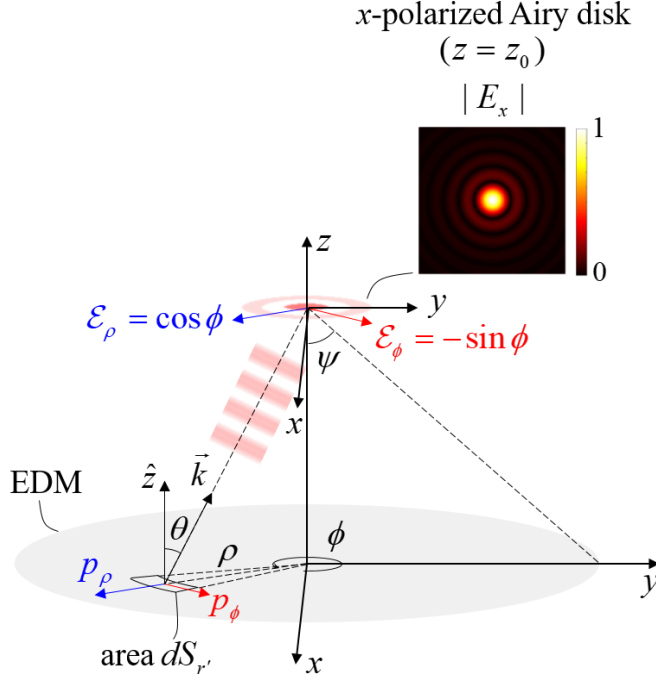


Figure 5.2 Illustration of the derivation of the electric dipole moment density of the EDM generating an x -polarized Airy disk pattern. The dipole moment densities, p_ρ and p_ϕ , in the infinitesimal area dS_r , correspond to the angular spectral components of the x -polarized Airy disk \mathcal{E}_ρ and \mathcal{E}_ϕ on the output plane, respectively.

where $\mathcal{F}_{xy}\{\cdot\}$ is the two-dimensional Fourier transform and $\mathbf{1}_{k_\rho \leq \text{NA} \cdot k_0}$ is an indicator function whose value is 1 when the tangential wavenumber $k_\rho = (k_x^2 + k_y^2)^{1/2}$ is not greater than $\text{NA} \cdot k_0$, and 0 otherwise. NA is the

numerical aperture of the Airy disk as defined by $\text{NA} = \sin\psi$, and the radius of the EDM is set accordingly to $R = z_0 \tan\psi$. It should be noted that Eq. 5.1 completely determines z -component of the electric field. The z -component of the electric field of x -polarized Airy disk causes anisotropic intensity distribution at $z = z_0$. There has been much research on anisotropic focal spots and beams with high-NA [146-149].

To generate the angular spectrum components of Eq. 5.1 on the output plane, each electric dipole moment should be placed at the specific corresponding position on the metasurface plane, as shown in Fig. 5.2. Because the field distribution of the Airy disk is localized around $(0, 0, z_0)$ and the corresponding electric dipole density varies slowly, the radiating pattern of the infinitesimal electric dipole moment, $\vec{p} = p_\rho \hat{\rho} + p_\phi \hat{\phi}$, on the EDM is the dominant contributor to the angular spectrum component, $\vec{\mathcal{E}}_{\text{tan}} = \mathcal{E}_\rho \hat{\rho} + \mathcal{E}_\phi \hat{\phi}$, of which wavevector \vec{k} should be parallel to the direction vector from the dipole to the center of the Airy disk, $\vec{r} - \vec{r}' = (-\rho \cos\phi, -\rho \sin\phi, z_0)$. The radiation pattern of dipole \vec{p} at position \vec{r}' in infinitesimal area dS_r is assumed to be in the form of Green's dyadic:

$$\begin{aligned} \vec{E} &= \vec{G} * \vec{p} = [1 + \vec{\nabla}\vec{\nabla}] \frac{e^{-ik_0|\vec{r}-\vec{r}'|}}{4\pi\epsilon_0|\vec{r}-\vec{r}'|} \cdot \vec{p} \\ &\approx \frac{e^{-ik_0|\vec{r}-\vec{r}'|}}{4\pi\epsilon_0|\vec{r}-\vec{r}'|^3} (|\vec{r}-\vec{r}'|^2 \vec{I} - (\vec{r}-\vec{r}')(\vec{r}-\vec{r}')) \vec{p}. \end{aligned} \quad (5.2)$$

Figure 5.2 illustrates that the angular spectrum component with $\vec{k} \parallel (\vec{r} - \vec{r}')$, decomposes into TM and TE components, \mathcal{E}_ρ and \mathcal{E}_ϕ , respectively. For the x -polarized Airy disk, $\mathcal{E}_\rho = \cos\phi$ and $\mathcal{E}_\phi = -\sin\phi$. It should be noted that \mathcal{E}_ρ is accompanied by the z -component of the Fourier component $-k_\rho \mathcal{E}_\rho / k_z$, while \mathcal{E}_ϕ is not. In turn, the generation of unit TM component needs $k_0 / k_z = 1 / \cos\theta$ times more power than that of the unit TE component, and the in-plane components of the electric field completely determine the perpendicular component of the electric field for the unit Airy disk field. Accordingly, the dipole field on the metasurface plane decomposes into TM and TE components, p_ρ and p_ϕ , respectively, as in Fig. 5.2. Starting with Eq. 5.2, the electric field distribution generated by the decomposed dipole components can be represented by

$$\begin{bmatrix} E_{\text{TM}}(\vec{r}) \\ E_{\text{TE}}(\vec{r}) \end{bmatrix} = \frac{1}{\epsilon_0} \frac{e^{-ik_0|\vec{r}-\vec{r}'|}}{4\pi|\vec{r}-\vec{r}'|} \begin{bmatrix} z/|\vec{r}-\vec{r}'| & 0 \\ 0 & 1 \end{bmatrix} \begin{bmatrix} p_\rho \\ p_\phi \end{bmatrix}. \quad (5.3)$$

For fixed propagating direction $\vec{k} \parallel (\vec{r} - \vec{r}')$, the TM component of the electric dipole moment, p_ρ , radiates only the TM component with the inclination factor $z/|\vec{r} - \vec{r}'| = \cos\theta$, while p_ϕ exclusively radiates the TE component. The infinitesimal area $dS_{r'}$ corresponds to the infinitesimal area in the transverse k -space dS_k in the form of $|dS_{r'} / dS_k| = (\rho d\rho d\phi) / (k_\rho dk_\rho d\phi) = |\vec{r} - \vec{r}'|^4 / z^2 = |\vec{r} - \vec{r}'|^2 / \cos^2\theta$. At the focal spot of the x -polarized Airy disk $\vec{r} = \vec{r}_0 = z_0 \hat{z}$, the

electric dipole $\vec{p} = p_\rho \hat{\rho} + p_\phi \hat{\phi}$ at $\vec{r}' = \rho(\cos \phi \hat{x} + \sin \phi \hat{y})$ contributes to the Fourier components $\mathcal{E}_\rho(\vec{k})$ and $\mathcal{E}_\phi(\vec{k})$ as follows:

$$\begin{bmatrix} \mathcal{E}_\rho(\vec{k}) \\ \mathcal{E}_\phi(\vec{k}) \end{bmatrix} \propto \left| \frac{dS_r}{dS_k} \right| \begin{bmatrix} E_{\text{TM}}(\vec{r}_0) \cos \theta \\ E_{\text{TE}}(\vec{r}_0) \end{bmatrix} = \frac{|\vec{r}_0 - \vec{r}'| e^{-ik_0|\vec{r} - \vec{r}'|}}{\epsilon_0 4\pi} \begin{bmatrix} p_\rho \\ p_\phi / \cos^2 \theta \end{bmatrix}. \quad (5.4)$$

Specifically, the distribution of the electric dipoles for the generation of the x -polarized Airy disk described in Eq. 5.1 is given as:

$$\begin{bmatrix} p_\rho \\ p_\phi \end{bmatrix} \propto \frac{e^{ik_0|\vec{r}_0 - \vec{r}'|}}{|\vec{r}_0 - \vec{r}'|} \begin{bmatrix} \mathcal{E}_\rho \\ \mathcal{E}_\phi \cos^2 \theta \end{bmatrix} = \frac{e^{ik_0|\vec{r}_0 - \vec{r}'|}}{|\vec{r}_0 - \vec{r}'|} \begin{bmatrix} \cos \phi \\ -\cos^2 \theta \sin \phi \end{bmatrix} \mathbf{1}_{\theta \leq \psi}. \quad (5.5)$$

p_x and p_y are derived by applying position-dependent rotation:

$$\begin{bmatrix} p_x \\ p_y \end{bmatrix} = \begin{bmatrix} \cos \phi & -\sin \phi \\ \sin \phi & \cos \phi \end{bmatrix} \begin{bmatrix} p_\rho \\ p_\phi \end{bmatrix} \propto \frac{e^{ik_0|\vec{r}_0 - \vec{r}'|}}{|\vec{r}_0 - \vec{r}'|} \begin{bmatrix} \cos^2 \phi + \cos^2 \theta \sin^2 \phi \\ \sin^2 \theta \sin \phi \cos \phi \end{bmatrix} \mathbf{1}_{\theta \leq \psi}. \quad (5.6)$$

Finally, the constructed field \vec{E}_{gen} , via the distribution of in-plane electric dipoles in Eq. 5.6, can be calculated as follows:

$$\vec{E}_{\text{gen}}(\vec{r}) \propto \iint_{x'^2+y'^2 \leq z_0^2 \tan^2 \psi} dx' dy' \frac{e^{-ik_0|\vec{r}-\vec{r}'|}}{|\vec{r}-\vec{r}'|^3} \frac{e^{ik_0|\vec{r}_0-\vec{r}'|}}{|\vec{r}_0-\vec{r}'|} \times \begin{bmatrix} (\vec{r}-\vec{r}')^2 - (x-x')^2 & -(y-y')(x-x') & -(z-z')(x-x') \\ -(x-x')(y-y') & (\vec{r}-\vec{r}')^2 - (y-y')^2 & -(z-z')(y-y') \\ -(x-x')(z-z') & -(y-y')(z-z') & (\vec{r}-\vec{r}')^2 - (z-z')^2 \end{bmatrix} \begin{bmatrix} \cos^2 \phi + \cos^2 \theta \sin^2 \phi \\ \sin^2 \theta \sin \phi \cos \phi \\ 0 \end{bmatrix}. \quad (5.7)$$

I argue that $\vec{E}_{\text{gen}} \cdot \hat{x} \Big|_{z=z_0} \propto J_1(\text{NA} \cdot k_0 \rho) / \rho$, that is, the x component of the generated field is the form of the Airy disk in Eq. 5.1. The decomposed dipole field \vec{p} was normalized to produce the x -polarized Airy disk on the focal plane $z = z_0$ of the form, with precise approximation,

$$E_x = \text{NA} \cdot k_0 \frac{J_1(\text{NA} \cdot k_0 \rho)}{2\pi\rho}, \quad (5.8)$$

where $J_1(x)$ is the first-order Bessel function of the first kind. This geometric correspondence is assisted by two previously established premises: (i) the x -polarized Airy disk is localized within the diffraction limited area, and (ii) the derived distribution of the electric dipoles varies slowly. In turn, this geometric ray-like treatment of EMD design is sufficient to generate an x -polarized Airy disk field on the output plane.

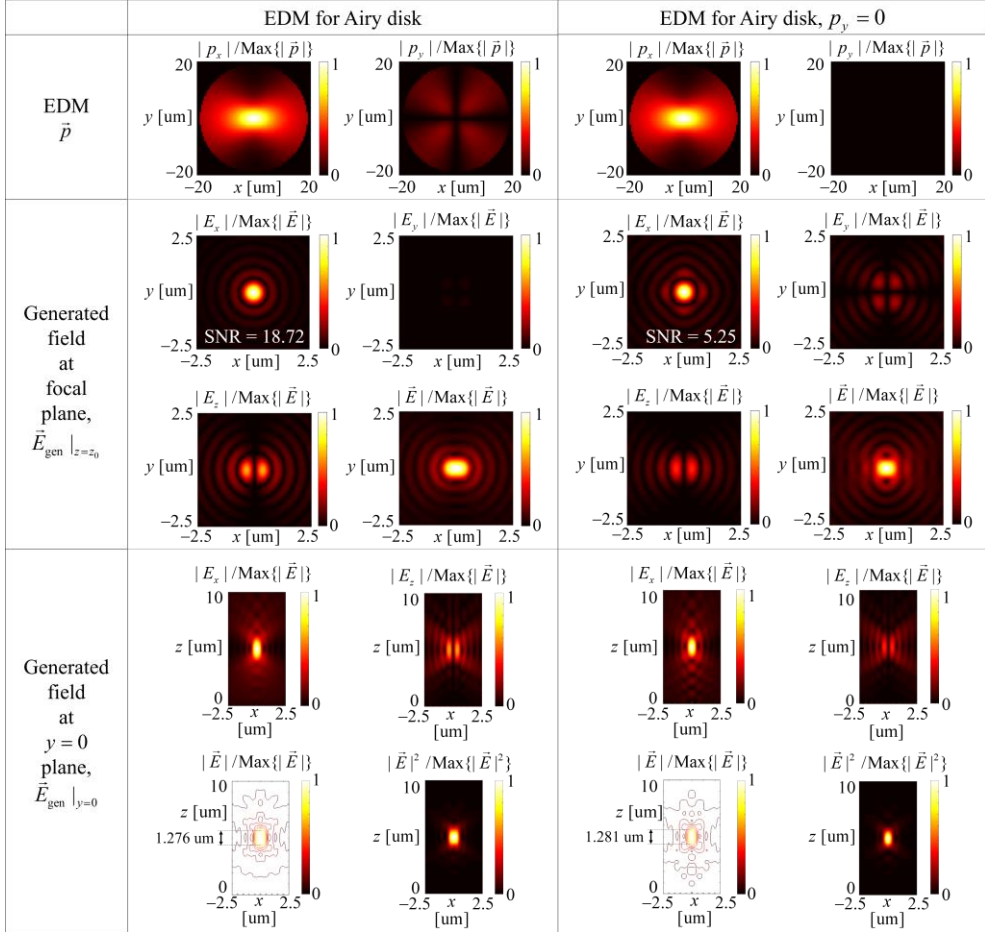


Figure 5.3 Comparison between EDM distributions generating the amplitude of normalized Airy disk with $NA = \sin(75^\circ) = 0.966$, $z_0 = 5 \text{ um}$, $k_0 = 2\pi / (1 \text{ um})$, and the reconstructed field distributions of an EDM for an x -polarized Airy disk (left column) and an EDM with a nullified p_y (right column).

The distribution of electric dipoles of the EDM for the generation of an x -polarized Airy disk is presented in the left panel of Fig. 5.3. The electric dipoles are placed at the two-dimensional isotropic grid with the grid size Λ . According to the Nyquist-sampling theorem, the grid size should satisfy $\Lambda \leq \lambda / 2$, where λ is the wavelength of optical field. In this chapter, $\Lambda = \lambda / 2$. An Airy disk with any polarization is realizable at an arbitrary position via the superposition of x - and y -polarized Airy disks. As depicted in Fig. 5.3, the amplitude distribution of the electric field is anisotropic due to the z -component of the electric field, which is required to satisfy the transversality of electromagnetic waves.

In Fig. 5.3, the amplitude distributions of the electric dipole moments for EDMs and the corresponding radiated field distributions are presented. Given the focal length $z_0 = 5 \text{ um}$ and the numerical aperture $\text{NA} = \sin(75^\circ) = 0.966$, the E_x is almost the same as the Airy disk $2J_1(\text{NA} \cdot k_0 \rho) / \rho$. Quantitatively, the quality of the constructed x -polarized Airy disk via the proposed EDM can be measured by the SNR:

$$\text{SNR} = \frac{\left[\iint |\alpha J_1(\text{NA} \cdot k_0 \rho) / \rho|^2 dx dy \right]}{\left[\iint (|E_x - \alpha J_1(\text{NA} \cdot k_0 \rho) / \rho|^2 + |E_y|^2) dx dy \right]}, \quad (5.9)$$

where $\alpha = \left\{ \left[\iint (|E_x|^2 + |E_y|^2) dx dy \right] / \left[\iint |J_1(\text{NA} \cdot k_0 \rho) / \rho|^2 dx dy \right] \right\}^{1/2}$ normalizes the Airy disk with respect to the transverse field of the radiated field of the EDM on the focal plane. The SNR of the x -polarized Airy disk via the EDM is estimated

to be 18.72.

The necessity of the cross-polarized dipole component p_y can also be examined by comparing the SNR of the EDM described in Eq. 5.6 with that of the EDM that only has p_x . As shown in the right column of Fig. 5.3, the SNR of the p_y -nullified EDM is calculated to be 5.25, which is far less than that of the EDM with p_y . As seen in Fig. 5.3, by nullifying p_y , the amplitude distribution of E_x on the focal plane $z = z_0$ is distorted compared with that of the ideal Airy disk, and the cross-polarized component of electric field E_y clearly exists. It means that the proposed EDM described in Eq. 5.6 precisely generates an Airy disk. The minimizing property of the focal volume is presented in Fig. 5.3. From a practical viewpoint, both the z -directional depth resolution of the Airy focus and the transversal x - y resolution are important. The z -directional spot size in both cases are similar: 1.276 μm and 1.281 μm . The minimization of the focal spot in three dimensions is achieved in the form of the Airy disk generated via the proposed EDM.

Let me conclude this subsection by giving some comments on generating x -polarized Airy disk via the corresponding EDM with in-plane dipole moment density as stated in Eq. 5.6. This result is straightforwardly generalized to the generation of arbitrarily polarized Airy disks by superposing x - and y -polarized Airy disks with the same focal spot and NA. Thanks to the regularized meta-atoms, superposition of corresponding EDMs is simply done by summing in-plane electric

dipole moment density of the EDMs. Further, since Fourier components of the electric field at the focal plane forms a uniform disk, the proposed Airy disks can be used as unit elements of reconstructing sampled wavefront without any distortion. In other words, as argued at the start of this section, linearly-polarized Airy disks are considered as virtual Huygens' sources having near-ideal radiation pattern, as seen in Sec. 2.4.

5.3.2 Bessel-Gauss beam

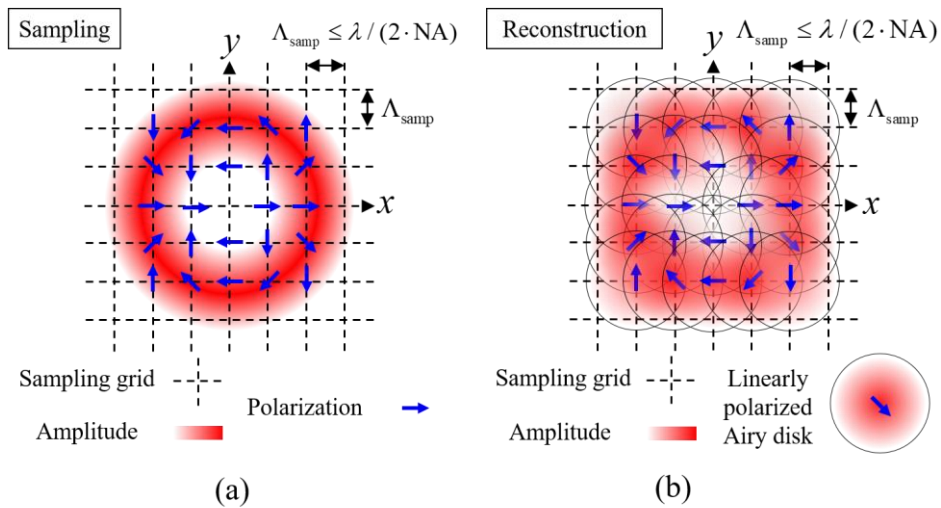


Figure 5.4 Schematics for the (a) sampling and (b) reconstruction scheme for a Bessel-Gauss beam with topological charge $m = 2$.

This subsection is devoted to describing sampling and reconstruction of arbitrary optical wavefront by exploiting linearly-polarized Airy disks as virtual Huygens'

sources with ideal radiation pattern as described in Sec. 2.4.

As an example of vector optical wavefront with a high divergence angle, Bessel-Gauss beam is selected [150-155]. A Bessel-Gauss beam on the focal plane is given as follows:

$$\begin{cases} E_x(\rho, \theta) = \cos(m\theta) \cdot \exp(-\rho^2 / w_0^2) \cdot J_m(\beta\rho) \\ E_y(\rho, \theta) = \sin(m\theta) \cdot \exp(-\rho^2 / w_0^2) \cdot J_m(\beta\rho), \end{cases} \quad (5.10)$$

where m is the topological charge of the Bessel-Gauss beam, w_0 and β determine the number of rings and the size of the beam, respectively, and $J_m(x)$ is an m -th order Bessel function of the first kind [157]. Figure 5.4(a) displays a Bessel-Gauss beam of topological charge $m = 2$. In Fig. 5.4(b), the Bessel-Gauss beam is decomposed into periodically arranged linearly polarized Airy disks whose amplitudes, phases, and polarizations are obtained from the sampling process of the transverse electric field as shown in Fig. 5.4(b). For a given NA, the sampling grid is set to satisfy the Nyquist sampling condition $\Lambda_{\text{samp}} \leq \lambda / (2 \cdot \text{NA})$, and the highest spatial frequency k_{max} of the considered beam should meet the inequality relation $k_{\text{max}} / k_0 \leq \text{NA}$. The later condition ensures that there is no loss of information during the reconstruction process by taking account of sufficiently high-NA. The transverse electric field for the Bessel-Gauss beam on the focal plane is linear as described in Eq. 5.10. The linearly polarized Airy disks, whose numerical aperture is defined by the sampling period Λ , are superposed to reconstruct the Bessel-Gauss beam.

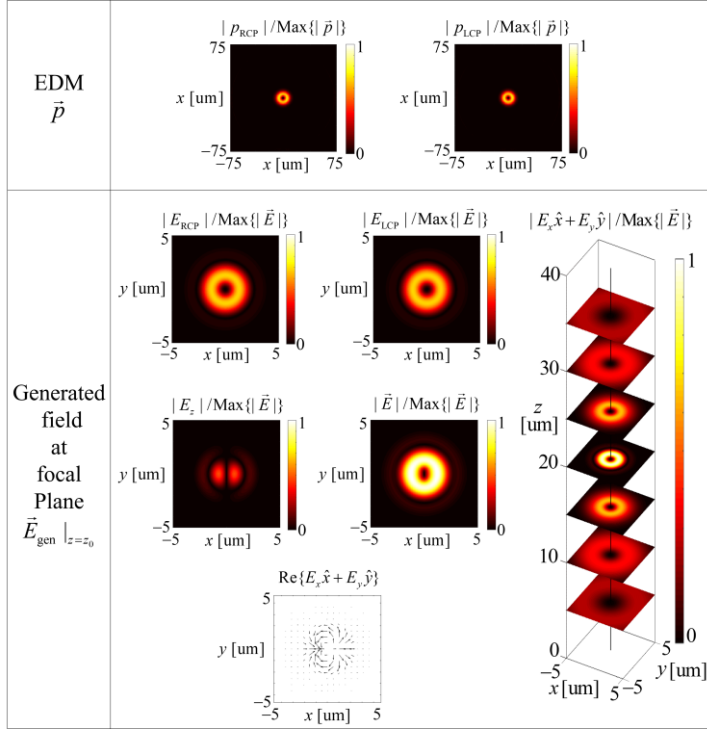


Figure 5.5 Generation of the Bessel-Gauss beam of the topological charge 2 via the EDM by sampling the transverse electric field on the focal plane $z = z_0 = 20 \text{ um}$. The amplitude distributions of p_{RCP} and p_{LCP} of the corresponding EDM (upper row) that generate the Bessel-Gauss beam. Plots of the amplitude distributions of E_{RCP} , E_{LCP} , E_z , and \vec{E} of the generated wavefront and the distribution of the polarization of the transverse electric field on the focal plane, and amplitude distributions of the transverse electric field at $z = 5, 10, 15, 20, 25, 30$ and 35 um (lower row).

The transverse electric field is sampled at the sampling grid points as seen in Fig. 5.4(a) so that the transverse electric field of the Bessel-Gauss beam on the focal plane is linearly polarized. Considering a Bessel-Gauss beam with parameters $m=2$, $w_0=2\lambda$, $\beta=0.3k_0$, and $\lambda=1\text{ }\mu\text{m}$, numerical testing confirms that the corresponding EDM precisely generates the target Bessel-Gauss beam in Fig. 5.5. The focal plane is placed at $z=z_0=20\text{ }\mu\text{m}$, and the corresponding EDM is at $z=0\text{ }\mu\text{m}$. The numerical aperture is set as $\text{NA}=\sin 75^\circ=0.966$ to reconstruct all of the angular spectra of the Bessel-Gauss beam. Figure 5.5 illustrates that the EDM generates a donut-shaped, wavefront with spatially varying polarization. The peak signal-to-noise ratio (PSNR) of the reconstructed wavefront seems to be proportional to the SNR of elementary Airy disks, so to achieve a high PSNR in the reconstructed wavefront, the SNR of the elementary Airy disk needs to be high.

5.3.3 Hologram

The sampling and reconstruction scheme introduced in the previous subsection can also be applied to generate high quality holograms via the proposed EDM. Consider the generation of a circularly polarized hologram defined by the image in Fig. 5.6(a). Figure 5.6(b) shows that an EDM with focal length $z_0=5\text{ }\mu\text{m}$ and fixed $\text{NA}=\sin 75^\circ=0.966$ produces a low-noise, right-handed circular polarization (RCP) hologram with the left-handed circular polarization (LCP) field component greatly suppressed. The PSNR is 76.81.

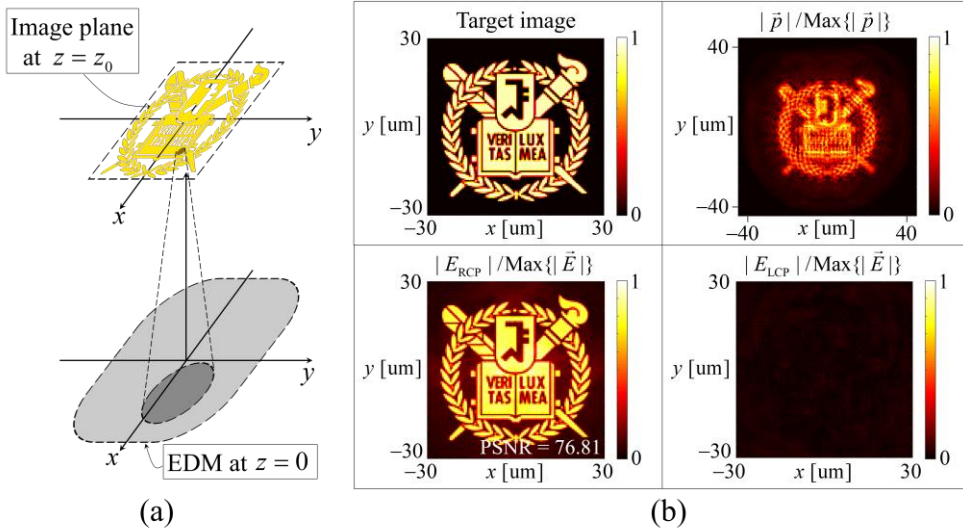


Figure 5.6 (a) Schematic for hologram generation. EDM on the plane $z=0$ illuminated by normally incident LCP plane wave along the $+z$ -axis is derived by the superposition of sampled Airy disk units on the image plane $z=z_0=5 \text{ um}$. (b) Plots of the target image, the electric dipole distribution of the EDM, and the corresponding field distributions on the image plane. The wavelength $\lambda=1 \text{ um}$. The PSNR is 76.81.

In the next section, to find the conditions necessary for the practical realization of ideal EDM meta-atoms, the quality of the reconstructed hologram from practical geometric phase metasurfaces is compared with that of the reconstructed hologram obtained using the EDM in Fig. 5.6.

5.4 Analysis of field generation via EDMs

In this section, I would like to analyze properties of the proposed EDM in detail. As already discussed in Sec. 5.3, SNR or PSNR can be defined to quantify the portion of noise with respect to the reconstructed signal. Generated optical wavefront is decomposed into periodic array of unit Airy elements, SNR of unit Airy elements determines overall performance. In the previous section, EDM of linearly-polarized Airy disks is derived under the assumption of one-to-one correspondence between a point on the EDM plane and Fourier components of the Airy disk. More rigorous approach is possible, and it is justified in the subsection 5.4.2. However, this is used only in this section because of heavy computational cost.

5.4.1 Signal-to-noise ratio analysis

To understand the properties of noise in generated optical wavefronts via the proposed EDMs, dependence of SNR on the focal length z_0 and the numerical aperture NA is studied. In Fig. 5.7, the electric field distributions of the residual field EDMs on the $z = z_0$. According to the numerical results, the SNR is improved by increasing z_0 and NA. For a fixed NA, a longer z_0 implies that the distribution of electric dipole moments on the EDM varies more slowly. Meanwhile, for a fixed z_0 , an EDM with larger NA generates an x -polarized Airy disk with less distorted sidelobes, as depicted by the intensity distributions of the

residual fields for the four selected EDMs on the corresponding focal plane in Fig. 5.7. The sidelobes of the Airy disk are properly reconstructed when z_0 and NA are large enough. The peak intensity of the residual field is also greatly suppressed.

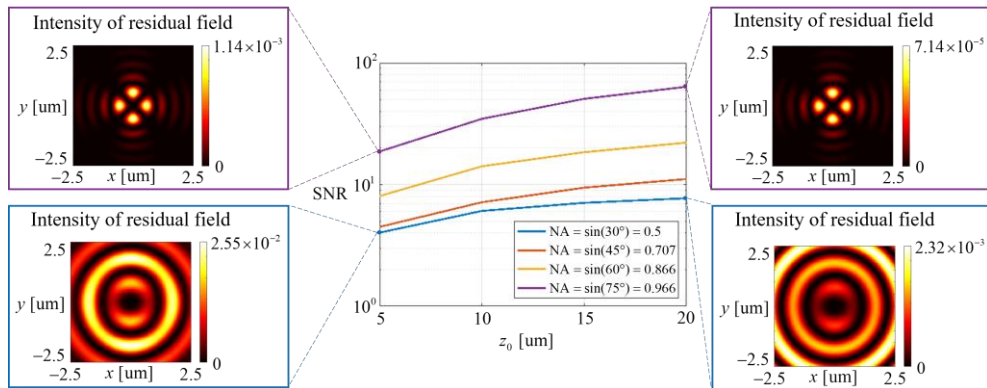


Figure 5.7 z_0 –SNR semi-log plot (center) for various NAs and focal lengths for EDMs. Four intensity profiles (the four corners of the figure) of the residual fields, which represent the difference between E_x generated by the EDM and the Airy disk on the focal plane.

5.4.2 Derivation of wave-optical EDMs

As I mentioned at the beginning of this section, there are an implicit assumption of one-to-one correspondence between a point on the EDM plane and Fourier components of the Airy disk. This assumption allows the intuitive derivation of EDM with smooth in-plane electric dipole density. However, as seen in Sec. 2.5, superposition of plane waves and its corresponding EDMs will give more accurate

form of in-plane electric dipole density of EDM. As virtual Huygens' sources, linearly-polarized Airy disks generated by the EDMs derived in the previous section suffer from moderate SNR for the case of short z_0 and small NA. This limitation can be overcome by extensive use of Fourier transform of field distribution and dipole density distribution. Recall Eq. 5.1 which describes the Fourier transform of the tangential electric field distribution of an Airy disk. It is related to the Fourier transform of the in-plane electric dipole distribution:

$$\mathcal{F}\{\vec{p}_{\text{tan}} \cdot \hat{k}_\rho\} = \frac{(\mathcal{F}\{\vec{G}_{\text{ideal}}\} \cdot \hat{k}_\rho) \cdot \hat{k}_\rho}{(\mathcal{F}\{\vec{G}_\rho\} \cdot \hat{k}_\rho) \cdot \hat{k}_\rho} (\vec{\mathcal{E}}_{\text{tan}} \cdot \hat{k}_\rho) e^{ik_z z_0} = \frac{1}{\cos\theta} \cos\phi e^{ik_z z_0}, \quad (5.11)$$

and

$$\mathcal{F}\{\vec{p}_{\text{tan}} \cdot \hat{k}_\phi\} = \frac{(\mathcal{F}\{\vec{G}_{\text{ideal}}\} \cdot \hat{k}_\phi) \cdot \hat{k}_\phi}{(\mathcal{F}\{\vec{G}_\rho\} \cdot \hat{k}_\phi) \cdot \hat{k}_\phi} (\vec{\mathcal{E}}_{\text{tan}} \cdot \hat{k}_\phi) e^{ik_z z_0} = -\cos\theta \sin\phi e^{ik_z z_0} \quad (5.12)$$

for generation of x -polarized Airy disk.

Numerical results on the EDM used in the previous chapters, denoted by ray-optical EDM (ROEDM), and the EDM derived in Eqs. 5.11 and 5.12, denoted by wave-optical EDM (WOEDM), are provided in Fig. 5.8. x -polarized Airy disks of $z_0 = 5 \text{ um}$ and $\text{NA} = \sin(45^\circ) = 0.707$ are generated by the corresponding ROEDM and WOEDM, respectively. It is clearly seen that in-plane dipole distribution of WOEDM has ripples, unlike ROEDM. SNR of the x -polarized Airy disk generated by the corresponding WOEDM is 319.9, whereas SNR of the same

Airy disk generated by the corresponding ROEDM is 4.488. It is noted that phase distribution of the generated field via WOEDM at focal plane is nearly ideal. By replacing ROEDM with WOEDM, about hundred-fold enhancement of SNR is observed for the case of short z_0 and small NA.

Without any loss of generality, ROEDM can be replaced by WOEDM for suppressing noise level. In this chapter, however, ROEDMs are extensively used to design EDMs with much smaller computational cost.

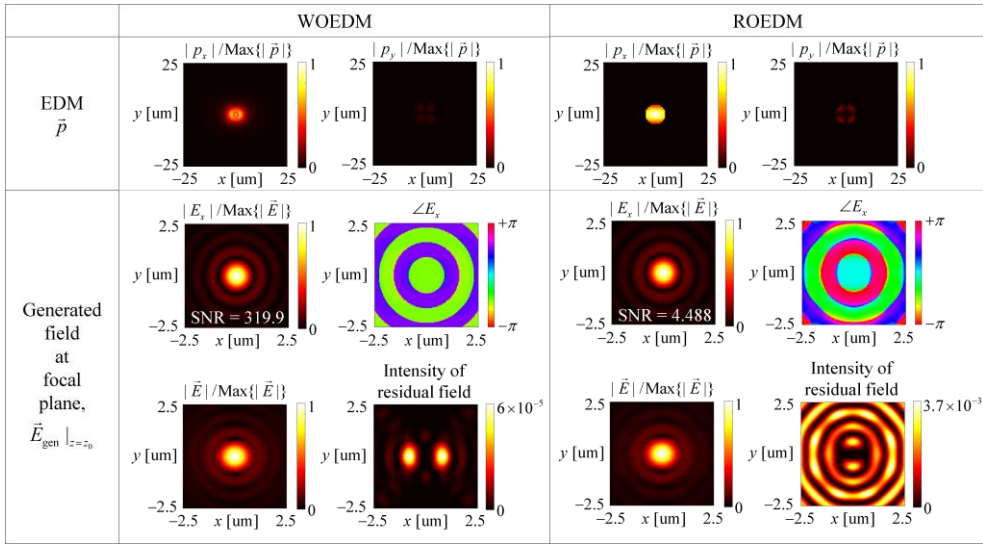


Figure 5.8 Comparison between WOEDM and ROEDM generating x -polarized Airy disks with $\text{NA} = \sin(45^\circ) = 0.707$, $z_0 = 5 \text{ um}$, and $k_0 = 2\pi / (1 \text{ um})$. In-plane electric dipole distribution (upper row) and the generated field at the focal plane (lower row).

5.5 Realization of electric dipole metasurfaces

This section is devoted to realization of EDMs by proposing and analyzing supercell metasurfaces. Designing arrangement of meta-atoms in supercells is crucial to ‘quasi-regularization’ of radiation patterns of supercells. I would like to start with defining the term ‘quasi-regularization’.

5.5.1 Quasi-regularization of radiation patterns for metasurfaces

Hypothesized meta-atoms in the previous sections are equipped with complex amplitude modulation and arbitrary polarization. As described in Sec. 5.1, such meta-atoms with optically thin thickness are currently unavailable. In Chapter 3, it is shown that meta-atoms having complex modulation capability compatible with regularized radiation patterns are realizable but requires optically thick structures. They also suffer from multiple interactions. In turn, strong light-matter interaction is not preferred, and consequently overall efficiency is low. In practice, a simple design having acceptable efficiency and noise level is preferred.

Here, I propose quasi-regularization process: it considers the arrangement of meta-atoms in supercell metasurfaces to roughly equalize supercells’ radiation patterns. The electric dipole distribution for the EDM presented in Figs. 5.3 and 5.6 are used in the comparative test. It is noted that the terms ‘unit cell’, ‘supercell’, and ‘meta-molecule’ are interchangeable in dealing with supercell metasurfaces. If each unit cell of metasurface contains single meta-atom, then the terms ‘unit cell’ and ‘meta-atom’ are interchangeable.

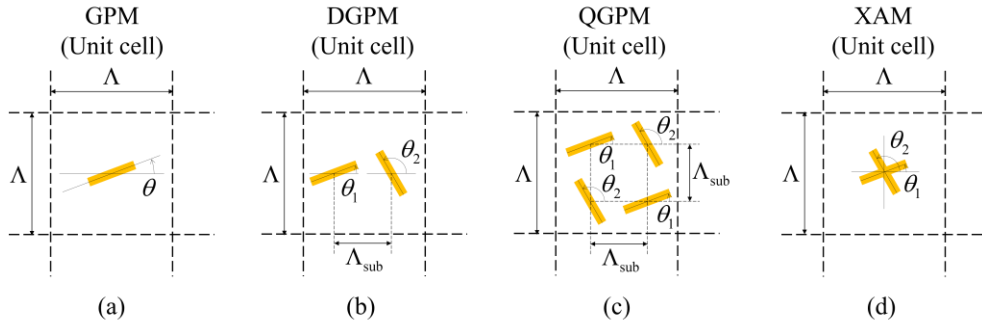


Figure 5.9 Schematics of (a) unit cell of GPM, (b) unit cell (supercell) of DGPM, (c) unit cell (supercell) of QGPM, and (d) unit cell of XAM.

Many metasurfaces use a geometric phase scheme to generate circular-polarized spatially modulated wavefronts. Under the illumination of a circular polarized ($+\sigma$) plane wave normal to the geometric metasurface, the phase of the cross-polarized field is modulated by the geometric phase structure [70, 79-82].

As a method to extend the phase-only modulation capability of geometric phase metasurfaces to the complex modulation of both amplitudes and phases, supercell metasurfaces have received a great deal of research attention [70, 80, 156]. Supercell structures that include a few meta-atoms are considered to be a single macro meta-molecule featuring complex amplitude modulation characteristics. Geometric phase metasurfaces (GPMs), of which unit cell (meta-

atom) are illustrated in Fig. 5.9(a), is categorized as EDMs. Dielectric rods with rotating angle θ act as efficient linearly polarized meta-atoms with 2θ phase modulation. Metasurfaces capable of complex amplitude modulation can be designed by combining two GPMs into a supercell metasurface as depicted in Fig. 5.9(b), producing a double geometric-phase metasurface (DGPM). Given the normalized amplitude and phase modulation of $A\exp(i\phi)$, the rotation angles θ_1 and θ_2 of the two nano-rod antennas are determined by the design equation

$$\begin{cases} \theta_1 - \theta_2 = \cos^{-1} \eta A \\ \theta_1 + \theta_2 = \phi \end{cases}, \quad (5.13)$$

where η is a proportionality constant that controls maximum amplitude. If η is small, the two elementary antennas act as two independent phase-modulated dipoles generating a linear superposition of respective dipole fields.

Quadruple geometric-phase metasurfaces (QGPMs) combine four GPMs into one (Fig. 5.9(c)). Meta-atoms of X-shaped antenna metasurfaces (XAMs) merge two elemental tilted rod antennas into single X-shape antenna [156], as illustrated in Fig. 5.9(d). GPMs, DGPMs, QGPMs, and XAMs generate an RCP wavefront with a DC plane wave of opposite polarization under the illumination of an LCP plane wave on the metasurfaces. It should be noted that Λ_{sub} is the distance between nearby nano-rod antennas of unit cells of DGPMs and QGPMs. To minimize mutual interactions of nano-rod antennas, $\Lambda_{\text{sub}} = \Lambda / 2$ in this section.

To sum up, GPMs are capable of full phase modulation for single circular

polarization. DGPMs and QGPMs are supercell metasurfaces for achieving complex amplitude modulation capability. QGPMs are quasi-regularized in comparison to DGPMs because C2 symmetry of unit cells of QGPMs efficiently suppresses second lowest multipole radiation: magnetic dipole component. Meta-atoms of XAMs are expected to have regularized radiation patterns, but efficiency is fundamentally limited, and mutual interaction of arms of X-shaped antenna gives distortion of both complex amplitude and radiation pattern. The performance of wavefront generation by these four types of metasurfaces is examined in the following subsections.

5.5.2 Generation of circularly polarized Airy disk

In this subsection, I would like to analyze the role of quasi-regularization by comparing the generated circularly polarized Airy disks of the four metasurfaces - GPM, DGPM, QGPM, and XAM. Figure 5.10 shows the local field distribution of the RCP Airy disk for the four metasurfaces around the focal spot. For analysis, the SNR_{RCP} is defined as

$$SNR_{RCP} = \frac{\left[\iint |\alpha J_1(NA \cdot k_0 \rho) / \rho|^2 dx dy \right]}{\left[\iint (|E_{RCP} - \alpha J_1(NA \cdot k_0 \rho) / \rho|^2) dx dy \right]}, \quad (5.14)$$

where $\alpha = 2 \cdot \text{Max}\{|E_{RCP}|\} / (NA \cdot k_0)$ to equalize the peak values of the calculated RCP field and the RCP Airy disk. The SNR_{RCP} for the DGPM, QGPM,

and XAM was 1.024, 1.932, and 4.347, respectively.

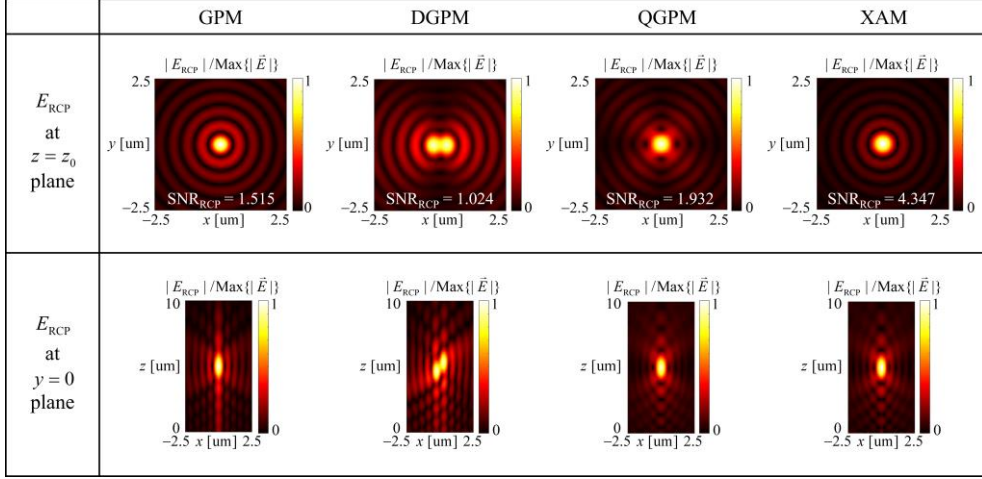


Figure 5.10 Amplitude distribution of the E_{RCP} for the unit RCP Airy disks via the DGPM, QGPM, and XAM on the focal plane $z = z_0 = 5 \text{ um}$ and on the $y = 0 \text{ um}$ plane (left panel). The three metasurfaces have the $\text{NA} = \sin 75^\circ = 0.966$ and the wavelength $\lambda = 1 \text{ um}$.

The numerical result in Fig. 5.10 shows that XAMs have an advantage in that they regularize the radiation pattern to be the same as that of the RCP EDM, in turn nullifying the other multipole radiation terms. It should be noted that the QGPM has a moderate SNR_{RCP} because the magnetic dipole radiation is suppressed by the C2 symmetry of the meta-atoms in a molecule of the QGPM. The DGPM failed

to form a single focal spot, producing instead two three-dimensionally separated focal spots away from the intended position $(x, y, z) = (0, 0, 5 \text{ um})$, as seen in Fig. 5.10. In terms of the SNR, the performance of the XAM is close to that of the EDM.

The comparative study of GPMs, DGPMs, QGPMs, and XAMs indicates that the radiation patterns of the meta-molecules are crucial to the generation of extremely high SNRs for high-NA focal spots.

5.5.3 Hologram

By exploiting the sampling-reconstruction process introduced in the previous subsection, hologram of arbitrary image profile is successfully reconstructed on the focal plane. GPMs, DGPMs, QGPMs, and XAMs are used to make the same target image in Fig. 5.6(b).

Figure 5.11 depicts the comparative study of the quality of hologram generated by the four types of metasurfaces. The resultant PSNR was 1.696, 7.894, 21.18, and 27.38, respectively, following the similar order as the SNR_{RCP} of the corresponding unit Airy disks. GPMs do not have complex amplitude modulation capability, which significantly harms the quality of the reconstructed hologram. Thus, not only complex amplitude modulation but also regularization process is important in ensuring the quality of the hologram image. The quasi-regularization process introduced in this section effectively realizes the complex amplitude modulation capability of meta-atoms with suppressed multipole radiation components.

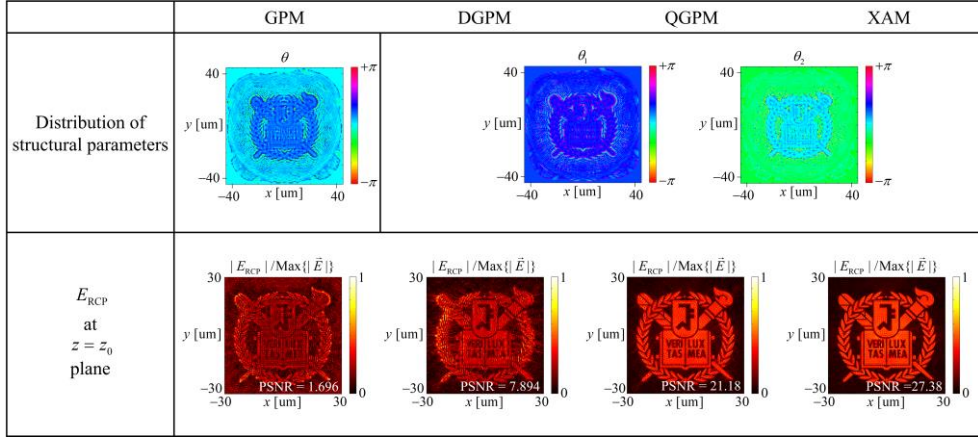


Figure 5.11 The holograms of the same target image in Fig. 5.6(b) are generated via the conventional metasurfaces DGPM, QGPM and XAM, respectively, at the focal plane $z_0 = 5 \text{ um}$. The corresponding structural parameters θ , θ_1 , and θ_2 are also presented (upper row).

For practical applications, efficiency of the considered metasurfaces is briefly discussed. Diffraction efficiency of meta-molecules of transmissive GPMs reaches $1/2$, assuming that low-reflection design is applied to the meta-molecules. Here, efficiency of the metasurfaces for generating a wavefront is calculated as the ratio of optical power of the generated signal to the incident power. This definition accounts for the quality of the generated wavefront as well as diffraction efficiency of meta-molecules. For example, in Fig. 5.11, the efficiencies of the DGPM, QGPM, and XAM are estimated to be 0.444, 0.477, and 0.236, respectively. The proportional constant η of the XAM is chosen as 0.7 which guarantees moderate

interaction between arms of each meta-molecule of the XAM. GPMs for generating such large bandwidth holograms suffer from low efficiency, due to their low PSNR.

5.6 Experimental demonstration

5.6.1 Fabrication and experimental setup

To demonstrate complex modulation capability of QGPMs and XAMs together with low noise level, GPM, DGPM, QGPM, and XAM for generating an amplitude hologram are fabricated and measured. Since hundreds of micron sized array of nano-antennas is required to get clear CCD images of holograms, e-beam lithography is used to implement the metasurfaces. A detailed recipe of e-beam lithography used in the experiment is described as follows. 2% dilution of 495 PMMA (polymethyl methacrylate of 495,000 molecular weight, solvent: Anisole, $\text{CH}_3\text{OC}_6\text{H}_5$) was spin-coated on a quartz plate with 2000 rpm and pre-baked at 180 °C for 3 min on a hot plate. 2% dilution of 950 PMMA (solvent: Anisole) was spin-coated on the spin-coated sample with 3000 rpm and pre-baked at 180 °C for 5 min on a hot plate. Then, e-spacer (300Z) was spin-coated to prevent charging effect during e-beam lithography. The spin-coated sample was patterned by e-beam lithography (JEOL-6300FS, JEOL USA, Inc.) with accelerating voltage 100kV, current 1nA, dose 770 $\mu\text{C}/\text{cm}^2$. The patterned sample was developed by soaking in MIBK/IPA (1:3) for 1min 30sec, rinsing in IPA for 20 sec, and DI water cleaning for 15sec. Then, each pattern has undercut profile for lift-off process. Thermal deposition was conducted to form silver nano-antennas of 50 nm thickness with the adhesion layer Cr of 2 nm thickness. Finally, lift-off process was performed after overnight acetone soak. Overall fabrication process is illustrated in Fig. 5.12(a).

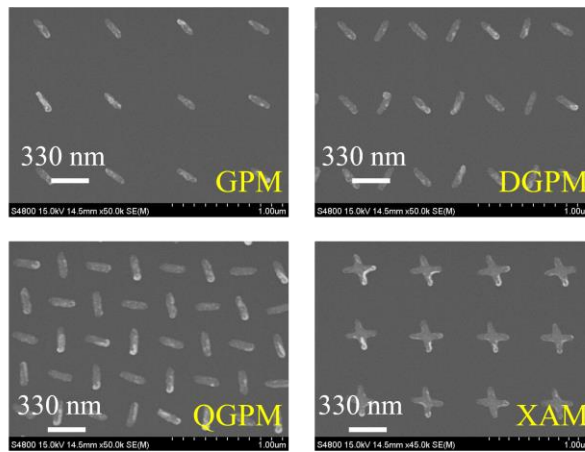
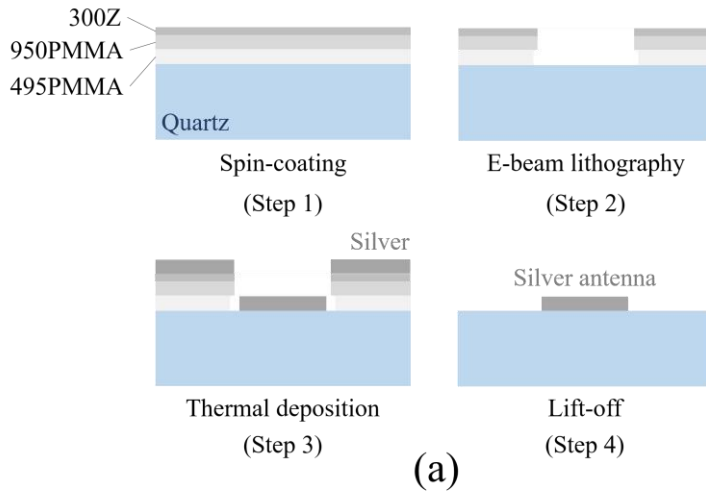


Figure 5.12 (a) Schematic of fabrication process of forming nano-antennas on a quartz plate. (b) SEM images for fabricated samples of GPM, DGPM, QGPM, and XAM, respectively.

The fabricated sample was examined by SEM images of a portion of GPM, DGPM, QGPM, and XAM as presented in Fig. 5.12(b). Intended size of antennas in GPM, DGPM, QGPM is $250 \text{ nm} \times 50 \text{ nm} \times 50 \text{ nm}$ (length, width, and height), and intended size of X-shaped antennas in XAM is $330 \text{ nm} \times 50 \text{ nm} \times 50 \text{ nm}$ (length of diagonal bars, width of arms, and height). The actual length is shortened because of the characteristic of e-beam lithography. The size of supercells is 660 nm , and the wavelength is 660 nm (laser diode). The fabricated samples have the size of $142.72 \text{ } \mu\text{m} \times 142.72 \text{ } \mu\text{m}$ (223×233 samples). Thus, first-order diffracted components exist but overall quality did not change much in the experiment.

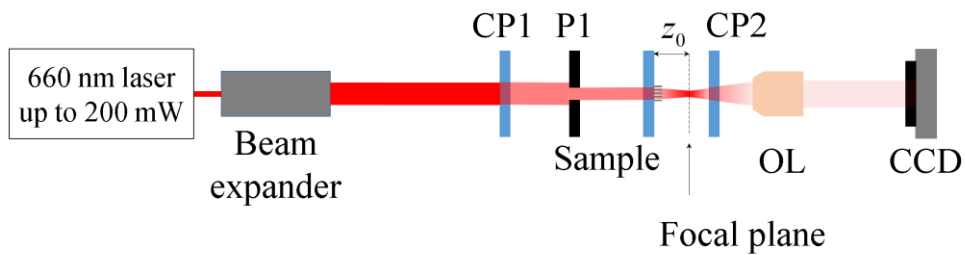


Figure 5.13 Schematic of experimental setup for measurement of hologram of geometric phase based metasurfaces.

Figure 5.13 shows the experimental setup to image the holograms at the focal plane at the CCD. Torus single longitudinal mode (SLM) 660 nm continuous-wave laser (Laser Quantum UK, Stockport, UK) is used for the coherent source, and the expanded beam is converted to circularly-polarized plane wave by polymer circular polarizer (CP1). The sample is illuminated by the circularly-polarized wave, and its

cross-polarized hologram constructed at the focal plane is collected by an objective lens (Nikon, $\times 10$, NA = 0.25) and imaged to the CCD camera.

5.6.2 Hologram generation

Hologram generation via the four metasurfaces is demonstrated as in Fig. 5.14. The target image of the holograms is shown in Fig. 5.14(a), the size of the holograms is $100 \text{ um} \times 100 \text{ um}$ at the focal plane $z = z_0 = 20 \text{ um}$. Optical microscope image of the patterned area of the metasurfaces looks like a translucent square as shown in Fig. 5.14(b). CCD images of the corresponding holograms of GPM, DGPM, QGPM and XAM are displayed in Figs. 5.15. The experimental results agree with the noise analysis derived by numerical results. Since QGPM have quasi-regularized radiation patterns of supercells, complex modulation capability enables to generate holograms with high contrast. X-shaped antennas of XAM have regularized radiation patterns, but its amplitude modulation depth is $\eta < 1$, limiting conversion efficiency of XAMs. $\eta = \sqrt{3}/2 \approx 0.866$ for the fabricated samples in the conducted experiment.

It should be noted that SNR_{RCP} defined in Eq. 5.14 cannot be calculated through CCD images. Interferometric experiments should be conducted to analyze SNR properties of the metasurfaces for examining complex modulation capability. Moreover, size of individual antennas is not optimized to achieve high efficiency.

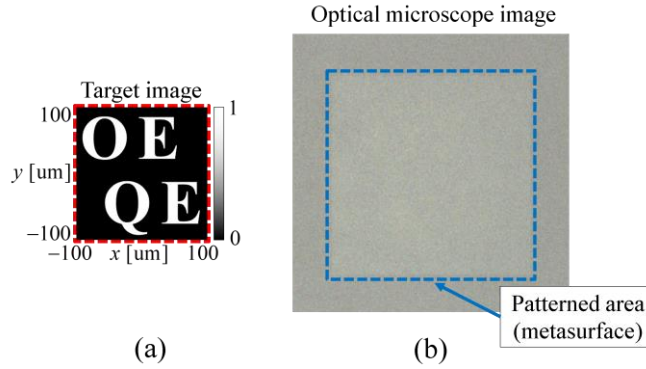


Figure 5.14 (a) Target image of the holograms, (b) optical microscope image of a patterned area of a QGPM sample.

| | GPM | DGPM | QGPM | XAM |
|---|-----|------|------|-----|
| Unit cell | | | | |
| CCD image (NA = 0.25) | | | | |
| Numerically derived hologram (NA = 0.5) | | | | |

Figure 5.15 Schematic of unit cell of GPM, DGPM, QGPM, and XAM, respectively (top panel). The corresponding CCD images of hologram (middle panel), and the numerically derived results of the same target image in Fig. 5.14(a) (bottom panel).

PSNRs of the holograms generated by GPM, DGPM, QGPM, and XAM are 1.307, 21.13, 68.51, 73.28, respectively. Performances of the four metasurfaces can be compared by defining figure of merit (FoM) as

$$(\text{FoM}) = (\text{average scattering efficiency}) \times (\text{PSNR}), \quad (5.15)$$

so that not only relative noise level but also intensity of signal is considered for practical applications. Then, scattering efficiency of XAMs used in the experiment is below 0.1%, and maximal scattering efficiency of the others is 3.8%. The relative FoMs of the four metasurfaces are calculated as 0.01907 (GPM), 0.3084 (DGPM), 1 (QGPM), and below 0.1426 (XAM), respectively. GPM has regularized radiation patterns but cannot give complex amplitude modulation capability. DGPM has non-regularized radiation patterns but can give complex amplitude modulation. QGPM has quasi-regularized radiation patterns and can give complex amplitude modulation. XAM has regularized radiation patterns and can give complex amplitude modulation. However, the XAM used in the experiment suffers from not only low efficiency but also mutual interaction between bars. Quasi-regularization by reducing multipole components offers a practical design scheme considering radiation patterns for low-noise generation of optical fields.

5.7 Conclusion

In this chapter, a scheme for generating arbitrary optical field is proposed by generalizing optical wavefront generation method described in Chapter 2. More specifically, assuming meta-atoms having in-plane polarized electric dipoles with designated complex amplitude are available, metasurfaces constructed by periodically arranging these meta-atoms enable to generate a linearly polarized Airy disk as a virtual Huygens' source. Since Fourier components of the Airy disk is a vector version of ideal Huygens' source, superposing periodically separated Airy disks can serve as sampling elements. EDM that is the superposition of the corresponding EDMs generates arbitrary wavefront with extremely low noise. Approximation of the proposed EDMs are made by applying 'quasi-regularization', then various supercell metasurfaces are proposed and examined as approximate version of EDMs. Signal-to-noise analysis for the generated wavefronts including Airy disks, Bessel-Gauss beam, and hologram of various metasurfaces are compared. Experimental results approve the notion of quasi-regularization to engineer supercell metasurfaces with respect to radiation patterns of supercells. It should be noted that double-lined slit array is the quasi-regularized version of ideal Huygens' sources. Other metasurfaces suffer from severe distortion if target wavefront has broad spatial bandwidth. It is expected that this study has opened possibility of engineering radiation patterns to achieve unprecedented level of controllability of generating and modulating optical wavefronts at will via metasurfaces. Metasurface of optically non-negligible thickness is worthy of

research to realize the most general form of the proposed EDMs.

Chapter 6 Conclusion

The main focus of this dissertation is to investigate and emphasize the role of radiation patterns of meta-atoms in metasurfaces and meta-slits. Starting from historical overview of Huygens' principle and Huygens' principle-based optical diffraction theories, throughout this dissertation, Huygens' sources refer to electromagnetic localized sources. Natural choices of Huygens' sources are electric dipole and magnetic dipole Huygens' sources. Its implementation by adopting basic forms of meta-atoms is discussed. I show that plane wave is easily constructed by meta-atoms of which radiation patterns are regularized. In addition, I show that ideal Huygens' sources can be exploited to generate arbitrary wavefronts with unprecedentedly low noise level, so that it can be inferred that regularized Huygens' sources would serve as a platform of generating arbitrary optical and plasmonic fields.

To generate field distribution at will, it is crucial to find a way of realizing complex amplitude modulation of meta-atoms. I give concrete examples of meta-atoms compatible with regularization process. Metal-clad waveguides are extensively used to regularize overall radiation pattern of a set of independent meta-atoms inside each waveguide. The regularized pattern of an edge of metal-clad waveguide is magnetic dipole-like. The first type of the proposed meta-atoms is reflection-type complex amplitude modulators, which utilize coherent perfect absorption phenomena. I also investigate a fabricable design that is comprised of three-dimensional metal-clad square aperture waveguide attached to asymmetric

slit apertures at the end of the waveguide in 3.2.3. The study shows that CPA condition in two-independent parameter space gives a natural complex modulation mechanism nearby the condition, so that continuous control of complex amplitude of reflection coefficient is accomplished in the proposed design. The second type of the proposed meta-atoms is also using short metal-clad plasmonic waveguide to regularize each supercell's overall radiation pattern. According to the numerical study, introduction of waveguides does not break the complex amplitude modulation capability of supercell metasurfaces.

In Chapter 4, regularized meta-atoms are exploited to realize a novel method of generating plasmonic field. Metal-clad plasmonic waveguide array is proposed as an example of regularized meta-slits. Interestingly, an edge of metal-clad plasmonic waveguide radiates plasmonic field with near-ideal radiation pattern: magnetic dipole radiation pattern. In addition, complex amplitude modulation is accomplished by rotation angle and shift of tilted input slit of each metal-clad waveguide. Plasmonic focal spot and plasmonic Airy beam are successfully generated by the proposed structure of designated complex amplitude profiles. Numerical results including full-field are delivered to analyze the generated wavefronts in the sense of SNR. Especially, plasmonic focal spot generated by the proposed structure has hundreds-fold higher SNR than the field generated by double-lined slit array as a conventional meta-slit. Note that the double-lined slit array is one of the most efficient meta-slits for wavefront synthesis. In Chapter 5, this observation is partly justified by analyzing 'quasi-regularized' metasurfaces.

Experimental suggestion is also made.

In Chapter 5, by refining the wave synthesis method discussed in Chapter 2, I propose a novel type of metasurfaces, EDMs. an EDM is comprised of two-dimensional periodically arranged optical meta-atoms with designated complex amplitude electric dipole moment and arbitrary in-plane polarization. Although these hypothetical meta-atoms are not realized for optically thin metasurfaces, EDMs are capable of generating arbitrary optical wavefront with extremely low noise level according to the numerical results. Linearly polarized Airy disk generated by an EDM is analyzed, and I use this optical field as a virtual Huygens' sources to construct arbitrary optical field. A Bessel-Gauss beam and a Hologram can be constructed by EDMs and the generated fields are numerically analyzed in the sense of SNR. I also give more accurate form of EDMs by extensively using Fourier transform of optical field and dipole distribution. I also give a method to realize approximated versions of the proposed metasurfaces by proposing 'quasi-regularization'. DGPMs, QGPMs, and XAMs as the concrete examples of quasi-regularized metasurfaces are proposed and investigated. The comparative study of generating Airy disk, Bessel-Gauss beam, and hologram via the quasi-regularized metasurfaces in the sense of signal-to-noise ratio is presented. Experimental results on hologram generation of the presented metasurfaces are also provided.

I expect that this dissertation can help to develop advanced metasurfaces and meta-slits that account radiation patterns of meta-atoms for achieving full control of generating and manipulating optical and plasmonic field, respectively. Wide-

angle operation of spatial light modulators with extremely low noise level is viable by adopting the proposed regularization process. Future research on compact active modulation mechanism is needed.

Bibliography

- [1] C. Huygens, *Traité de la lumière*, Pieter van der Aa, Leiden, 1690.
- [2] T. Young, “Experiments and calculations relative to physical optics,” *Phil. Trans. R. Soc. Lond.* **94**, 1-16 (1804).
- [3] T. Young, “On the theory of light and colours,” *Phil. Trans. R. Soc. Lond.* **92**, 12-48 (1802).
- [4] T. Young, “An account of some cases of the production of colours, not hitherto described,” *Phil. Trans. R. Soc. Lond.* **92**, 387-397 (1802).
- [5] A. Fresnel, *Oeuvres complètes D’ Augustin Fresnel*, (Imprimerie Impériale, 1866).
- [6] A. Fresnel, “Mémoire sur la diffraction de la lumière,” in *Oeuvres complètes D’ Augustin Fresnel*, H. Desenarmont, E. Verdet, and L. Fresnel eds. (Imprimerie Impériale, 1866), 247-364 (1818).
- [7] J.Z. Buchwald, *The rise of the wave theory of light: Optical theory and experiment in the early nineteenth century* (University of Chicago, 1989).
- [8] E. T. Whittaker, *A history of the theories of aether and electricity from the age of Descartes to the close of the nineteenth century* (Longmans, Green and Co., 1910).
- [9] B. B. Baker and E. T. Copson, *The mathematical theory of Huygens’ principle* (Clarendon, 1939).
- [10] M. Born and E. Wolf, *Principles of Optics* (7th ed.) (Cambridge, 1999).

- [11] W. Greiner, J. Reinhardt, *Quantum electrodynamics* (Springer, 2008).
- [12] G. G. Stokes, “On the dynamical theory of diffraction,” *Trans. Cambridge Philos. Soc.* **9**, 1-62 (1849).
- [13] H. Helmholtz, “Theorie der Luftschwingungen in Röhren mit offenen Enden,” *J. Reine Angew. Math.* **57**, 1-72 (1860).
- [14] G. Kirchhoff, “Zur theorie der lichtstrahlen,” *Ann. Phys. (Leipzig)* **254**(4), 663-695 (1883).
- [15] A. Sommerfeld, “Mathematische theorie der diffraction,” *Math. Ann.* **47**, 317-374 (1896).
- [16] A. Sommerfeld, *Optics* (Academic, 1954).
- [17] L. Rayleigh, “On the passage of waves through apertures in plane screens, and allied problems,” *Philos. Mag.* **43**(263), 259-272 (1897).
- [18] J. A. Stratton and L. J. Chu, “Diffraction theory of electromagnetic waves,” *Phys. Rev.* **56**(1), 99 (1939).
- [19] W. Franz, “Zur formulierung des Huygensschen prinzipts,” *Z. Naturforsch. A* **3**, 500-506 (1948).
- [20] H. Levine and J. Schwinger, “On the theory of electromagnetic wave diffraction by an aperture in an infinite plane conducting screen,” *Commun. Pure Appl. Math.* **3**(4), 355-391 (1950).
- [21] C. J. Bouwkamp, “Diffraction theory,” *Rep. Prog. Phys.* **17**, 35-100 (1954).
- [22] B. Richards and E. Wolf, “Electromagnetic diffraction in optical systems I. An integral representation of the image field,” *Proc. R. Soc. Lond. A Math. Phys. Sci.*

253(1274), 349-357 (1959).

[23] B. Richards and E. Wolf, "Electromagnetic diffraction in optical systems II. Structure of the image field in an aplanatic system," Proc. R. Soc. Lond. A Math. Phys. Sci. **253**(1274), 358-379 (1959).

[24] C. J. R. Sheppard and P. Török, "Efficient calculation of electromagnetic diffraction in optical systems using a multipole expansion," J. Mod. Opt. **44**(4), 803-818 (1997).

[25] A. S. Marathay and J. F. McCalmont, "Vector diffraction theory for electromagnetic waves," J. Opt. Soc. Am. A **18**(10), 2585-2593 (2001).

[26] S. P. Anokhov, "Return to foundations of wave optics," Opt. Lett. **32**(15), 2209-2211 (2007).

[27] S. Guha and G. D. Gillen, "Vector diffraction theory of refraction of light by a spherical surface," J. Opt. Soc. Am. B **24**(1), 1-8 (2007).

[28] J. D. Jackson, *Classical electrodynamics* (Wiley, 1998).

[29] L. Novotny and B. Hecht, *Principles of nano-optics* (Cambridge University, 2012).

[30] A. E. H. Love, "The integration of the equations of propagation of electric waves," Philos. Trans. Royal Soc. A **197**, 1-45 (1901).

[31] J. Larmor, "On the mathematical expression of the principle of Huygens," Proc. Lond. Math. Soc. **1**, 1 (1903).

[32] W. v. Ignatowsky, "Diffraction und reflexion, abgeleitet aus den Maxwellschen gleichungen," Ann. Phys. (Leipzig) **328**(10), 875-904 (1907);

330(1), 99-117 (1907).

[33] H. M. Macdonald, "The integration of the equations of propagation of electric waves," Proc. Lond. Math. Soc. **2**(1), 91-95 (1912).

[34] F. Kottler, "Elektromagnetische theorie der beugung an schwarzen schirmen," Ann. Phys (Leipzig), **376**(15), 457-508 (1923).

[35] S. A. Schelkunoff, "Some equivalence theorems of electromagnetics and their application to radiation problems," Bell Sys. Tech. J. **15**(1), 92-112 (1936).

[36] J. A. Stratton and L. J. Chu, "Diffraction theory of electromagnetic waves," Phys. Rev. **56**(1), 99-107 (1939).

[37] W. Franz, "On the theory of diffraction," Proc. Phys. Soc. A **63**(9), 925-939 (1950).

[38] F. Wyrowski and M. Kuhn, "Introduction to field tracing," J. Mod. Opt. **58**(5-6), 449-466 (2011).

[39] B. Andreas, G. Mana, and C. Palmisano, "Vectorial ray-based diffraction integral," J. Opt. Soc. Am. A **32**(8), 1403-1424 (2015).

[40] M. Mout, M. Wick, F. Bociort, J. Petschulat, and P. Urbach, "Simulating multiple diffraction in imaging systems using a path integration method," Appl. Opt. **55**(14), 3847-3853 (2016).

[41] J. Kim, Y. Wang, and X. Zhang, "Calculation of vectorial diffraction in optical systems," J. Opt. Soc. Am. A **35**(4), 526-535 (2018).

[42] D. C. O'Shea, T. J. Suleski, A. D. Kathman, and D. W. Prather, *Diffraction optics: design, fabrication, and test* (SPIE, 2004).

- [43] Y. G. Soskind, *Field guide to diffractive optics* (SPIE, 2011).
- [44] V. A. Soifer, *Computer design of diffractive optics* (Elsevier, 2012).
- [45] C. Caloz and T. Itoh, *Electromagnetic metamaterials: transmission line theory and microwave applications* (Wiley, 2005).
- [46] N. Engheta and R. W. Ziolkowski (Eds.), *Metamaterials: physics and engineering explorations* (Wiley, 2006).
- [47] R. Marqués, F. Martín, and M. Sorolla, *Metamaterials with negative parameters: theory, design, and microwave applications* (Wiley, 2007).
- [48] S. Zouhdi, A. Sihvola, and A. P. Vinogradov (Eds.), *Metamaterials and plasmonics: fundamentals, modelling, applications* (Springer, 2008).
- [49] T. J. Cui, D. R. Smith, and R. Liu, *Metamaterials: theory, design, and applications* (Springer, 2009).
- [50] W. Cai and V. Shalaev, *Optical metamaterials: fundamentals and applications* (Springer, 2010).
- [51] M. A. Noginov and V. A. Podolskiy (Eds.), *Tutorials in metamaterials* (CRC, 2011).
- [52] D. H. Werner and D. H. Kwon (Eds.), *Transformation electromagnetics and metamaterials: fundamental principles and applications* (Springer, 2013).
- [53] D. R. Smith, W. J. Padilla, D. C. Vier, S. C. Nemat-Nasser, and S. Schultz, “Composite medium with simultaneously negative permeability and permittivity,” *Phys. Rev. Lett.* **84**(18), 4184 (2000).
- [54] D. R. Smith, D. C. Vier, N. Kroll, and S. Schultz, “Direct calculation of

permeability and permittivity for a left-handed metamaterial,” *Appl. Phys. Lett.* **77**(14), 2246-2248 (2000).

[55] R. A. Shelby, D. R. Smith, S. C. Nemat-Nasser, and S. Schultz, “Microwave transmission through a two-dimensional, isotropic, left-handed metamaterial,” *Appl. Phys. Lett.* **78**(4), 489-491 (2001).

[56] V. G. Veselago, “The electrodynamics of substances with simultaneously negative values of ϵ and μ ,” *Sov. Phys. Usp.* **10**(4), 509-514 (1968).

[57] J. B. Pendry, “Negative refraction makes a perfect lens,” *Phys. Rev. Lett.* **85**(18), 3966 (2000).

[58] N. Garcia and M. Nieto-Vesperinas, “Left-handed materials do not make a perfect lens,” *Phys. Rev. Lett.* **88**(20), 207403 (2002).

[59] D. O. Melville, R. J. Blaikie, and C. R. Wolf, “Submicron imaging with a planar silver lens,” *Appl. Phys. Lett.* **84**(22), 4403-4405 (2004).

[60] D. Schurig, J. J. Mock, B. J. Justice, S. A. Cummer, J. B. Pendry, A. F. Starr, and D. R. Smith, “Metamaterial electromagnetic cloak at microwave frequencies,” *Science* **314**(5801), 977-980 (2006).

[61] W. Cai, U. K. Chettiar, A. V. Kildishev, and V. M. Shalaev, “Optical cloaking with metamaterials,” *Nat. Photonics* **1**(4), 224-227 (2007).

[62] J. Li and J. B. Pendry, “Hiding under the carpet: a new strategy for cloaking,” *Phys. Rev. Lett.* **101**(20), 203901 (2008).

[63] J. Valentine, J. Li, T. Zentgraf, G. Bartal, and X. Zhang, “An optical cloak made of dielectrics,” *Nat. Mater.* **8**(7), 568-571 (2009).

- [64] T. Ergin, N. Strenger, P. Brenner, J. B. Pendry, and M. Wegener, “Three-dimensional invisibility cloak at optical wavelengths,” *Science* **328**(5976), 337-339 (2010).
- [65] A. Vakil and N. Engheta, “Transformation optics using graphene,” *Science* **332**(6035), 1291-1294 (2011).
- [66] S. Enoch, G. Tayeb, P. Sabouroux, N. Guérin, and P. Vincent, “A metamaterial for directive emission,” *Phys. Rev. Lett.* **89**(21), 213902 (2002).
- [67] R. W. Ziolkowski, “Propagation in and scattering from a matched metamaterial having a zero index of refraction,” *Phys. Rev. E* **70**(4), 046608 (2004).
- [68] H. Suchowski, K. O’Brien, Z. J. Wong, A. Salandrino, X. Yin, and X. Zhang, “Phase mismatch-free nonlinear propagation in optical zero-index materials,” *Science* **342**(6163), 1223-1226 (2013).
- [69] I. Liberal and N. Engheta, “Near-zero refractive index photonics,” *Nat. Photon.* **11**(3), 149-158 (2017).
- [70] H. T. Chen, A. J. Taylor, and N. Yu, “A review of metasurfaces: physics and applications,” *Rep. Prog. Phys.* **79**(7), 076401 (2016).
- [71] C. Holloway, E. F. Kuester, J. Gordon, J. O’hara, J. Booth, and D. Smith, “An overview of the theory and applications of metasurfaces: the two-dimensional equivalents of metamaterials,” *IEEE Antennas Propag. Mag.* **54**(2), 10-35 (2012).
- [72] N. Yu, P. Genevet, F. Aieta, M. Kats, R. Blanchard, G. Aoust, J. P. Tetienne, Z. Gaburro, and F. Capasso, “Flat optics: controlling wavefronts with optical antenna metasurfaces,” *IEEE J. Sel. Top. Quantum Electron.* **19**(3), 4700423 (2013).

- [73] A. V. Kildishev, A. Boltasseva, and V. M. Shalaev, “Planar photonics with metasurfaces,” *Science* **339**(6125), 1232009 (2013).
- [74] N. F. Yu, and F. Capasso, “Flat optics with designer metasurfaces,” *Nat. Mater.* **13**(2), 139-150 (2014).
- [75] S. Walia, C. M. Shah, P. Gutruf, H. Nili, D. R. Chowdhury, W. Withayachumnankul, M. Bhaskaran, and S. Sriam, “Flexible metasurfaces and metamaterials: a review of materials and fabrication processes at micro-and nano-scales,” *Appl. Phys. Rev.* **2**(1), 011303 (2015).
- [76] A. E. Minovich, A. E. Miroschnichenko, A. Y. Bykov, T. V. Murzina, D. N. Neshev, and Y. S. Kivshar, “Functional and nonlinear optical metasurfaces,” *Laser Photonics Rev.* **9**(2), 195-213 (2015).
- [77] P. Genevet and F. Capasso, “Holographic optical metasurface,” *Rep. Prog. Phys.* **78**(2), 024401 (2015).
- [78] M. K. Hedayati and M. Elbahri, “Review of metasurface plasmonic structural color,” *Plasmonics* **12**(5), 1463-1479 (2017).
- [79] G. Zheng, H. Mühlenbernd, M. Kenney, G. Li, T. Zentgraf, and S. Zhang, “Metasurface holograms reaching 80% efficiency,” *Nat. Nanotechnol.* **10**(4), 308–312 (2015).
- [80] J. P. B. Mueller, N. A. Rubin, R. C. Devlin, B. Groever, and F. Capasso, “Metasurface polarization optics: independent phase control of arbitrary orthogonal states of polarization,” *Phys. Rev. Lett.* **118**(11), 113901 (2017).
- [81] F. Yue, X. Zang, D. Wen, Z. Li, C. Zhang, H. Liu, B. D. Gerardot, W. Wang, G.

- Zheng, and X. Chen, “Geometric phase generated optical illusion,” *Sci. Rep.* **7**(1), 11440 (2017).
- [82] D. Wen, F. Yue, C. Zhang, X. Zang, H. Liu, W. Wang, and X. Chen, “Plasmonic metasurface for optical rotation,” *Appl. Phys. Lett.* **111**(2), 023102 (2017).
- [83] R. C. Devlin, M. Khorasaninejad, W. T. Chen, J. Oh, and F. Capasso, “Broadband high-efficiency dielectric metasurfaces for the visible spectrum,” *Proc. Natl. Acad. Sci. U.S.A.* **113**(38), 10473–10478 (2016).
- [84] P. C. Li, Y. Zhao, A. Alù, and E. T. Yu, “Experimental realization and modeling of a subwavelength frequency-selective plasmonic metasurface,” *Appl. Phys. Lett.* **99**(22), 221106 (2011).
- [85] F. Costa, A. Monochio, and G. Manara, “An overview of equivalent circuit modeling techniques of frequency selective surfaces and metasurfaces,” *Appl. Comput. Electromagn. Soc. J.* **29**(12), 960-976 (2014).
- [86] D. Costantini, A. Lefebvre, A. L. Coutrot, I. Moldovan-Doyen, J. P. Hugonin, S. Boutami, F. Marquier, H. Benisty, and J. J. Greffet, “Plasmonic metasurface for directional and frequency-selective thermal emission,” *Phys. Rev. Appl.* **4**(1), 014023 (2015).
- [87] H. L. Zhu, S. W. Cheung, K. L. Chung, and T. I. Yuk, “Linear-to-circular polarization conversion using metasurface,” *IEEE Trans. Antennas and Propag.* **61**(9), 4615-4623 (2013).
- [88] Y. Yang, W. Wang, P. Moitra, I. I. Kravchenko, D. P. Briggs, and J. Valentine,

“Dielectric meta-reflectarray for broadband linear polarization conversion and optical vortex generation,” *Nano Lett.* **14**(3), 1394-1399 (2014).

[89] J. Lončar and A. Grbic, “A reflective polarization converting metasurface at X-band frequencies,” *IEEE Trans. Antennas Propag.* (Early Access) (16, March, 2018).

[90] J. Lee, M. Tymchenko, C. Argyropoulos, P. Y. Chen, F. Lu, F. Demmerle, G. Boehm, M. C. Amann, A. Alù, and M. Belkin, “Giant nonlinear response from plasmonic metasurfaces coupled to intersubband transitions,” *Nature* **511**, 65-69 (2014).

[91] N. Nookala, J. Lee, M. Tymchenko, J. S. Gomez-Diaz, F. Demmerle, G. Boehm, K. Lai, G. Shvets, M. C. Amann, A. Alù, and M. Belkin, “Ultrathin gradient nonlinear metasurface with a giant nonlinear response,” *Optica* **3**(3), 283-288 (2016).

[92] G. Li, S. Chen, N. Pholchai, B. Reineke, P. W. H. Wong, E. Y. B. Pun, K. W. Cheah, T. Zentgraf, and S. Zhang, “Continuous control of the nonlinearity phase for harmonic generations,” *Nat. Mater.* **14**(6), 607-612 (2015).

[93] U. Kreibig and M. Vollmer, *Optical properties of metal clusters* (Springer, 1995).

[94] A. V. Zayats and S. A. Maier, *Active plasmonics and tuneable plasmonic metamaterials* (Wiley, 2013).

[95] P. N. Prasad, *Nanophotonics* (Wiley, 2004).

[96] S. A. Maier, *Plasmonics: fundamentals and applications* (Springer, 2007).

- [97] J. A. Polo, T. G. Mackay, and A. Lakhtakia, *Electromagnetic surface waves: a modern perspective* (Elsevier, 2013).
- [98] “S. A. Maier and H. A. Atwater, “Plasmonics: localization and guiding of electromagnetic energy in metal/dielectric structures,” *J. Appl. Phys.* **98**(1), 011101 (2005).
- [99] Y. Fang and M. Sun, “Nanoplasmonic waveguides: towards applications in integrated nanophotonic circuits,” *Light Sci. Appl.* **4**(6), e294 (2015).
- [100] S. I. Bozhevolnyi, V. S. Volkov, E. Devaux, J. -Y. Laluet, and T. W. Ebbesen, “Channel plasmon subwavelength waveguide components including interferometers and ring resonators,” *Nature* **440**(7083), 508-511 (2006).
- [101] I. -M. Lee, J. Jung, J. Park, H. Kim, and B. Lee, “Dispersion characteristics of channel plasmon polaritons waveguides with step-trench-type grooves,” *Opt. Express* **15**(25), 16596-16603 (2007).
- [102] D. Choi, I. -M. Lee, J. Jung, J. Park, J. -H. Han, and B. Lee, “Metallic-grating-based interconnector between surface plasmon polariton waveguides,” *J. Lightw. Technol.* **27**(24), 5675-5680 (2009).
- [103] S. -Y. Lee, J. Park, M. Kang, and B. Lee, “Highly efficient plasmonic interconnector based on the asymmetric junction between metal-dielectric-metal and dielectric slab waveguides,” *Opt. Express* **19**(10), 9562-9574 (2011).
- [104] S. -Y. Lee, J. Kim, I. -M. Lee, and B. Lee, “Efficient transition between photonic and plasmonic guided modes at abrupt junction of MIM plasmonic waveguide,” *Opt. Express* **21**(18), 20762-20770 (2013).

- [105] K. F. MacDonald, Z. L. Sámson, M. I. Stockman, and N. I. Zheludev, “Ultrafast active plasmonics,” *Nat. Photon.* **3**(1), 55-58 (2009).
- [106] W. Cai, J. S. White, and M. L. Brongersma, “Compact, high-speed and power-efficient electrooptic plasmonic modulators,” *Nano Lett.* **9**(12), 4403-4411 (2009).
- [107] J. A. Conway, S. Sahni, and T. Szkopek, “Plasmonic interconnects versus conventional interconnects: a comparison of latency, cross-talk and energy costs,” *Opt. Express* **15**(8), 4474-4484 (2007).
- [108] A. V. Krasavin and A. V. Zayats, “Silicon-based plasmonic waveguides,” *18*(11), 11791-11799 (2010).
- [109] N. Kinsey, M. Ferrera, G. V. Naik, V. E. Babicheva, V. M. Shalaev, and A. Boltasseva, “Experimental demonstration of titanium nitride plasmonic interconnects,” *Opt. Express* **22**(10), 12238-12247 (2014).
- [110] C. Zhao and J. Zhang, “Plasmonic demultiplexer and guiding,” *ACS Nano* **4**(11), 6433-6438 (2010).
- [111] B. Lee, S. Kim, H. Kim, and Y. Lim, “The use of plasmonics in light beaming and focusing,” *Prog. Quantum Electron.* **34**(2), 47-87 (2010).
- [112] Y. Gao, Z. Xin, B. Zeng, Q. Gan, X. Cheng, and F. J. Bartoli, “Plasmonic interferometric sensor arrays for high performance label-free biomolecular detection,” *Lap Chip* **13**(24), 4755-4764 (2013).
- [113] W. Srituravanich, L. Pan, Y. Wang, C. Sun, D. B. Bogy, and X. Zhang, “Flying plasmonic lens in the near field for high-speed nanolithography,” *Nat.*

Nanotech. **3**(12), 733 (2008).

[114] C. Min, Z. Shen, J. Shen, Y. Zhang, H. Fang, G. Yuan, L. Du, S. Zhu, T. Lei, and X. Yuan, “Focused plasmonic trapping of metallic particles,” *Nat. Commun.* **4**, 2891 (2013).

[115] I. Epstein, Y. Tsur, and A. Arie, “Surface-plasmon wavefront and spectral shaping by near-field holography,” *Laser Photonics Rev.* **10**(3), 360-381 (2016).

[116] H. Kim, J. Park, S.-W. Cho, S.-Y. Lee, M. Kang, and B. Lee, “Synthesis and dynamic switching of surface plasmon vortices with plasmonic vortex lens,” *Nano Lett.* **10**(2), 529-536 (2010).

[117] A. E. Minovich, A. E. Klein, D. N. Neshev, T. Pertsch, Y. S. Kivshar, and D. N. Christodoulides, “Airy plasmons: non-diffracting optical surface waves,” *Laser Photonics Rev.* **8**(2), 221-232 (2014).

[118] S.-Y. Lee, S.-J. Kim, H. Kwon, and B. Lee, “Spin-direction control of high-order plasmonic vortex with double-ring distributed nanoslits,” *IEEE Photon. Technol. Lett.* **27**(7), 705-708 (2015).

[119] S. -Y. Lee, K. Kim, S. -J. Kim, H. Park, K. -Y. Kim, and B. Lee, “Plasmonic meta-slit: shaping and controlling near-field focus,” *Optica* **2**(1), 6-13 (2015).

[120] E. -Y. Song, S. -Y. Lee, J. Hong, K. Lee, Y. Lee, G. -Y. Lee, H. Kim, and B. Lee, “A double-lined metasurface for plasmonic complex-field generation,” *Laser Photonics Rev.* **10**(2), 299-306 (2016).

[121] J. Chen, L. Li, T. Li, and S. N. Zhu, “Indefinite plasmonic beam engineering by in-plane holography,” *Sci. Rep.* **6**(1), 28926 (2016).

- [122] Y. Tsur, I. Epstein, R. Remez, and A. Arie, “Wavefront shaping of plasmonic beams by selective coupling,” *ACS Photonics* **4**(6), 1339-1343 (2017).
- [123] L. Zhu, Z. Xiong, W. Yu, X. Tian, Y. Kong, C. Lu, and S. Wang, “Polarization-controlled tunable multi-focal plasmonic lens,” *Plasmonics* **12**(1), 33-38 (2017).
- [124] C. L. Holloway, A. Dienstfrey, E. F. Kuester, J. F. O’Hara, A. K. Azad, and A. J. Taylor, “A discussion on the interpretation and characterization of metafilms/metasurfaces: the two-dimensional equivalent of metamaterials,” *Metamaterials* **3**(2), 100-112 (2009).
- [125] C. Pfeiffer and A. Grbic, “Metamaterial Huygens’ surfaces: tailoring wavefronts with reflectionless sheets,” *Phys. Rev. Lett.* **110**(19), 197401 (2013).
- [126] C. Pfeiffer and A. Grbic, “Bianisotropic metasurfaces for optimal polarization control: analysis and synthesis,” *Phys. Rev. Appl.* **2**(4), 044011 (2014).
- [127] S. B. Glybovski, S. A. Tretyakov, P. A. Belov, Y. S. Kivshar, and C. R. Simovski, “Metasurfaces: from microwaves to visible,” *Phys. Rep.* **634**, 1-72 (2016).
- [128] L. Zhang, S. Mei, K. Huang, and C. W. Qiu, “Advances in full control of electromagnetic waves with metasurfaces,” *Adv. Opt. Mater.* **4**(6), 818-833 (2016).
- [129] A. Epstein and G. V. Eleftheriades, “Huygens’ metasurfaces via the equivalence principle: design and applications,” *J. Opt. Soc. Am. B* **33**(2), A31-A50 (2016).
- [130] N. M. Estakhri and A. Alù, “Wave-front transformation with gradient

- metasurfaces,” *Phys. Rev. X* **6**(4), 041008 (2016).
- [131] F. Ding, Z. Wang, S. He, V. M. Shalaev, and A. V. Kildishev, “Broadband high-efficiency half-wave plate: a supercell-based plasmonic metasurface approach,” *ACS Nano* **9**(4), 4111-4119 (2015).
- [132] A. Pors, M. G. Nielsen, and S. I. Bozhevolnyi, “Plasmonic metagratings for simultaneous determination of Stokes parameters,” *Optica* **2**(8), 716-723 (2015).
- [133] L. H. Gao, Q. Cheng, J. Yang, S. J. Ma, J. Zhao, S. Liu, H. B. Chen, Q. He, W. X. Jiang, H. F. Ma, Q. Y. Wen, L. J. Liang, B. B. Jin, W. W. Liu, L. Zhou, J. Q. Yao, P. H. Wu, and T. J. Cui, “Broadband diffusion of terahertz waves by multi-bit coding metasurfaces,” *Light Sci. Appl.* **4**(9), e324 (2015).
- [134] J. Petschulat, J. Yang, C. Menzel, C. Rockstuhl, A. Chipouline, P. Lalanne, A. Tünnermann, F. Lederer, and T. Pertsch, “Understanding the electric and magnetic response of isolated metaatoms by means of a multipolar field decomposition,” *Opt. Express* **18**(14), 14454-14466 (2010).
- [135] C. Rockstuhl, C. Menzel, S. Mühlig, J. Petschulat, C. Helgert, C. Etrich, A. Chipouline, T. Pertsch, and F. Lederer, “Scattering properties of meta-atoms,” *Phys. Rev. B* **83**(24), 245119 (2011).
- [136] S. Mühlig, C. Menzel, C. Rockstuhl, and F. Lederer, “Multipole analysis of meta-atoms,” *Metamaterials* **5**(2-3), 64-73 (2011).
- [137] M. Decker, I. Staude, M. Falkner, J. Dominguez, D. N. Neshev, I. Brener, T. Pertsch, and Y. S. Kivshar, “High-efficiency dielectric Huygens’ surfaces,” *Adv. Opt. Mater.* **3**(6), 813-820 (2015).

- [138] M. Gupta, V. Savinov, N. Xu, L. Cong, G. Dayal, S. Wang, W. Zhang, N. I. Zheludev, and R. Singh, “Sharp toroidal resonances in planar terahertz metasurfaces,” *Adv. Mater.* **28**(37), 8206-8211 (2016).
- [139] T. Chung, S. -Y. Lee, E. Y. Song, H. Chun, and B. Lee, “Plasmonic nanostructures for nano-scale bio-sensing,” *Sensors* **11**(11), 10907-10929 (2011).
- [140] T. Søndergaard, J. Jung, S. I. Bozhevolnyi and G. D. Valle, “Theoretical analysis of gold nano-strip gap plasmon resonators,” *New J. Phys.* **10**(10), 105008 (2008).
- [141] A. Yariv, “Universal relations for coupling of optical power between microresonators and dielectric waveguides,” *Electron. Lett.* **36**(4), 321-322 (2000).
- [142] M. J. Weber, *Handbook of Optical Materials* (CRC, 2003).
- [143] J. A. Nelder, and M. Roger, “A simplex method for function minimization,” *Computer J.* **7**(4), 308-313 (1965).
- [144] M. V. Berry and N. L. Balazs, “Nonspreading wave packets,” *Am. J. Phys.* **47**(3), 264-267 (1979).
- [145] A. Salandrino and D. N. Christodoulides, “Airy plasmon: a nondiffracting surface wave,” *Opt. Lett.* **35**(12), 2082-2084 (2010).
- [146] A. V. Novitsky and D. V. Novitsky, “Negative propagation of vector Bessel beams,” *J. Opt. Soc. Am. A* **24**(9), 2844-2849 (2007).
- [147] W. T. Chen, M. Khorasaninejad, A. Y. Zhu, J. Oh, R. C. Devlin, A. Zaidi, F. Capasso, “Generation of wavelength-independent subwavelength Bessel beams using metasurfaces,” *Light Sci. Appl.* **6**(5), e16259 (2017).

- [148] R. Dorn, S. Quabis, and G. Leuchs, "The focus of light-linear polarization breaks the rotational symmetry of the focal spot," *J. Mod. Opt.* **50**(12), 1917-1926 (2003).
- [149] J. W. Chon, X. Gan, and M. Gu, "Splitting of the focal spot of a high numerical-aperture objective in free space," *Appl. Phys. Lett.* **81**(9), 1576-1578 (2002).
- [150] A. April, "Bessel-Gauss beams as rigorous solutions of the Helmholtz equation," *J. Opt. Soc. Am. A* **28**(10), 2100-2107 (2011).
- [151] Q. Zhan, "Cylindrical vector beams: from mathematical concepts to applications," *Adv. Opt. Photonics* **1**(1), 1-57 (2009).
- [152] Z. Bouchal and M. Olivík "Non-diffractive vector Bessel beams," *J. Mod. Opt.* **42**(8), 1555-1566 (1995).
- [153] F. Yue, D. Wen, J. Xin, B. D. Gerardot, J. Li, and X. Chen, "Vector vortex beam generation with a single plasmonic metasurface," *ACS Photonics* **3**(9), 1558-1563 (2016).
- [154] D. G. Hall, "Vector-beam solutions of Maxwell's wave equation," *Opt. Lett.* **21**(1), 9-11 (1996).
- [155] K. Huang, P. Shi, G. W. Cao, K. Li, X. B. Zhang, and Y. P. Li, "Vector-vortex Bessel-Gauss beams and their tightly focusing properties," *Opt. Lett.* **36**(6), 888-890 (2011).
- [156] G. -Y. Lee, G. Yoon, S. -Y. Lee, H. Yun, J. Cho, K. Lee, H. Kim, J. Rho, and B. Lee, "Complete amplitude and phase control of light using broadband

holographic metasurfaces,” *Nanoscale* **10**(9), 4237-4235 (2018).

Appendix

Portions of the work discussed in this dissertation are also presented in the following publications:

[Chapter 2, 4] H. Park, S.-Y. Lee, J. Kim, B. Lee, and H. Kim, “Near-infrared coherent absorption in plasmonic metal-insulator-metal waveguide,” *Opt. Express*, **23**(19), 24464-24474 (2015).

[Chapter 2, 5] H. Park, J. Kim, Y. Jeon, B. Lee, and H. Kim, “Regularized Huygens’ plasmonic wave field synthesis using a metal-clad plasmonic waveguide array,” *Opt. Lett.* **42**(18), 3610-3613 (2017).

[Chapter 3] H. Park, H. Yun, C. Choi, J. Hong, H. Kim, and B. Lee, “Huygens’ optical vector wave field synthesis via in-plane electric dipole metasurface,” *Opt. Express* **26**(8), 10649-10660 (2018).

초 록

1690년 빛의 반사와 굴절을 설명하기 위해 제안했던 호이겐스 원리는 광학 회절 이론의 중심이 되어 왔다. 특히 이차 파의 개념은 지금까지도 회절, 분산 현상을 설명하는데 유용하다. 최근에 이르러 메타물질 분야가 지난 20년간의 응용 물리학에서 가장 활성화되었다. 메타원자는 3차원의 메타물질, 2차원의 메타표면, 1차원의 메타슬릿 구성 단위다. 메타원자가 파장 이하 크기의 설계된 인공 구조물이므로 이는 호이겐스 광원으로 취급할 수 있다. 메타원자의 형상과 배열을 통해 연구자들은 색다른 광학 성질을 가지는 메타물질들을 개발해냈다. 그러나 메타 원자들의 방사 패턴에 관한 깊은 고찰은 거의 이루어지지 않았다. 본 논문에서는, 광학장 및 플라즈몬 장의 저잡음 형성을 위해 새로운 종류의 메타표면과 메타슬릿을 제안하고 시험하여 메타 원자들의 방사 패턴 설계의 중요성을 다룬다.

첫째로, 호이겐스 원리에 기반한 광학 회절 이론들을 역사적으로 개괄하여, 호이겐스 광원을 정의하고 메타원자들이 지정된 방사 패턴을 가지는 호이겐스 광원으로 어떻게 사용되는지 살핀다. 정규화된 방사 패턴을 가지는 호이겐스 광원을 규칙적으로 배열해 왜곡 없는 평면파를 생성하는 방법을 보인 후, 이상적인 호이겐스 광원 배열이 극도로 잡음 세기가 낮은 임의의 장 형성을 위해 사용되는 수학적 공식화 방식을 제시한다.

다음으로 정규화된 메타원자의 복소 진폭 변조 가능성을 조사한다. 임의의 광파 및 플라즈몬 파가 복소 진폭 분포로 설명되기 때문에 이 연구는 정규화된 호이겐스 광원에 기반한 메타표면과 메타슬릿 개발에 결정적으로 중요하다.

이어지는 두 장(章)에서는 2장에서 제안된 방법을 개량하여 광파 및 플라즈몬 파 생성 방식을 시연하는데 할애한다. 복소 진폭과 편광을 정할 수 있는 정규화된 방사 패턴을 가지는 메타원자를 구현할 수 있다고 가정할 때, 이를 주기적으로 배열하여 구축한 메타표면과 메타슬릿을 통해 임의의 광파 및 플라즈몬 파를 생성할 수 있음을 보인다.

4장에서는 정규화된 메타슬릿의 구체적인 예로 금속 클레드 도파로 배열체가 제안된다. 플라즈몬 집속과 플라즈몬 에어리 빔이 제시된 구조를 통해 생성된다. 생성된 파면을 신호-대-잡음 비 관점에서 해석하기 위해 필드 시뮬레이션을 포함한 수치해석 결과들이 제시된다. 실험적 구현 방식도 제안된다.

이어지는 장에서는, 광학장 합성을 위해 2장과 4장에서 제시되었던 장 합성 방식을 일반화하는 방법을 제안한다. 복소 변조된 평면 상의 전기 쌍극자 모멘트를 부여할 수 있는 메타원자가 존재한다고 가정할 때, 이 가상의 메타원자로 이루어진 메타표면이 잡음 세기가 극도로 낮은 일반화된 장 합성 방식을 구현할 수 있음을 보인다. 또한 제안된 메타표면의 근사 방식으로 준(準)정규화 방법을 제시한다. 준정규화된 메타표면을 포함한 다양한 메타표면을 이용해 에어리 원반, 베셀-가우스 빔, 홀로그램을 생성하여 신호-대-잡음 비 관점에서 비교분석한다. 제안된 메타표면들의 홀로그램 생성을 실험 결과로 확인하였다.

본 논문의 결과는 메타원자의 방사 패턴을 고려하여 빛과 표면 플라즈몬의 생성 및 조사를 완전히 제어할 수 있는 진전된 메타장치를 개발하는 데 기여할 것으로 기대된다. 또한 제안된 정규화 방법을 적용하면 공간 광 변조기의 광각 동작에서 매우 낮은 잡음 세기를 실현 가능하며, 이를 위해 초소형 능동 변조 메커니즘에 관한 앞으로의 연구가 필요하다.

주요어: 호이젠스 원리, 방사 패턴, 복소 변조, 광학장, 플라즈몬장,
메타표면, 메타슬릿
학 번: 2012-20775